

# Hochschule für Angewandte Wissenschaften Hamburg Hamburg University of Applied Sciences

### **Masterthesis**

Lukas Müller

Data driven optimization of slow longitudinal feedback systems for free electron lasers

# Lukas Müller

# "Data driven optimization of slow longitudinal feedback systems for free electron lasers"

Masterarbeit eingereicht im Rahmen der Masterprüfung

im Studiengang Berechnung und Simulation im Maschinenbau am Department Maschinenbau und Produktion der Fakultät Technik und Informatik der Hochschule für Angewandte Wissenschaften Hamburg

in Zusammenarbeit mit:

Deutsches Elektronen-Synchrotron DESY Abteilung: MSK (Maschine Strahlkontrollen) Notkestraße 85 22607 Hamburg

Erstprüferin: Prof. Dr. Sarah Hallerberg Zweitprüferin: Prof. Dr. Annika Eichler

Abgabedatum: 26.09.2024

#### Abstract

To enable a reliable SASE (self-amplified spontaneous emission) process at free-electron lasers, stable electron beam properties are needed. The slow longitudinal feedback system compensates long term drifts of the accelerating modules using toroids, beam arrival monitors and beam compression monitors. To optimize the current system, various approaches are investigated. Beginning with the evaluation of the current mathematical model and moving on towards the inversion of linear and nonlinear response matrices, a description of the system needs to be found. As measurable outcomes, the RSME and the amount of mismatching derivatives signs are considered. Furthermore, the system is checked for dynamics. Finally, a modified version of the SINDy-algorithm is introduced and all approaches are compared to each other.

To access the necessary data for the optimization, a parameter scan at the particle accelerator FLASH was performed by scanning all actuators randomly and simultaneously

#### Abstrakt

Um einen zuverlässigen SASE (self-amplified spontaneous emission) Prozess an Freie-Elektronen-Lasern zu ermöglichen, werden stabile Eigenschaften des Elektronenstrahls benötigt. Das langsame, longitudinale Feedbacksystem kompensiert langsames Driften der Beschleunigermodule indem Toroiden, beam arrival monitors und beam compression monitors für die Regelung verwendet werden. Um das vorhandende System zu optimieren, werden unterschiedliche Ansätze untersucht. Beginnend mit der Bewertung des aktuellen Ansatzes und dem zugrundeliegenden mathematischen Modell, über die Invertierung linearer und nichtlinearer Antwortmatrizen wird eine Beschreibung des Systems gesucht. Als messbare Größen werden hierbei der RSME und die falsch vorhergesagten Vorzeichen der Ableitung verwendet. Weiterhin wird das System auf dynamisches Verhalten untersucht. Schließlich wird eine modifizierte Version des SINDy-Algorithmus eingeführt und die verschiedenen Ansätze miteinander verglichen.

Um die notwendigen Daten für die Optimierung zu erheben, wurde ein Parameterscan am Teilchenbeschleuniger FLASH durchgeführt. Hierbei wurden zeitgleich alle Aktuatoren zufällig verändert.

# Contents

Li	List of acronyms 8			
Li	st of	symbo	ols	10
1	Intr	oducti	on	12
	1.1	X-ray	free electron lasers	12
		1.1.1	FLASH	13
		1.1.2	European XFEL	14
	1.2	Task		14
2	Bas	ics and	l current status	16
	2.1	Diagno	ostics	16
		2.1.1	Laser based synchronization systems	16
		2.1.2	Toroids	17
		2.1.3	Beam arrival monitors	18
		2.1.4	Beam compression monitors	19
	2.2	Layout	t of the slow longitudinal Feedback System at FLASH and European	
		XFEL		20
		2.2.1	Gun	20
		2.2.2	First accelerating modules	22
		2.2.3	First bunch compressor	23
		2.2.4	Accelerating modules 2,3 and second bunch compressor	25
		2.2.5	Accelerating modules 4,5 and 6,7	25
		2.2.6	Differences between FLASH and EuXFEL	25
	2.3	Contro	ol system data	25
		2.3.1	Monitors	25
		2.3.2	Actuators	26
	2.4	Slow lo	ongitudinal feedback control system	27
3	Ana	alysis o	f the existing system	32
	3.1	Simpli	fied model	32
	3.2	Extend	ded model	32
4	Ma	chine le	earning approaches	38
	4.1	Regres	$\operatorname{sion}$	38
	4.2	Sparse	identification of nonlinear dynamics (SINDy)	39
	4.3	Conve	x optimization	42

5	Ger	neratin	g data sets at FLASH	44
	5.1	Data i	from DAQ and user operation	44
	5.2	Param	neter scans	46
6	Ana	alysis c	of the data sets	50
	6.1	Recald	culation of the linear response matrix	50
	6.2	Nonlin	near response matrix	60
	6.3	Sparse	e Identification of Nonlinear Dynamics	68
		6.3.1	SINDy	69
		6.3.2	SINDy with control	69
	6.4	SINDy	y modified	71
		6.4.1	Indirect calculation of the actuator values using a modified SINDy algorithm	71
		6.4.2	Direct calculation of the actuator values using the modified SINDy	
			algorithm	75
		6.4.3	Optimization of the modified SINDy algorithm	78
	6.5	Addin	g further base functions to SINDy modified	82
	6.6	Influer	nce of the bunch number for control	84
7	Cor	nclusio	n and Outlook	85
$\mathbf{R}$	efere	nces		89
$\mathbf{A}$	ppen	dix		91
$\mathbf{A}$	ppen	dix A	Additional figures for the analysis of the existing system	
$\mathbf{A}$	ppen	dix B	$\frac{\delta m}{\delta a}$ -plot with raw data	
$\mathbf{A}$	ppen	dix C	Nonlinear fit for all actuators	
$\mathbf{A}$	ppen	dix D	Optimization of the LASSO regressed model	

# List of Figures

1	Accelerators at DESY[1]	12
2	Schematic of a basic free electron laser $[2]$	13
3	FLASH Layout[3]	14
4	XFEL Layout[4]	14
5	Schematic diagram of FLASH longitudinal feedback[5]	16
6	Schematic layout of the laser-based synchronization system[6]	17
7	Hardware setup with high dynamic range feature (simplified) system[7]	18
8	Basic layout of the BAM cabling scheme[6]	18
9	CAD model of the screen station and CDR screen[8]	19
10	Diffraction radiation measurement with BCM[6]	20
11	$\operatorname{Gun}[9]$	21
12	Laser schematic	21
13	Gun amplitude and phase over time	22
14	Energy $E$ over phase $\phi$ , black line is the desired working point	22
15	Energy change $E$ over time $t$ in working point	23
16	Accelerating modules[9]	23
17	Current distribution over a time[10]	24
18	Magnetic chicane [11]	24
19	Macrobunch BCM downstream of bunch compressor 1	26
20	Sumvoltage and chirp values of ACC23	27
21	Response Matrix FLASH expert panel	28
22	actuators FLASH expert panel	29
23	monitors FLASH expert panel	30
24	slow RF Feedback Control Panel	31
25	results for all monitors using the simplified response matrix $C$ with the	
	extended model	35
26	results for all actuators using the simplified response matrix $C$ with the	
	extended model	36
27	Visualization of the SINDy-algorithm for the Lorenz system $[12]$	42
28	Gun amplitude and phase beam region 1	45
29	Example of BAM spectra and the first entries of each spectrum	46
30	Actuator values of the parameter scan	48
31	Monitor values of the parameter scan	49
32	Comparison of original actuator changes and recalculated changes with	
	FLASH 2024 response matrix and measured linear response matrix (test	
	dataset)	53

33	reduced response matrix	55
34	Comparison of original actuator changes with recalculated changes using a	
	single loop response matrix	56
35	Comparison of original actuator changes with recalculated changes using a full, reduced and single loop response matrix after normalization of the	
36	data within the interval [1,2] and rescaling	59
07	rescaling	60
37	nonlinear dependencies between changes of actuators and monitors	
38 39	Fitted data for gun phase with polynomials of order 2	63
	matrix approach	64
40	Comparison gun phase, measured values and estimated values from full, reduced and single loop approach	66
41	Fitted data for gun phase with polynomials of order 2 compared to the	
	original values	67
42	Fitted data for ACC139 sumvoltage and chirp with polynomials of order 4 and 2 compared to the original values	68
43	Fitted data for ACC23 sumvoltage and chirp with polynomials of order 2 compared to the original values	68
44	Fitted data for ACC45 sum voltage and chirp with polynomials of order $2$	
45	compared to the original values	68
46	polynomial order of 2	69
40	and maximum polynomial order of 2	70
47	Sparsity matrix visualization with $\lambda = 0.5$ and maximum polynomial order of $2 \dots $	72
48	Visualization of the recalculated monitor changes with $\lambda=0.5$ and maximum polynomial order of 2 using a modified version of the SINDy algorithm	73
49	Recalculated actuator changes from the modified SINDy approach (test	
£0	data set)	74
50	Sparsity matrix visualization with $\lambda = 0.5$ and maximum polynomial order of 2 of the direct approach	76
51		76
ÐΙ	Sparsity matrix visualization with $\lambda = 0.5$ and maximum polynomial order of 2 using the direct approach	77
	OI 4 using the unet approach	11

52	Optimization of the modified SINDy approach: scan $\lambda$ in the range of [0, 1]
	using sequential least squares and polynomial order 1 to find lowest RSME 79
53	Optimization of the modified SINDy approach: scan $\lambda$ in the range of $[0,1]$
	using sequential least squares and polynomial order 2 to find lowest RSME 79
54	Sparsity matrices from the optimized approaches
55	Visualization of the sparsity matrix using convex optimization and addi-
	tional terms
56	results for all monitors using the simplified response matrix $C$
57	results for all actuators using the simplified response matrix $C$
58	results for all monitors using the response matrix $R$ with the extended modelA-3
59	results for all actuators using the response matrix $R$ with the extended modelA-4
60	nonlinear dependencies between changes of actuators and monitors B-1 $$
61	Fitted data for ACC139 sum voltage with polynomials of order 4 $$ C-1
62	Fitted data for ACC139 chirp with polynomials of order 2
63	Fitted data for ACC23 sum voltage with polynomials of order $2 \dots \dots $ . C-2
64	Fitted data for ACC23 chirp with polynomials of order 2
65	Fitted data for ACC45 sum voltage with polynomials of order $2 \dots \dots$ . C-3
66	Optimization of the modified SINDy approach: scan $\lambda$ in the range of $[0,1]$
	using convex optimization and polynomial order 1 to find lowest RSME $$ . $$ D-1 $$
67	Optimization of the modified SINDy approach: scan $\lambda$ in the range of $[0,1]$
	using convex optimization and polynomial order 2 to find lowest RSME $$ . $$ D-1 $$

# **List of Tables**

1	Allowed changes during the parameter scan	48
2	Constraints for the combination of actuators and monitors for a reduced	
	matrix approach	54
3	Constraints for the combination of actuators and monitors for a single loop	
	approach	55
4	RSME of the calculated actuator values for the test data set	57
5	False signs of the calculated actuator changes for the test data set	57
6	Condition numbers linear	58
7	Condition numbers linear after normalization	58
8	RSME of the calculated actuator values for the normalized test data set $$ .	60
9	False signs of the calculated actuator changes for the normalized test data	
	set	60
10	Parameters contained in the data set, polynomials used and RSME of the	
	fit compared to a linear fit	63
11	Condition numbers non linear after normalization	66
12	RSME of the calculated actuator values	67
13	False signs of the calculated actuator values	67
14	RSME and false prediced signs of the actuator changes of the calculated	
	actuator values	68
15	RSME of the calculated monitor values and false signs of the monitor	
	changes during test with 117 setpoints using the SINDy algorithm and	
	the normalized data set	69
16	RSME of the calculated monitor values during test with $117$ setpoints (nor-	
	$malized\ data)\ \dots$	70
17	RSME and false predicted signs of the derivatives of the recalculated actu-	
	ator values from the test data set using the indirect approach	74
18	RSME and false predicted sign of the derivatives of the calculated monitor	
	values during training using the indirect approach	74
19	RSME and false predicted signs of the derivatives of the calculated monitor	
	values during testing using the indirect approach	74
20	RSME and false predicted signs of the derivatives of the recalculated actu-	
	ator values from the training data set using the direct approach $\dots$	77
21	RSME and false predicted signs of the derivatives of the recalculated actu-	
	ator values from the test data set using the direct approach	77
22	Possible polynomial orders referring to the given training data set with 233	
	setpoints	78

23	RSME and false predicted signs of the derivatives of the recalculated ac-	
	tuator values from the test data set using the optimized direct approach	
	compared to the not optimized, direct SINDy approach	80
24	RSME and sign evaluation of the direct SINDy approach using LASSO-	
	regression compared to the non-optimized, direct SINDy approach	81
25	RSME and false predicted signs of the derivatives of the recalculated ac-	
	tuator values from the test data set compared to the not optimized, direct	
	SINDy approach	82
26	RSME and falsely predicted derivatives signs of the recalculated actuator	
	values from the test data set compared to the not optimized, direct SINDy	
	approach using the mean value of the macrobunch	84
27	RSME and falsely predicted derivatives signs of the recalculated actuator	
	values from the test data set compared to the non-optimized, direct SINDy	
	approach using the median value of the macrobunch	84
28	Comparison of all approaches applied to the test data set (RSME)	86
29	Comparison of all approaches applied to the test data set (derivative sign)	87

# List of acronyms

acronym	description
ACC139 C	accelerating modules 1 and 3.9 GHz chirp
ACC139 SV	accelerating modules 1 and 3.9 GHz sumvoltage
ACC23 C	accelerating modules 2 and 3 chirp
ACC23 SV	accelerating modules 2 and 3 sum voltage $$
ACC45 C	accelerating modules 4 and 5 chirp
ACC45 SV	accelerating modules 4 and 5 sum voltage $$
ACC67 C	accelerating modules 6 and 7 chirp
ACC67 SV	accelerating modules 6 and 7 sum voltage $$
BAM	beam arrival monitors
BCM	beam compression monitors
CDR	coherent diffraction radiation
DAQ	data acquisition server
DESY	Deutsches Elektronen-Synchrotron
DMD	dynamic mode decomposition
EOM	electro-optical modulator
EuXFEL	European XFEL
LINAC	linear accelerator
MPS	machine protection system
MSE	mean squared error
RF	radio frequency
RSME	root mean squared error
SASE	self-amplified spontaneous emisson
SINDy	Sparse identification of nonlinear dynamics
SVD	singular value depositon
XFEL	X-ray free-electron laser

# List of symbols

symbol	description
coeff1	coefficients for gun fit
$\delta a$	actuator changes
$\delta ampl$	amplitude changes
$\delta BAM$	BAM changes
$\delta BCM$	BCM changes
$\delta E$	engergy change
$\delta m$	monitor changes
$\delta phase$	phase changes
$\dot{x}$	time dependent derivative of x
$\hat{a}$	best fit coefficient
$\hat{b}$	best fit coefficient
$\hat{y}$	original feature values
$\lambda$	sparsification hyperparameter, LASSO regularization parameter
$\mu$	mean values
$\phi$	phase
Θ	libary terms
$\tilde{\delta a}$	vector of actuator changes
$\tilde{\delta m}$	vechtor of monitor changes
a	coefficient, actuator value
$a_0$	initial actuator value
avg	vector with number of bunches for averaging
B	binary matrix
b	coefficient
C	simplified, inverse response matrix
c	coefficients
$c_{MSE}$	mean squared error
E	engergy
$e_{RSME}$	root mean square error
F	fudge factor matrix
k	counter
limits	actuator limits
m	size of monitors, coefficient to be calculated
M	best fit coefficient matrix
$m_0$	initial monitor value
n	vector length

symbol	$\operatorname{description}$
p	polynomial order
R	response matrix
$\mathbb{R}$	real space
$\mathcal R$	regularization term
S	standard deviation
t	time
x	variable
X	variable matrix
ξ	sparsification vector
Ξ	sparsification matrix
y	feature values
Y	feature vector

### 1. Introduction

The Deutsches Elektronen-Sychrotron (DESY) is one of the leading institutes for accelerator physics worldwide. It has two different sites in Germany, on the one hand, there is a campus in Zeuthen, where astrophysical experiments are developed and performed. In addition to this, the development of new injectors for particle accelerators takes place there, too. On the other hand, there is a site in Hamburg where different particle accelerators are developed and prosecuted. In total, DESY has about 2700 employees and about 3000 scientists visiting the campus every year.

On campus in Hamburg, there are accelerators of different types for various purposes. There are ring accelerators like PETRAIII, with its pre-accelerators PIA and DES,Y as well as linear accelerators e.g., FLASH and the EuXFEL. An overview of the main facilities is provided in fig.1.



Figure 1: Accelerators at DESY[1]

### 1.1. X-ray free electron lasers

In the last years, X-ray free-electron lasers (XFEL) became a significant factor in experiments with matter and fluids. Compared to synchrotron radiation facilities like PETRAIII, they have the advantage that a large number of photons can be used for the exploration of different probes on a femtosecond scale, whereas synchrotron radiation sources deliver the photons on a picosecond scale. This leads to new opportunities for experiments. With XFELs it is possible to explore dynamic processes of atoms or molecules. [13]

Fig. 2 shows the basic principle of an XFEL. First, electron bunches exit the electron gun in a certain bunch pattern and get accelerated e.g. with radio frequency in superconducting cavities. After the acceleration, the bunch is often compressed with the help of a magnetic chicane (bunch compressor), acceleration and compression can repeat several times. Finally, the beam enters a wiggler or undulator, which usually consist of many permanent magnets of different orientation in longitudinal and transversal direction. When the electrons change their direction according to the magnets, self-amplified spontaneous emission (SASE) is generated which is transported to the experiment while the electron beam is dumped.

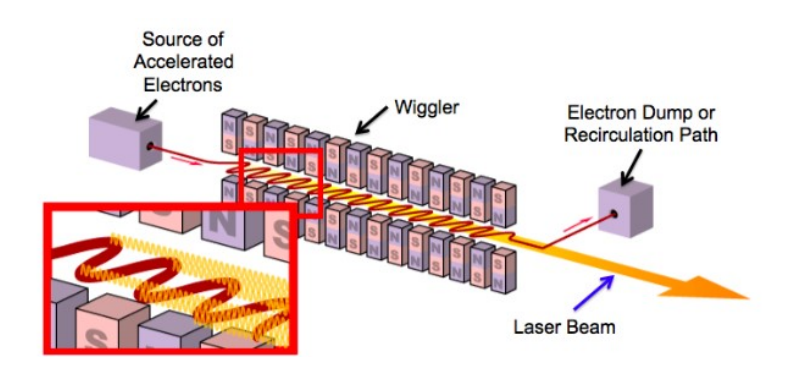


Figure 2: Schematic of a basic free electron laser[2]

Two XFELs are prosecuted by DESY:

- FLASH
- European XFEL

Their specific structures will be explained in the following subsections.

#### 1.1.1. FLASH

The FLASH facility was the world's first short-wavelength free-electron laser facility.[3] It was developed as test facility for the superconducting TESLA-accelerator technology and has a length of 315 m. Today, the facility is used as photon source for two experimental halls with five and six measuring stations (3).[3][14]

By using two independent photocathode lasers, it is possible to create different bunch patterns for two beamlines. This enables the synchronous operation of the beamlines FLASH1 and FLASH2. Before the electrons are sent into the different beamlines, they get accelerated and compressed in seven accelerating modules and two magnetic chicanes.

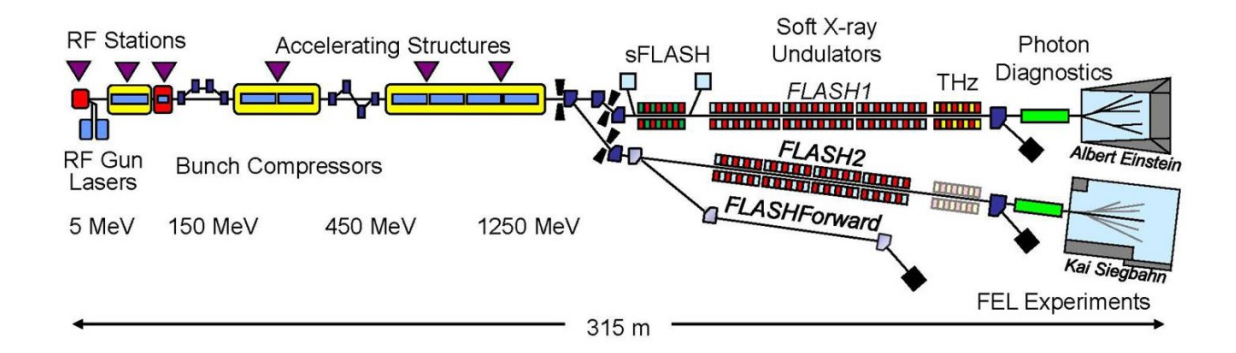


Figure 3: FLASH Layout[3]

#### 1.1.2. European XFEL

The European XFEL (EuXFEL) (fig. 4) is one of the world's brightest XFELs with a peak brilliance of  $5 \cdot 10^{33}$ . [15] The whole facility has a length of 3.4 km and starts on the DESY campus, Hamburg. The experimental hall with currently four different experimental set-ups is located in Schnenefeld, Schleswig-Holstein.

After the injection, the electrons pass a superconducting linear accelerator (LINAC) with a total length of 1.7 km that basically uses the same components as FLASH. Due to the usage of 98 accelerating modules the electron beam can reach up to 17.5 GeV. Afterwards, the electrons enter the SASE sections where 27,000 ultra-short light flashes per second with a wavelength of 0.05 nm to 4.7 nm can be achieved. The photons are sent to the experimental stations whereas the electrons are dumped in a water cooled graphite block. Finally, the scientists can use the light for experiments in various disciplines to explore the world on a femtosecond scale.

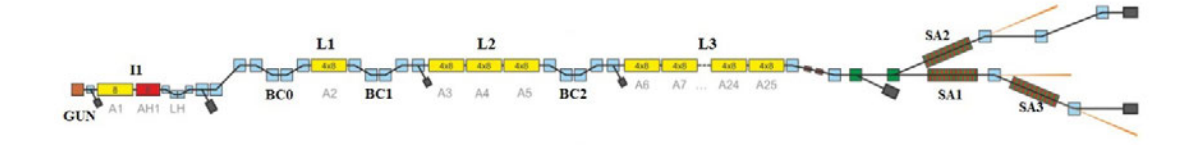


Figure 4: XFEL Layout[4]

#### 1.2. Task

To fulfill the requirements of the experiments of high and stable photon energies, it is crucial to have a reliable SASE process with electron beam parameters that always saty the same, such as compression and energy. For that reason, a good control of the beam in front of the undulators is needed. Hence, the settings in the injector and the accelerating modules, such as gun phase and amplitude as well as sumvoltage and chirp in the

modules, are the enabling factors for successful operation of the system.

To enhance a stable beam with constant properties, various feedback systems are used. This thesis essentially deals with the slow longitudinal feedback system of the FLASH accelaerator which is responsible for the compensation of long term drifts during operation caused by e.g., temperature or humidity changes. The control system currently used works only to a certain state of the machine before it starts to drift. It contains six independent control loops for the FLASH accelerator with the option for nine additional loops [5]. By measuring a response matrix of the machine by applying small changes to the different actuators, a linear control loop is enabled [5]. The response matrix is inverted by singular value deposition (SVD), so that the control system recalculates the necessary actuator changes out of the changes in arrival time and bunch length measured by different monitors [5].

Hitherto, the behavior of the system during operation is not satisfying due to occurring drifts and the subsequent adjustments made by the operators and their experience. For this reason, a closer look into the slow longitudinal feedback is necessary. With focus on the actuators and monitors as closed and dependent system as well as the recalculation of response matrices, a new approach including e.g. nonlinearites should be developed and implemented by using machine learning methods. Due to the similarity of EuXFEL and FLASH, an adaption of the dependencies found at FLASH to the EuXFEL control system is possible.

### 2. Basics and current status

This chapter deals with the different components of the slow longitudinal feedback system and the system itself. To understand the longitudinal feedback in a sufficient way, a basic knowledge about the different diagnostics like

- Laser based synchronization systems
- Toroids
- Beam arrival monitors (BAM)
- Beam compression monitors (BCM)

is necessary. In addition to this, the location of the actuators and monitors as well as the principle of the control system are pointed out.

#### 2.1. Diagnostics

The schematic diagram of the FLASH longitudinal feedback system (fig. 5) shows the layout of the different components for diagnostics for the longitudinal feedback system of FLASH and the accelerating modules as well as the parameters gained from the components. Starting from the electron gun, the functionality of the different diagnostics will be explained in the following subsections.

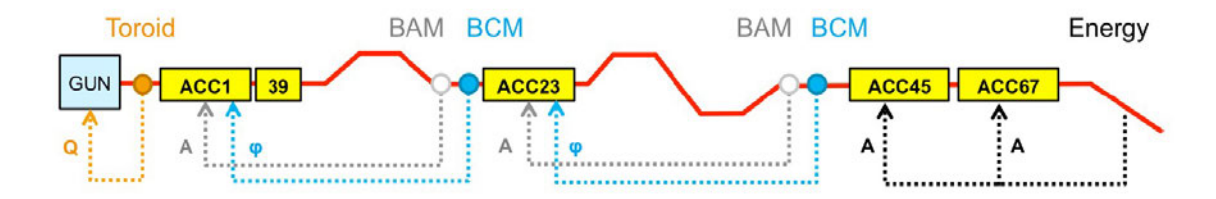


Figure 5: Schematic diagram of FLASH longitudinal feedback[5]

#### 2.1.1. Laser based synchronization systems

To allow a precise control of the accelerator parameters, all components have to run with a higher precision than the demanded measurement precision, in this case within a femtosecond resolution. For this reason, a laser based synchronization system was implemented. A master laser oscillator provides ultra short laser pulses via fibre links to the different components. To compensate environmental influences, the fibers are stabilized with piezo actuators that adjust the length of the fiber according to humidity and temperature by

comparing the reflected part of the pulse with a new pulse.[6]

The master laser oscillator is locked to the radio frequency master oscillator that works as a time reference for other accelerator systems. Both systems are located in a temperature stabilized room to avoid environmental influence. A schematic layout of the whole system is presented in fig. 6.[6]

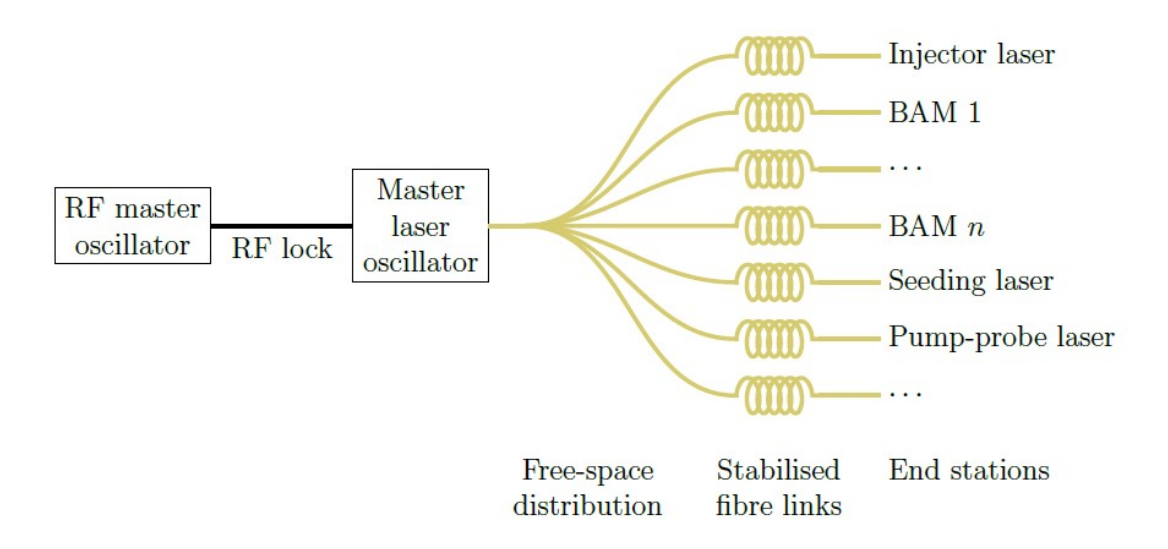


Figure 6: Schematic layout of the laser-based synchronization system[6]

#### 2.1.2. Toroids

To measure the current and the charge of the electron beam, toroids are used. The induced current which appears when a charged particle passes a toroidal core can be used to extract the beam current without distracting the beam itself.[16] For the accelerators FLASH and EuXFEL, a toroid coil works in combination with a frontend device. It has a two channel arrangement with two amplifiers of different gains so that an extended dynamic range of the current can be covered (fig. 7). Then, the signals are provided to a MTCA.4 crate which processes the data.[7]

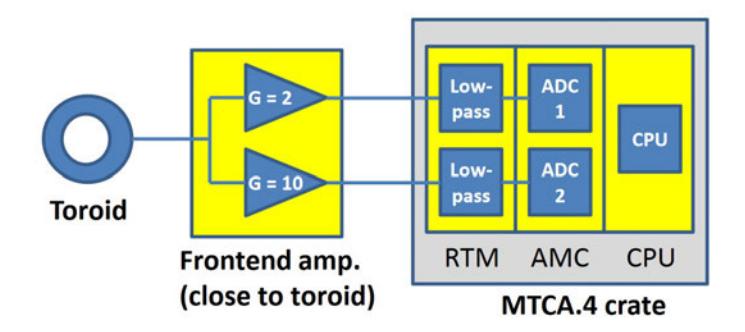


Figure 7: Hardware setup with high dynamic range feature (simplified) system[7]

#### 2.1.3. Beam arrival monitors

Gaining information about the arrival time of the bunch is crucial for the control system because it allows an indirect measurement of the energy of the electron bunches. For that reason, beam arrival monitors are implemented at several positions of both accelerators as shown in fig. 5. By electro-optical modulation of the electric field of the passing electron beam, a comparison to the laser-based synchronization is possible. A schematic of the measurement principle is shown in fig. 8.[6]

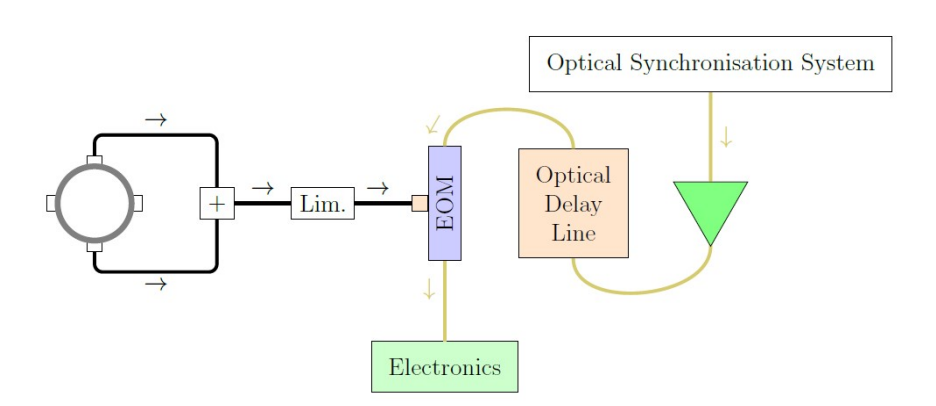


Figure 8: Basic layout of the BAM cabling scheme[6]

There are two opposing pick-ups implemented in the beam pipe which receive the electric field from the beam. Next, the signals are combined so that the orbit dependence of the measured values is reduced. The signal is transferred to an electro-optical modulator (EOM) that adjusts the amplitude of laser pulses to the voltage received. By adding the pulses from the laser-based synchronization to the modulated pulses from the EOM, the timing of the bunch arrival can be calculated with the help of the detector electronics.[6]

#### 2.1.4. Beam compression monitors

After each bunch compression chicane a beam compression monitor is installed (fig. 5). Due to an elliptic aperture with a 45°-angle to the electron beam, coherent diffraction radiation (CDR) is perpendicularly emitted when an electron bunch passes. It does not affect the electron beam.[8]

The perpendicularly emitted CDR exits the beam pipe through a vacuum window made of e.g., diamond or fused silica. Outside of the beam pipe, it hits a mirror that points the radiation through a splitter and several filters towards the detectors that convert it into an electric signal. In order to achieve a larger measurement range, two detectors with different sensitivities are used. Switching the detectors also leads to a different aperture in the beam. A CAD-model is shown in fig. 9, while the whole system is shown in fig.10.[6][8]

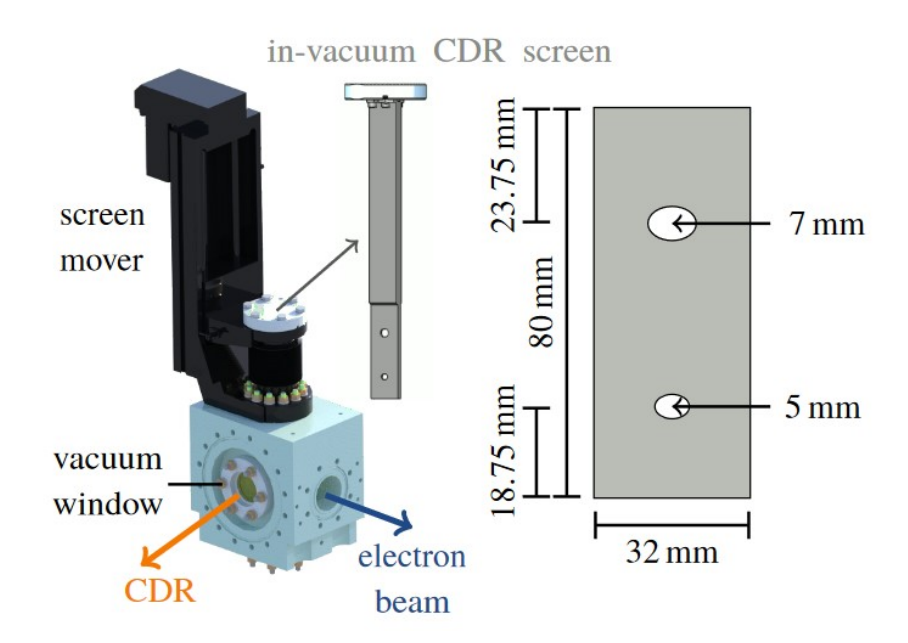


Figure 9: CAD model of the screen station and CDR screen[8]

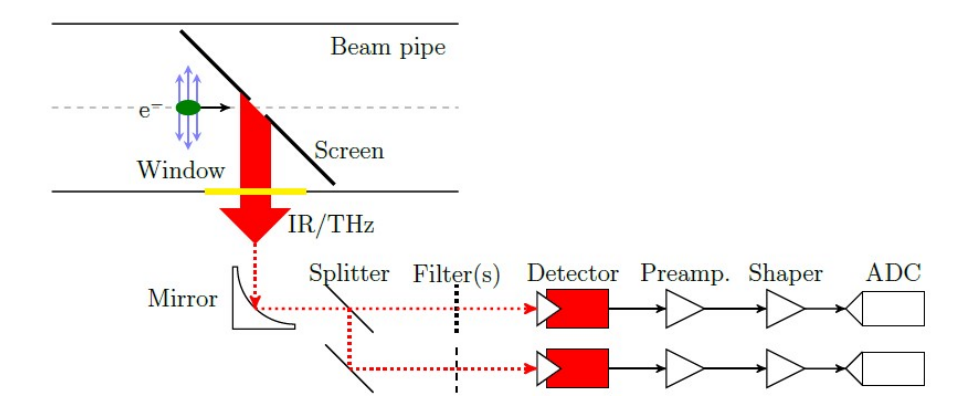


Figure 10: Diffraction radiation measurement with BCM[6]

The spectral intensity of the CDR is dependent on the current profile as well as on the bunch length so that an approximated value for the bunch length can be calculated. This scalar value provided by a BCM does not describe the longitudinal bunch profile completely but can be used for the estimation of the total bunch length, or even for substructures.[6]

# 2.2. Layout of the slow longitudinal Feedback System at FLASH and European XFEL

This chapter deals with the slow longitudinal feedback systems of the EuXFEL and FLASH. Both facilities are similar to each other with only small differences as pointed out in chapter 1.1. In the following subsections, the FLASH feedback system with its actuators and monitors will be explained, starting from the electron gun and moving towards the experimental halls. Finally, the differences to the EuXFEL will be pointed out.

#### 2.2.1. Gun

To extract electrons from a cathode material, a laser is used. By hitting the cathode material with a pulsed laser, a certain number of electrons (bunch) exit the gun within a short time window to get accelerated in the modules further downstream (fig. 11).



Figure 11: Gun[9]

For FLASH, two lasers are used to provide the different branches with bunches of different pattern, charge and phase. Both lasers are connected to the same fibre which leads their pulses to the cathode material as shown in fig. 12.

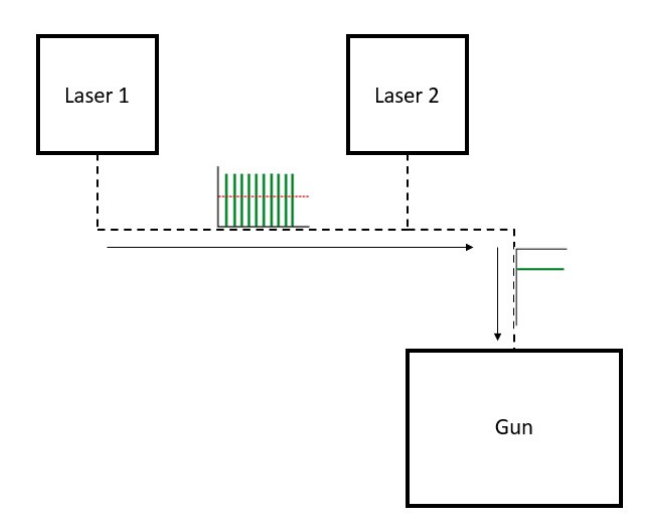


Figure 12: Laser schematic

The machine runs with 10Hz. There are certain time slots for bunching available, called beam regions. For the longitudinal feedback system, a toroid right after the gun is used to gain information about the charge of the electron bunch so that the amplitudes of the lasers can be adjusted by in- or decreasing the voltage. In addition to this, the phase of the laser can be tuned by using a BAM which is located after the first accelerating modules. A possible sequel of amplitude and phase over time is shown in fig. 13. The different beam regions are colored blue (FLASH1) and orange (FLASH2).

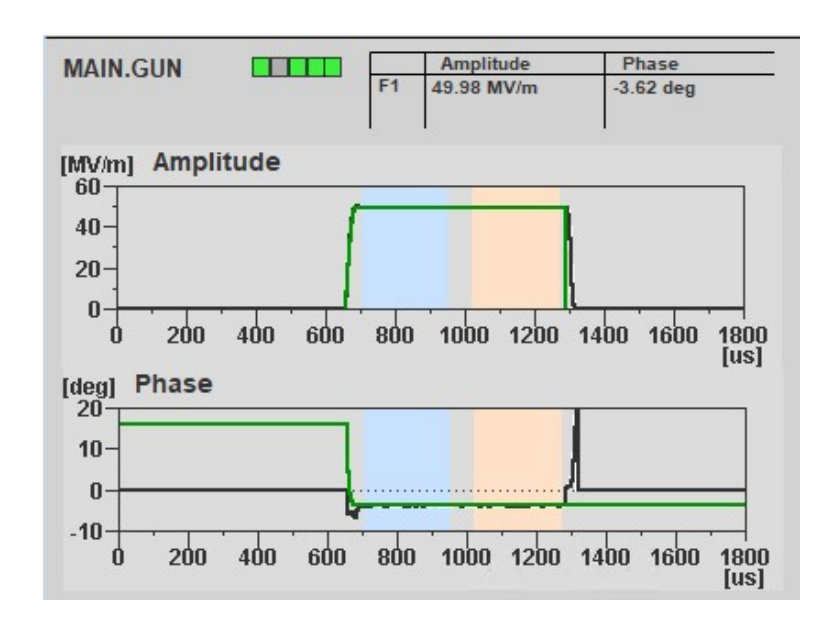


Figure 13: Gun amplitude and phase over time

#### 2.2.2. First accelerating modules

After a bunch exits the gun, it enters the first accelerating modules where radio frequency (RF) is applied to the bunch in superconducting cavities. By increasing the electric field of the RF, the bunch gets accelerated. The bunch itself has got a significant length that leads to a different acceleration of single electrons within a bunch depending on their location when the radio frequency is applied. Fig. 14 shows the dependency of the applied electric field E and the phase  $\phi$ . The influence over the time t is shown in fig. 15. The change of the electric field  $\delta E$  over the time is called chirp.

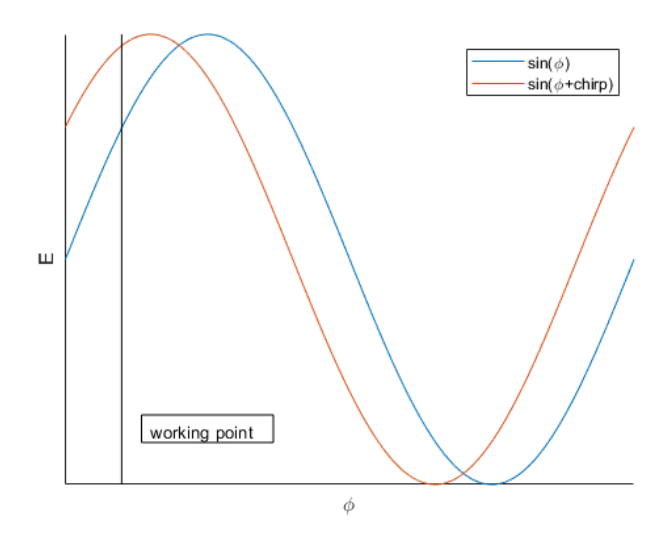


Figure 14: Energy E over phase  $\phi$ , black line is the desired working point

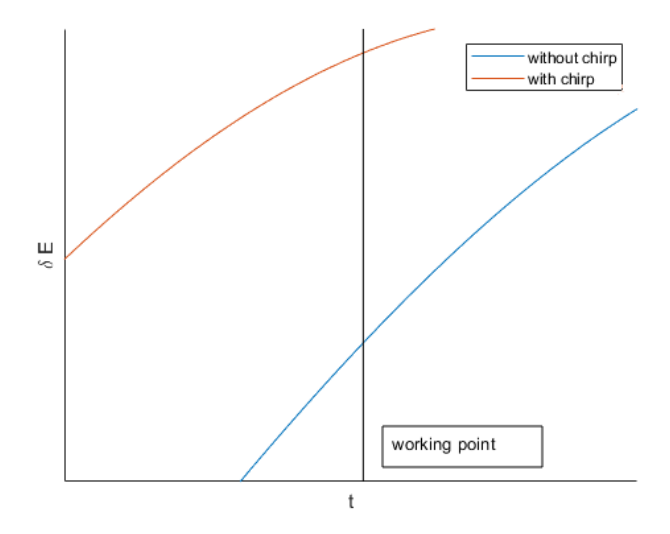


Figure 15: Energy change E over time t in working point

The accelerating modules (fig. 16) work as actuators for the control system, but the tunable parameters are not phase and amplitude of the applied radio frequency. Instead, the chirp and the voltage applied over the whole structure are used and automatically recomputed to phase and amplitude. The beam properties generated in the accelerating modules are monitored by a BAM for the amplitude or sumvoltage downstream of the accelerating modules and a BCM for the phase or chirp after the first bunch compressor.

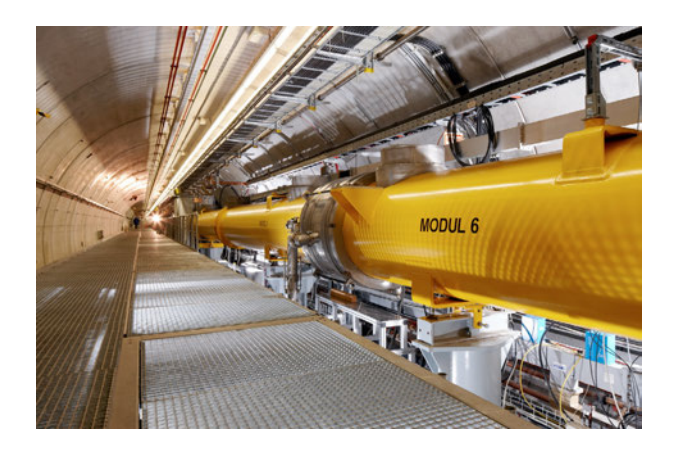


Figure 16: Accelerating modules[9]

#### 2.2.3. First bunch compressor

After leaving the first accelerating modules, the beam has several disadvantageous properties: On the one hand, the bunches are streched and need to be compressed. On the other hand, there is no exact Gaussian distribution of the electrons over the time (fig. 17).

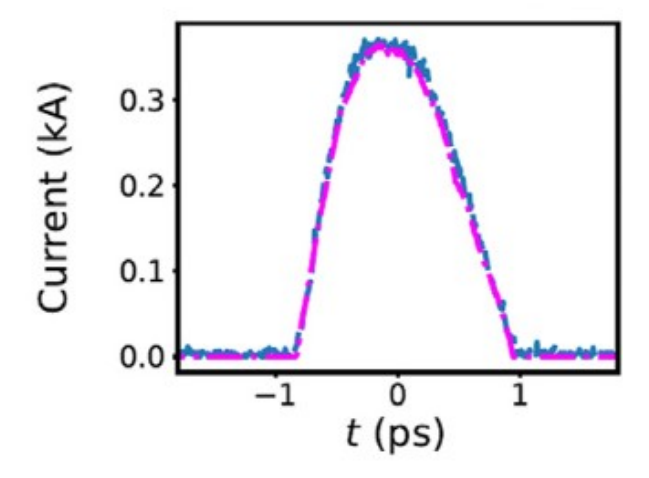


Figure 17: Current distribution over a time[10]

As mentioned in chapter 2.2.2, the electrons leave the accelerating modules with different energies. Under the assumption that all electrons are moving very close to the speed of light, it is now possible to compress the bunch by sending it through a magnetic chicane as shown in fig. 18. The electrons with high energies are less distracted by the magnets than the ones with lower energies whose way become longer so that the bunch will be compressed.

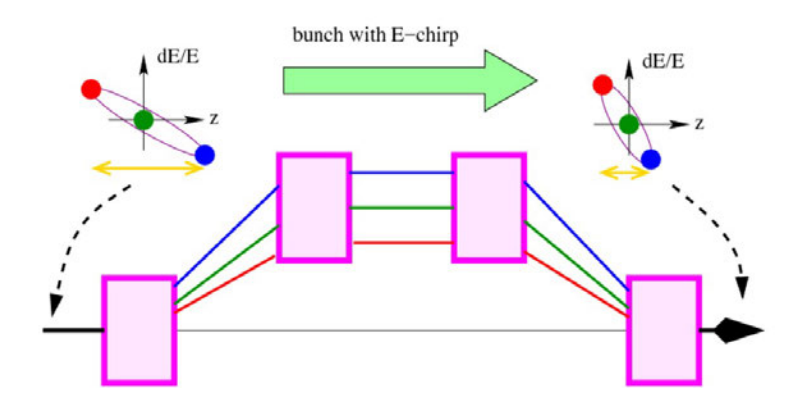


Figure 18: Magnetic chicane [11]

The beam arrival time corresponds directly with the chirp and the sumvoltage as shown in fig. 18. The chicane cannot be tuned because the magnets run with constant current and power. To allow a variation of the bunch compression, the information gained from the BAM and the BCM after the chicane is provided to the accelerating modules and can be used to adapt the chirp and the sumvoltage for the first modules. For the compression of the beam, the chirp parameter is dominant.

#### 2.2.4. Accelerating modules 2,3 and second bunch compressor

After the first bunch compressor, the layout repeats. The next accelerating modules can be found further downstream. They are also controlled by a BAM and a BCM after the following second bunch compressor chicane. Here, it is also possible to tune the beam properties like chirp and sumvolatage to compress and accelerate the bunches in the direction of the properties desired by the experiments.

#### 2.2.5. Accelerating modules 4,5 and 6,7

For the last accelerating modules only the sumvoltage is needed for operation because the bunches are already in final compression. To monitor the acceleration of the bunches, BAMs are used as well as beam position monitors. Depending of the orbit of several beam position monitors, the energy of the beam can be recalculated and adapted.

#### 2.2.6. Differences between FLASH and EuXFEL

In general, both machines work with the same principles but due to the higher photon energies provided by EuXFEL, the electrons need more energy, too. For that reason, more accelerating modules are needed (in total 98). This large amount of modules leads to a subdivision with more groups for a specific sumvoltage and chirp control. Furthermore, the EuXFEL has an additional bunch compressor. Hence, the monitor layout is also slightly different, the EuXFEL has more monitors but at similar positions (e.g. BCM behind bunch compressors).

### 2.3. Control system data

The control system allocates each measured or set and time dependent value to a bunch train number. Furthermore, there are two different types of data. On the one hand, there are single values e.g. for the accelerating modules, on the other hand, there are spectral values e.g. of the monitors for every bunch train which are written into the control system. Both types are shown and explained in the following subsections.

#### 2.3.1. Monitors

The monitors mentioned in chapter 2.1 provide data for every bunch within a bunch train. These spectra are used for both beam regions, so that the values can vary strongly within a bunch train. Due to the fact that the different beam regions are aligned to a specific time slot, it is possible to sort the different bunches. A typical spectrum for a BCM is

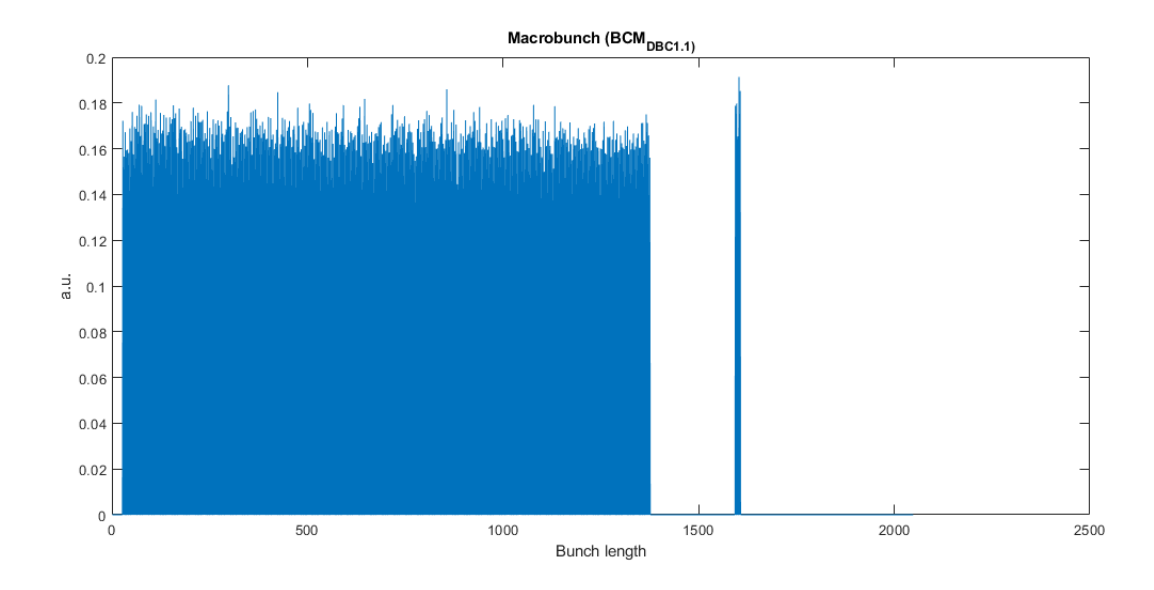
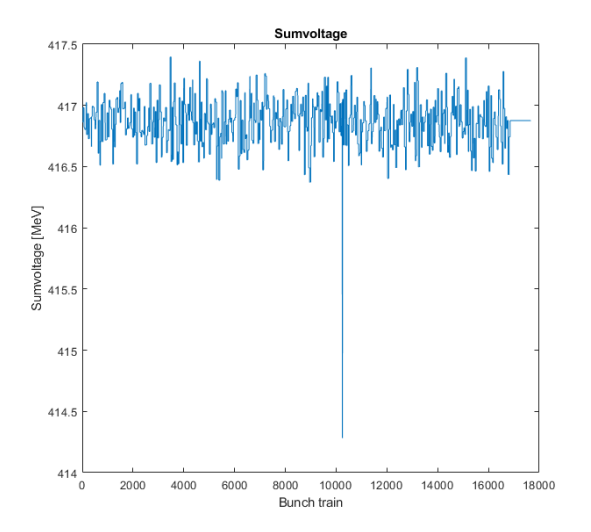


Figure 19: Macrobunch BCM downstream of bunch compressor 1

The different beam regions with the different compression levels can be seen in fig. 19. In this case, very few bunches are needed for FLASH2. When spectra are used for control loops, one has to decide which value should be used for the control e.g. the first, the last or the mean value. The current control system works only with the first entries.

#### 2.3.2. Actuators

Corresponding to the monitors mentioned above, fig. 20 shows the values of the accelerating modules ACC23 at the same time (identical TrainID). There is only a single value available per bunch train so that a decision of the right value is not needed.



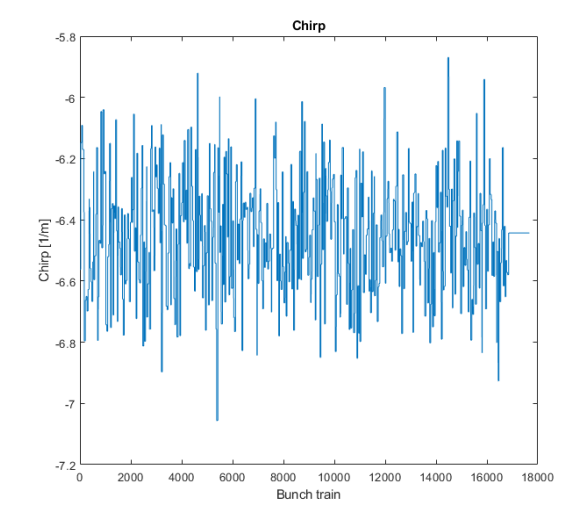


Figure 20: Sumvoltage and chirp values of ACC23

### 2.4. Slow longitudinal feedback control system

In general, there are up to six feedback loops as shown in fig. 5. The changes of the monitors  $\delta m$  shall be compensated with the change (adjustment) of the actuators  $\delta a$ . Under the assumption of small changes, a linear response of the monitors can be expected. By inverting the responses R of all monitors, a global correction can be achieved as shown in eq. 2.1.[5]

$$\delta a = R^{-1} \cdot \delta m \tag{2.1}$$

The full global equation for all relevant monitors an actuators is shown in the following eq. 2.2.[5]

$$\begin{bmatrix} \delta ampl_{ACC1} \\ \delta phase_{ACC1} \\ \delta ampl_{ACC39} \\ \delta phase_{ACC39} \\ \delta phase_{ACC39} \\ \delta phase_{ACC39} \\ \delta phase_{ACC23} \\ \delta phase_{ACC23} \\ \delta phase_{ACC45} \\ \delta phase_{ACC45} \\ \delta phase_{ACC45} \\ \delta phase_{ACC67} \end{bmatrix} = \begin{bmatrix} R_{11} & R_{12} & R_{13} & R_{14} & R_{15} & R_{16} & R_{17} & R_{18} & R_{19} & R_{110} \\ R_{21} & R_{22} & R_{23} & R_{24} & R_{25} & R_{26} & R_{27} & R_{28} & R_{29} & R_{210} \\ R_{31} & R_{32} & R_{33} & R_{34} & R_{35} & R_{36} & R_{37} & R_{38} & R_{39} & R_{310} \\ R_{41} & R_{42} & R_{43} & R_{44} & R_{45} & R_{46} & R_{47} & R_{48} & R_{49} & R_{410} \\ R_{51} & R_{52} & R_{53} & R_{54} & R_{55} & R_{56} & R_{57} & R_{58} & R_{59} & R_{510} \\ R_{61} & R_{62} & R_{63} & R_{64} & R_{65} & R_{66} & R_{67} & R_{68} & R_{69} & R_{610} \\ R_{71} & R_{72} & R_{73} & R_{74} & R_{75} & R_{76} & R_{77} & R_{78} & R_{79} & R_{710} \\ R_{81} & R_{82} & R_{83} & R_{84} & R_{85} & R_{86} & R_{87} & R_{88} & R_{89} & R_{810} \\ R_{91} & R_{92} & R_{93} & R_{94} & R_{95} & R_{96} & R_{97} & R_{98} & R_{99} & R_{910} \end{bmatrix}^{-1} \begin{bmatrix} \delta BAM_{1UBC2} \\ \delta BAM_{1UBC2} \\ \delta BAM_{1BC2} \\ \delta BCM_{BC2(fine)} \\ \delta BCM_{BC2(fine)} \\ \delta BCM_{BC3(fine)} \\ \delta BCM_{BC3(fine)} \\ \delta BCM_{BC3(coarse)} \\ \delta BAM_{18ACC7} \\ \delta Energy_{Dogleg} \end{bmatrix}$$

27

For the calculation of the inverse response matrix, singular value decomposition (SVD) is applied to generate the matrix  $R^+$ . To simplify this (often) fully filled matrix, a binary matrix B is multiplied element-wise (Hadamard product) to allow a single loop combination of actuators and monitors for the feedback control (C) chosen by the operator (eq. 2.3).[5]

$$C = B \circ R^+ \tag{2.3}$$

After all the simplifications mentioned above, this leads to eq. 2.4 that is implemented in the control system.

$$\delta a = C \cdot \delta m \tag{2.4}$$

Several measured response matrices depending on the beam energies can be found in the expert panel of the control system (fig. 21). Screenshots of the actuators and monitors as well as their combination (matrix B) are provided in fig. 22 and fig. 23. Usually, it does not change so that smaller adjustments can be applied in a simplified panel for the operators of the machine.



Figure 21: Response Matrix FLASH expert panel

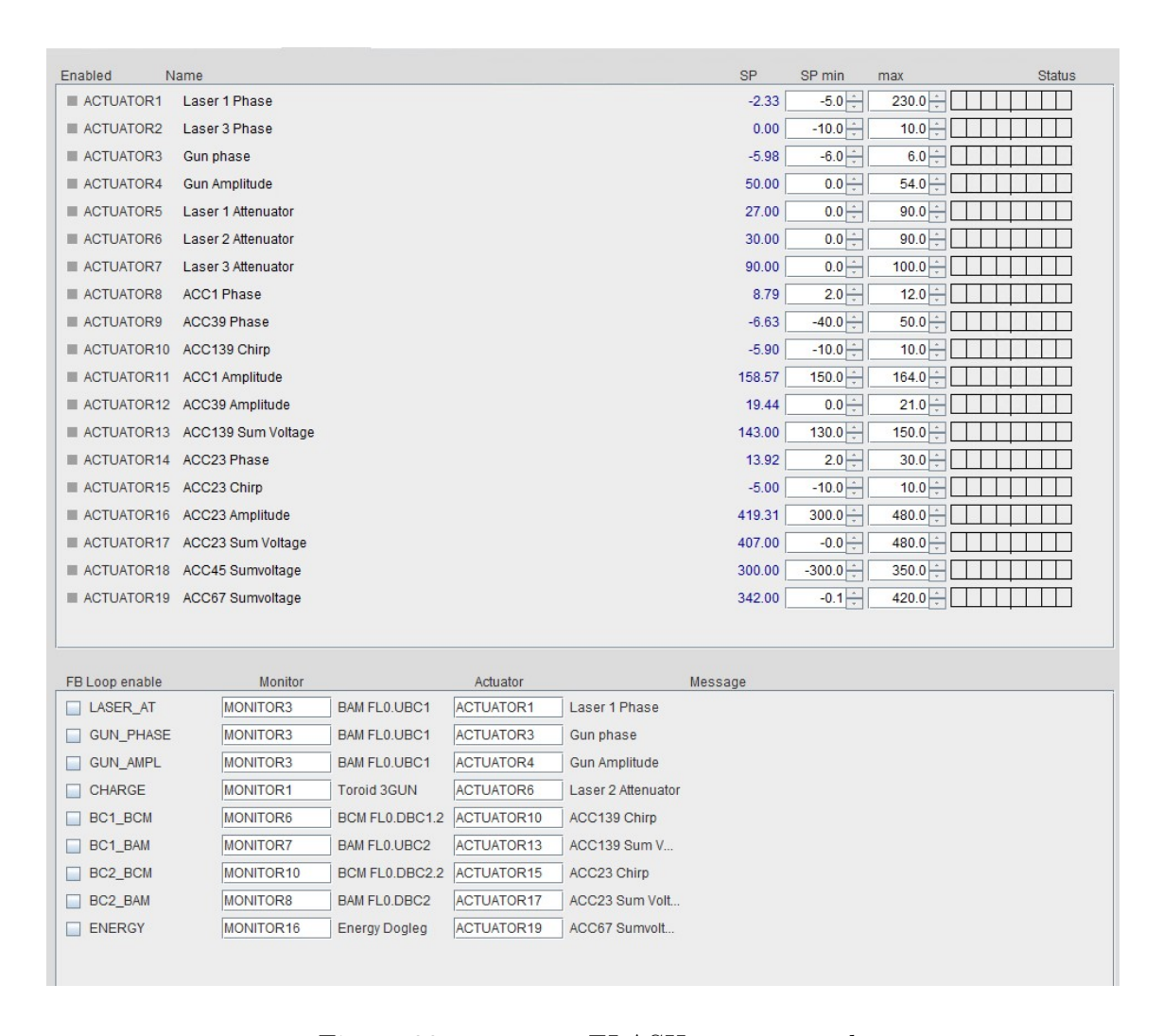


Figure 22: actuators FLASH expert panel

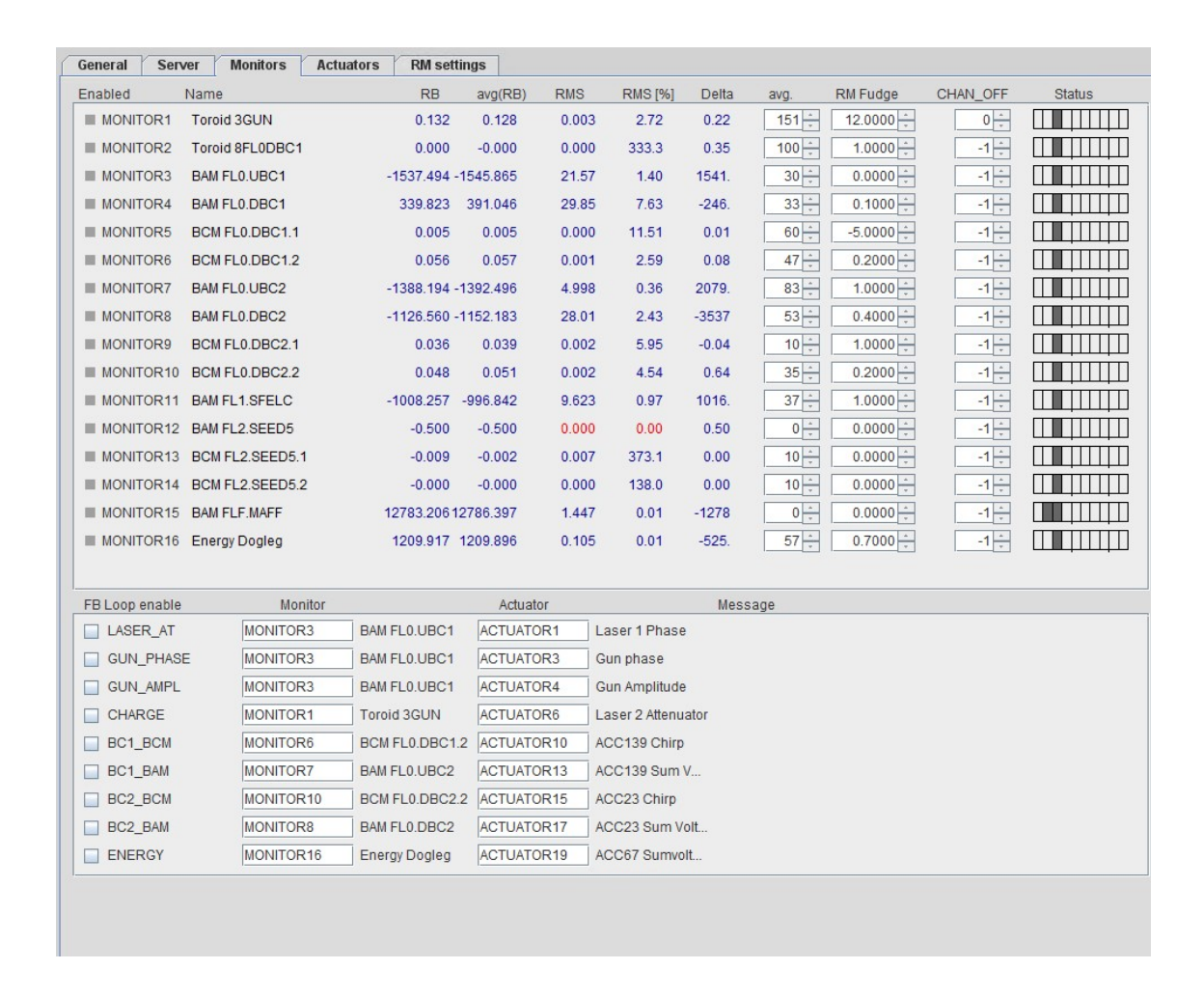


Figure 23: monitors FLASH expert panel

For the operators, another panel was prepared as shown in fig. 24. There, the monitor/actuator combination is displayed together with the information whether the feedback control is enabled. Furthermore, the number of samples to build an average value for each of the monitors can be set and will be processed by the control system. This procedure has the advantage to keep the system stabilized even if single events with extreme values occur. Finally, there is the opportunity to change certain values of the response matrix by applying a gain factor (RM Fudge) on single entries of the response matrix to adapt it to the current machine operation mode.



Figure 24: slow RF Feedback Control Panel

### 3. Analysis of the existing system

In this chapter, the functionality of the existing mathematical system will be analyzed with the given matrices from chapter 2.4. The reaction of the model is compared to the real system so that similarities and differences can be pointed out to gain information about the accuracy and the stability of the current control approach.

### 3.1. Simplified model

To simulate the slow longitudinal feedback system according to [5], the matrix approach from chapter 2.4 is used without regarding the averaged values as well as the gain factors. With the starting point of all monitor changes  $\delta m$  and the measured response matrix R and its simplified inverse C it is possible to calculate the first change of all actuators to compensate the applied change of the beam properties as described in chapter 2.4. For the first monitor values, the corresponding entries of the control system were chosen and the changes actuators calculated. With the new actuator values now given  $\delta a$ , a linearized answer of the system's monitors can be calculated like shown in the following algorithm 1.

```
Algorithm 1 Linearized, simplified model
```

```
1: procedure ACTUATORS(\delta m, R, B, n)
        C \leftarrow R^{-1} \circ B
2:
         for i = 1 : n \text{ do}
3:
             \delta a \leftarrow C \cdot \delta m
                                                                                                ▷ new actuator values
4:
             \delta m \leftarrow R \cdot \delta a
5:
                                                                                                 ▷ new monitor values
        end for
6:
        plot \delta a, \delta m
7:
8: end procedure
```

The matrices-based simulation shows that both actuator and monitor values start to diverge quickly by oscillating with increasing amplitudes. This does not cover the behavior of the real system, hence the actuator values are many decades above the highest possible values and do not show a slow drifting behavior. A visualization of the data can be found in appendix A.

#### 3.2. Extended model

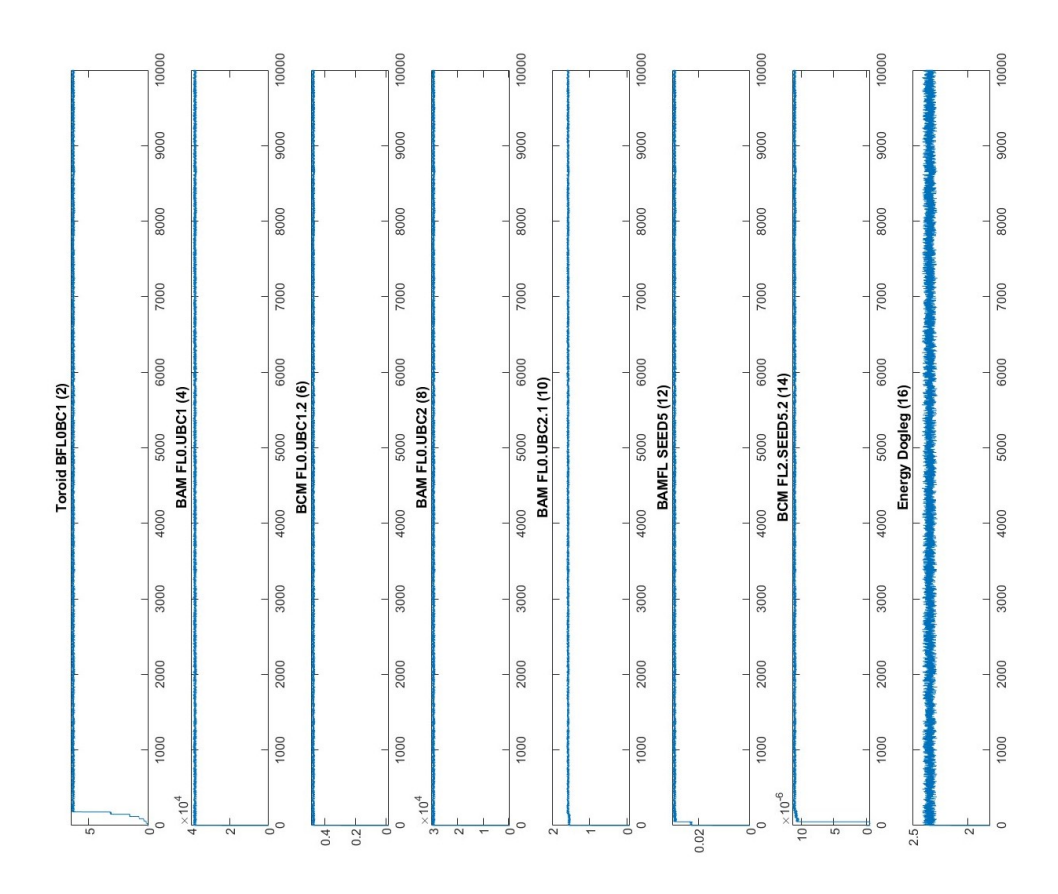
To adapt the simplified model to the current control system, additional functionalities are applied to the existing control loop introduced in algorithm 1. Firstly, a running average

is implemented for each monitor value so that single events do not effect the control loop massively. The values for each monitor can be found in a vector avg. Furthermore, the gain factor (RM fudge) is added with the help of a matrix F that is multiplied elementwise to the simplified response matrix C. Lastly, a matrix limits with the actuator limits is given by the operator. avg and limits were extracted from the control system while F is filled with ones. The entire extended approach for the first actuator/monitor combination is shown in the algorithm 2.

By extending the model according to algorithm 2 and after applying a random jitter of up to three percent to the monitor values, the following result for the monitors occurs (fig. 25). The corresponding actuator values are shown in fig. 26. It can be shown, that many actuators drive quickly towards their limits and according to the linear model, the monitor changes are kept stable as well. This behavior does not represent the real system hence it diverges like the simplified approach with the difference that the changes are restricted to the boundaries of the actuators.

#### Algorithm 2 Linearized, extended model

```
1: procedure ACTUATORS(\delta m, R, B, n, F, avg, limits)
          C \leftarrow R^{-1} \circ B \circ F
 2:
          for i = 1 : n \text{ do}
 3:
 4:
               \delta a1(i) \leftarrow \delta a(1)
 5:
               \delta m1(i) \leftarrow \delta m(1)
 6:
 7:
               if \frac{\delta m(1)}{avg(1)} is natural and actuator/monitor combination is nan then
 8:
 9:
                    buffer1 \leftarrow 0
10:
11:
                    for j = length(\delta m1) - avg(1) + 1: length(\delta m1(j)) do
12:
13:
                         buffer1 \leftarrow buffer1 + \delta m1(j)
14:
15:
                    end for
16:
17:
                    \bar{\delta m1} \leftarrow \frac{1}{avg(1)} \cdot buffer1
18:
                    \delta m1(i) \leftarrow \bar{\delta m1}
19:
                    \delta m(1) \leftarrow \delta m1(i)
20:
                    \delta a1_{new} \leftarrow C \cdot M
21:
22:
                    if limits(1,1) \leq \delta a1_{new}(Actuator1) and limits(1,2) \geq \delta a1_{new}(Actuator1)
23:
     then
24:
                         \delta a(Actuator1) \leftarrow \delta a1_{new}(Actuator1)
25:
26:
                    else
27:
28:
                         \delta a(Actuator1) \leftarrow \delta a(Actuator1)
29:
30:
                    end if
31:
               end if
32:
33:
          end for
          plot \delta a, \delta m
34:
35: end procedure
```



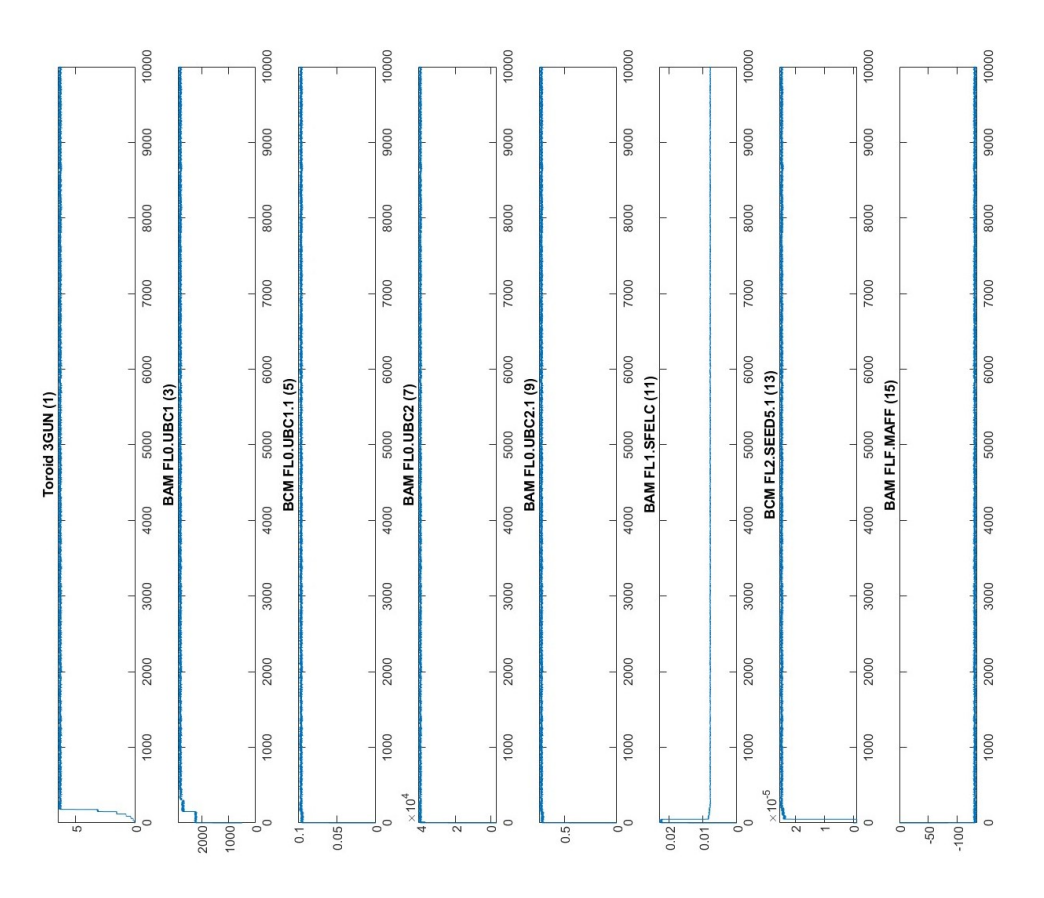
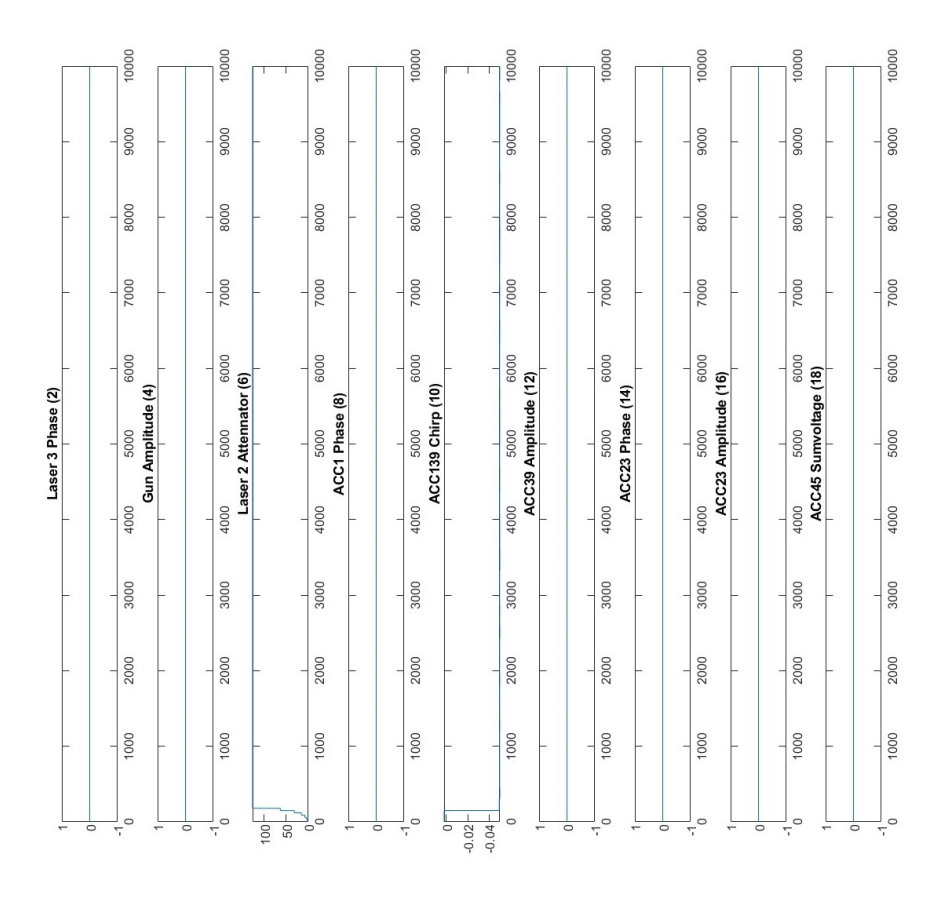


Figure 25: results for all monitors using the simplified response matrix C with the extended model  ${\bf 35}$ 



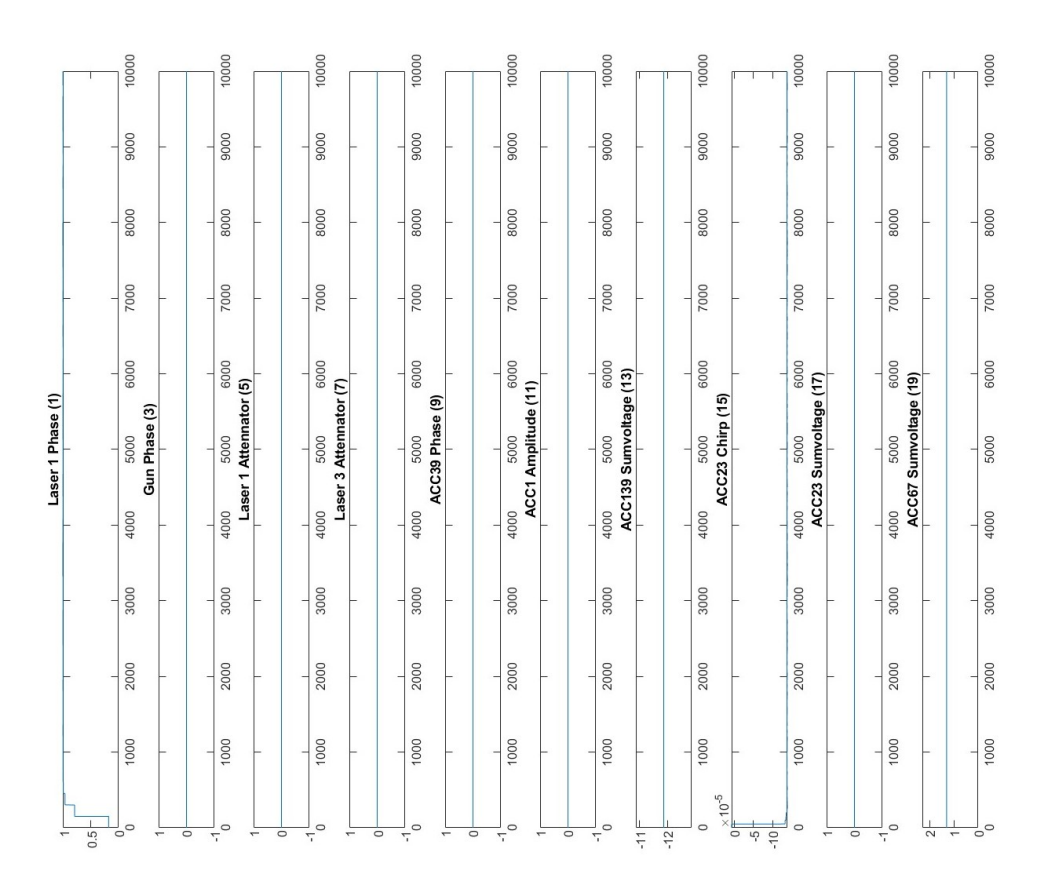


Figure 26: results for all actuators using the simplified response matrix C with the extended model  ${\it 36}$ 

In comparison to the results of the simulation with the simplified inverse response matrix C, the next simulation investigates the linearized system reaction with the full inverse response matrix R. The simplification of the response matrix leads to very different results in the simulation and it occurs that both calculated system reactions are hardly comparable. The values for the actuators do not run directly into their limits and the monitor changes move according to them. These differences could be caused by numerical errors during the inversion of the matrix R or direct linear coupling between actuator and monitor values in the simulation. The linearization can not be validated on a small scale due to a diverging model which is only stopped by its actuator limits. A visualization of the system with fully inverted matrix can be found in appendix A.

For this reasons, an optimization with the given information is not leading towards an acceptable solution. Regarding the fact that many actuator/monitor combinations, actuator limits, averaged values and fudge factors have to be chosen by experience and with the introduced model uncertainty, it is questionable whether a sufficient working solution for the problem can be found. Before the optimization of the feedback loop can be realized, more information about the system's behavior should be collected.

The linearization of the system's answer as well as the simplification of the response matrix have lead to different results. The variation in the responses might be a hint towards numerical problems in the real system in which case the operators have to adapt the values fudge factor and the actuators which are enabled in the control loops frequently. Summarizing, the measured response matrix R is insufficient for description of the system using the presented algorithms. For the following chapters of this report, this approach will not further be part of the scope and data driven approaches will be tested.

# Machine learning approaches

In this chapter, the machine learning approaches used and the tools needed are introduced. Static and dynamic methods for system identification will be explained as well as convex optimization.

### 4.1. Regression

To find an optimal fit with functions of different order, regression models can be applied to the given data set. In an one-dimensional and linear case with the features x and y and the coefficients a and b, the following equation 4.1 shall describe the model. [17]

$$y = a \cdot x + b \tag{4.1}$$

Now, a system of equations with the length of the data set n can be created.[17]

$$y_n = a \cdot x_n + b \tag{4.2}$$

Subtracting the original feature values  $\hat{y}$  from the right side of eq. 4.2 leads to the mean squared error  $c_{MSE}$  (MSE) after summation.[17]

$$c_{MSE}(a,b) = \sum_{k=1}^{n} ((a \cdot x_k + b) - \hat{y_k})^2$$
 (4.3)

Minimizing the mean square error delivers the best linear fit for the given data set. After deviation of eq. 4.3 to eqs. 4.4-4.5 the best fit coefficients  $\hat{a}$  and b are calculated (eqs. 4.6-4.7).[17]

$$\frac{\partial c_{MSE}(a,b)}{\partial a} = 0 (4.4)$$

$$\frac{\partial c_{MSE}(a,b)}{\partial b} = 0 (4.5)$$

$$\hat{a} = a \left( \frac{\partial c_{MSE}(a, b)}{\partial a} = 0 \right) \tag{4.6}$$

$$\frac{\partial c_{MSE}(a,b)}{\partial a} = 0$$

$$\frac{\partial c_{MSE}(a,b)}{\partial b} = 0$$

$$\hat{a} = a \left( \frac{\partial c_{MSE}(a,b)}{\partial a} = 0 \right)$$

$$\hat{b} = b \left( \frac{\partial c_{MSE}(a,b)}{\partial b} = 0 \right)$$

$$(4.4)$$

$$(4.5)$$

$$(4.6)$$

Transferring the principle to higher dimensional problems e.g., with multiple actuators and multiple monitors, makes a matrix notation necessary. With the vectors  $\delta m$  for the changes of the monitors m (size m) and  $\delta a$  for the changes of the actuators a from the original set point (size n), a coefficient matrix R with the size  $m \times n$  is needed (eqs. 4.8-4.9. A term for the static offset like in eq. 4.1 is here neglicated because only the changes to the working point are considered. This relationship is shown in eq. 4.10.

$$\delta m = m_i - m_0 \tag{4.8}$$

$$\delta a = a_i - a_0 \tag{4.9}$$

$$\delta m = R \cdot \delta a \tag{4.10}$$

The following least square problem can be described with the following eq. 4.13 where M is the coefficient matrix to be optimized using the Frobenius norm. Furthermore, all set points are combined to the matrices  $\delta \tilde{m}$  and  $\delta \tilde{a}$  like shown in eqs. 4.11-4.12. [18]

$$\tilde{\delta m} = [\delta m_1, \delta m_2, \delta m_3, ..., \delta m_n] \tag{4.11}$$

$$\tilde{\delta a} = [\delta a_1, \delta a_2, \delta a_3, ..., \delta a_n] \tag{4.12}$$

$$R = \operatorname{argmin}_{M \in R^{m \times n}} ||\tilde{\delta m} - M\tilde{\delta a}||_{F}$$

$$\tag{4.13}$$

Instead of the Frobenius norm, other norms, like the Euclidean norm, can also be applied. [18]

The approach described above can be extended by adding additional functions like the higher polynomials, exponential functions, logarithmic functions etc. to the actuator values so that the coefficient matrix grows as well as the computation time. Eq. 4.14 shows the dependency of the coefficient matrix R, the change of the monitor values  $\delta m$  and the different approaches for  $\delta a$  combined in the vector u.

$$\delta m = R \cdot u(1, \delta a, \delta a^2, e^{\delta a}, \log(\delta_a), \dots)$$
(4.14)

Now, the procedure can be executed like in the linear regression.

# 4.2. Sparse identification of nonlinear dynamics (SINDy)

For the identification of an unknown dynamic system, the so called SINDy (sparse identification of nonlinear dynamics) algorithm can be applied. With the help of the algorithm, the governing equations of a dynamic system can be estimated from measured data. A main assumption of the algorithm is that the only a few terms are sufficient for an accurate identification of the system whereas most of the other terms are negligible and can

be set to 0 in the corresponding matrix. [12][19]

For high dimensional, nonlinear problems, combinatric brute-force methods were state of the art for a very long time. For that reason, system identification needed a lot of computational power and was hardly usable for multidimensional problems. The progress in nonlinear optimization nowadays allows for the performance of nonlinear optimization algorithms with huge data sets. [12]

Today, algorithms like DMD (dynamic mode decomposition) with a linear, dynamic regression are dominant. Their disadvantage is that the functions have to be estimated from the form of the given problem. SINDy results in a sparse, nonlinear regression which automatically finds the relevant terms of the system's behavior. [12]

A multidimensional, measured data set  $y \in \mathbb{R}^m$  might be represented by a linear combination of different library terms  $\Theta \in \mathbb{R}^{m \times p}$  (feature matrix). The combination of these terms is given by the vector  $\xi \in \mathbb{R}^p$ . This relationship is shown in eq. 4.15. [12]

$$y = \Theta \xi \tag{4.15}$$

A standard regression for solving  $\xi$  would lead to a non-zero solution for each element of the library matrix. Performing an  $L^1$ -regularization with the weighting factor  $\lambda$  and using the euclidean norm results in the following LASSO-regression (eq. 4.16) [12]:

$$\xi = \underset{\xi'}{argmin} ||\Theta \xi' - y||_2 + \lambda ||\xi'||_1 \tag{4.16}$$

The goal of the algorithm is to show the behavior of a a nonlinear dynamic system with different states x and the time-based deviation  $\dot{x}$ . [12]

$$\dot{x} = f(x(t)) \tag{4.17}$$

The state of the system at the time t is represented by the vector  $x(t) = [x_1(t)...x_n(t)]^T \in \mathbb{R}^n$ , at the same time the dynamic boundaries are given by the function f(x(t)) that define the system equations (eq. 4.17). [12]

To gain the function f(x(t)) of eq. 4.17 from a data set, the states and their time-based deviations are aligned as demonstrated in the following equations (eqs. 4.18-4.19) [12]:

$$X = \begin{bmatrix} x^{T}(t_{1}) \\ x^{T}(t_{2}) \\ \vdots \\ x^{T}(t_{m}) \end{bmatrix} = \begin{bmatrix} x_{1}(t_{1}) & x_{2}(t_{1}) & \cdots & x_{n}(t_{1}) \\ x_{1}(t_{2}) & x_{2}(t_{2}) & \cdots & x_{n}(t_{2}) \\ \vdots & \vdots & \ddots & \vdots \\ x_{1}(t_{m}) & x_{2}(t_{m}) & \cdots & x_{n}(t_{m}) \end{bmatrix}$$
(4.18)

$$\dot{X} = \begin{bmatrix} \dot{x}^{T}(t_{1}) \\ \dot{x}^{T}(t_{2}) \\ \vdots \\ \dot{x}^{T}(t_{m}) \end{bmatrix} = \begin{bmatrix} \dot{x}_{1}(t_{1}) & \dot{x}_{2}(t_{1}) & \cdots & \dot{x}_{n}(t_{1}) \\ \dot{x}_{1}(t_{2}) & \dot{x}_{2}(t_{2}) & \cdots & \dot{x}_{n}(t_{2}) \\ \vdots & \vdots & \ddots & \vdots \\ \dot{x}_{1}(t_{m}) & \dot{x}_{2}(t_{m}) & \cdots & \dot{x}_{n}(t_{m}) \end{bmatrix}$$
(4.19)

Now, the feature matrix can be built with polynomials of different orders as well as other functions like trigonometric functions (eq. 4.20). [12]

The entry for polynomials of second degree (P2) would look like shown in eq. 4.21. [12]

$$X^{P2} = \begin{bmatrix} x_1^2(t_1) & x_1(t_1)x_2(t_1) & \cdots & x_2^2(t_1) & x_2(t_1)x_3(t_1) & \cdots & x_n^2(t_1) \\ x_1^2(t_2) & x_1(t_2)x_2(t_2) & \cdots & x_2^2(t_2) & x_2(t_2)x_3(t_2) & \cdots & x_n^2(t_2) \\ \vdots & \vdots & \ddots & \vdots & \vdots & \ddots & \vdots \\ x_1^2(t_m) & x_1(t_m)x_2(t_m) & \cdots & x_2^2(t_m) & x_2(t_m)x_3(t_m) & \cdots & x_n^2(t_m) \end{bmatrix}$$
(4.21)

Each column of the library matrix  $\Theta(X)$  represents a candidate function for the left side of eq. 4.22, the sparse vectors  $\xi$  are combined to the matrix  $\Xi$  that controls the terms of the (nonlinear) polynomials. [12]

$$\dot{X} = \Theta(X)\Xi \tag{4.22}$$

As a solution for the whole problem and to identify the system, the following equation can be solved (eq. 4.23). The matrix x contains the symbolic functions. [12]

$$\dot{x} = f(x) = \Xi^T(\Theta(x^T))^T \tag{4.23}$$

To reduce the computational time, the convex optimization has recently been replaced by a sequential least squares approach. The accuracy of the system identification is hardly influenced and for certain problems it is advantageous. The algorithm performs a linear least squares fit with an additional cut-off value  $\lambda$  which converts every entry that is  $<\lambda$  to zero. This procedure is repeated several times until a certain number of iterations is reached and the result converged. A visualization of the algorithms principle is shown in fig. 27 [12]

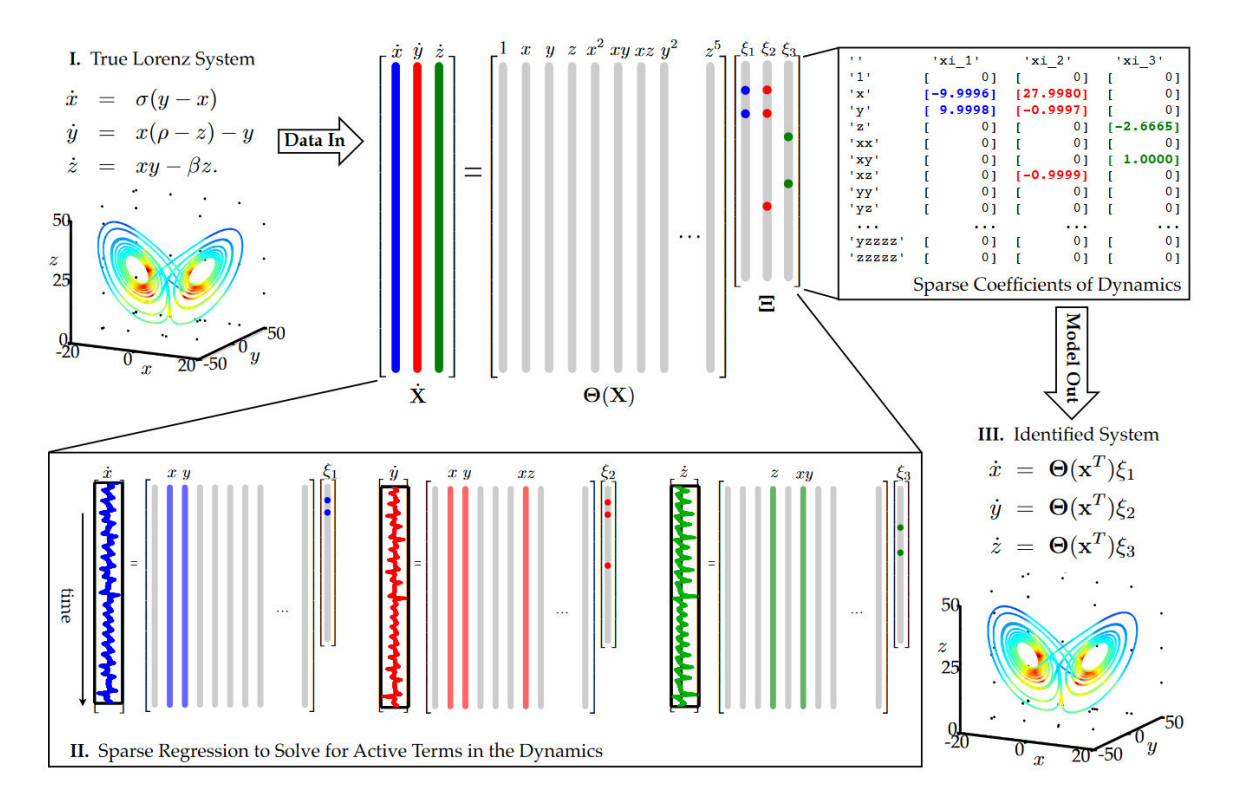


Figure 27: Visualization of the SINDy-algorithm for the Lorenz system [12]

## 4.3. Convex optimization

Convex optimization problems often occur in machine learning in form of eq. 4.24. The functions  $f_i$  and  $\mathcal{R}$  are convex and  $\lambda \geq 0$  is a fixed parameter.  $f_i$  is hereby the cost of using x on the  $i^{th}$  element of the data set.  $\mathcal{R}$  is a regularization term.[20]

$$\min_{x \in \mathbb{R}^n} \sum_{i=1}^m f_i(x) + \lambda \mathcal{R}(x) \tag{4.24}$$

By choosing  $f_i$  as demonstrated in eq. 4.25 and  $\mathcal{R} = 0$ , the original least squares problem (eq. 4.26) occurs again when M is the coefficient matrix to be optimized. [20]

$$f_i = (x^T m_i - y_i)^2 (4.25)$$

$$\min_{x \in \mathbb{R}^n} \left| |Mx - Y| \right|_2^2 \tag{4.26}$$

By adding regularization term  $\mathcal{R} = ||x||_1$  in eq. 4.27, the LASSO-problem from chapter 4.2 is set up again. [20]

$$\min_{x \in \mathbb{R}^n} ||Mx - Y||_2^2 - ||x||_1 \tag{4.27}$$

If the problem is formulated once, various algorithms were developed to solve it. A further look into the different calculation techniques is provided e.g. in [21].

# 5. Generating data sets at FLASH

Hence, the simplified and equation-based model is insufficient to achieve a mathematical accurate model of the accelerator. As pointed out in chapter 3, other approaches have to be considered. For that reason, real machine data is needed to identify the system's behavior properly.

In general, there are two different ways to achieve data from FLASH. On the one hand side, there is the data acquisition server (DAQ) which saves all machine data for two weeks. A big advantage of this method is that data from user runs can be downloaded easily without influencing the operation or even the experiments. On the other hand, it is possible to run a parameter scan directly on the accelerator during the set up of the machine. This has several advantages that will be pointed out later (chapter 5.2).

Furthermore, the influences of the current monitor states will not be investigated. They are not readjusted every time the machine is set up, so that the values only allow to show a tendency instead of e.g. the real arrival time at the BAMs which could be negative in the data.

#### 5.1. Data from DAQ and user operation

To extract data from the DAQ, it is necessary to create an .xml-file with the corresponding addresses of the control system. Now, the data can be downloaded as an .hdf5-file which contains all the data from actuators and monitors defined in the xml.-file for the desired time slot. It has to be mentioned that there is no differentiation between beam region 1 and 2 in the data. Hence, the downloaded .hdf5-file contains the complete raw data of the run. Due to the fact that every bunch train has its own ID, it is possible to follow it through the whole accelerator. Nevertheless, one has to be careful and choose the right ID-numbers for the analysis of the data set. Actuator and monitor values do not necessarily have the same shape, because the monitors save spectra for every bunch train while actuators are usually set to a certain value for a bunch. For example, spectra of the gun from the first macro bunch as well as the first entries of every macro bunch of a user run are shown in fig. 28.

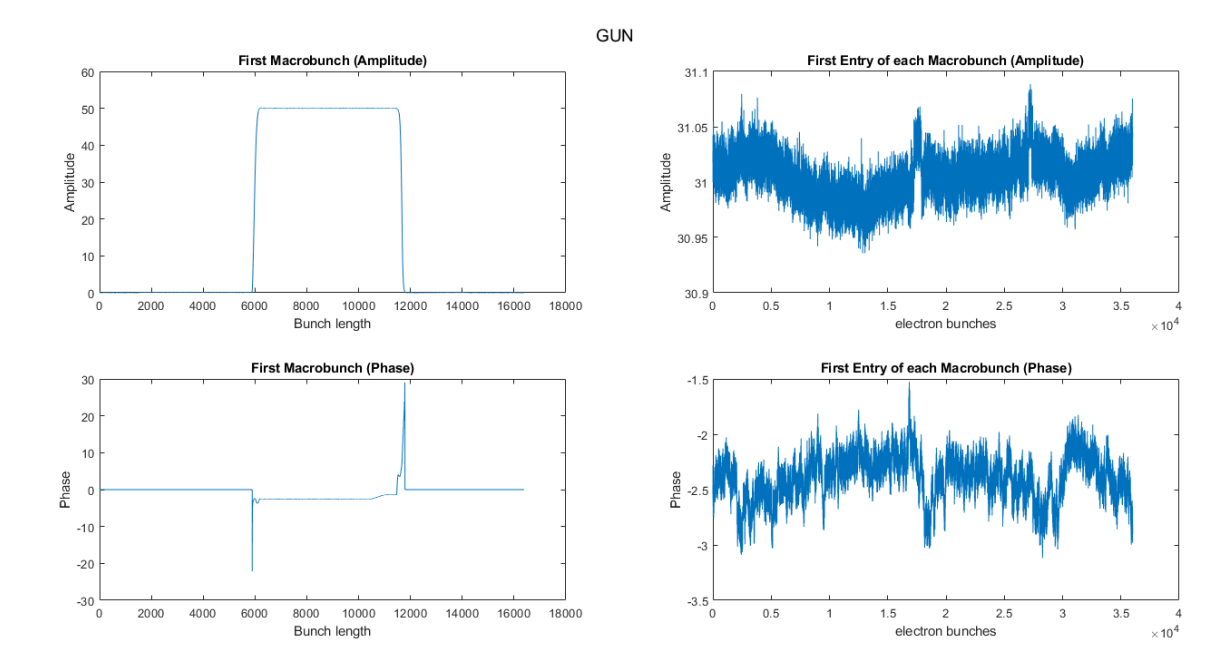


Figure 28: Gun amplitude and phase beam region 1

In fig. 28 the amplitude is the same for both beam regions, hence it is not possible to find the right position in the bunch train to define the start of the different beam regions. As described in chapter 2.4, the control system works with the first entries of the demanded beam region. For that reason, the gun phase is much more important to estimate the start and end of each beam region. Using the first non-zero entries (as the control system does) would not lead to the set value of the operator but will still be on the rising part. This can be demonstrated by comparing the values of the gun phase over a macro bunch (bottom left) where the maximum value is -22° with the first entries of each macro bunch of the data set (bottom right) where the value oscillates around -2.5°. For this reason, it might be useful to investigate the highest value for a beam region or an averaged value. But since the original control system uses the first entries, this approach will be followed for a first look into the data set. As the control system works with changes of the actuator values referring to a given set point, the first set point is given as reference.

Looking at the monitor values e.g., in fig. 29, the difficulties with data sets from user runs become visible. Apart from the fact that the current control system tends to drift over a long period of time (several hours), larger adjustments of the actuators are not needed. Single events can influence the data massively. Whether these extreme events occur randomly or whether the changes in the arrival time were intended by the operator, remains unclear. Maybe the experiment asked for slightly other beam properties or the SASE-experts enhanced the performance by adjusting the different actuators by intervention.

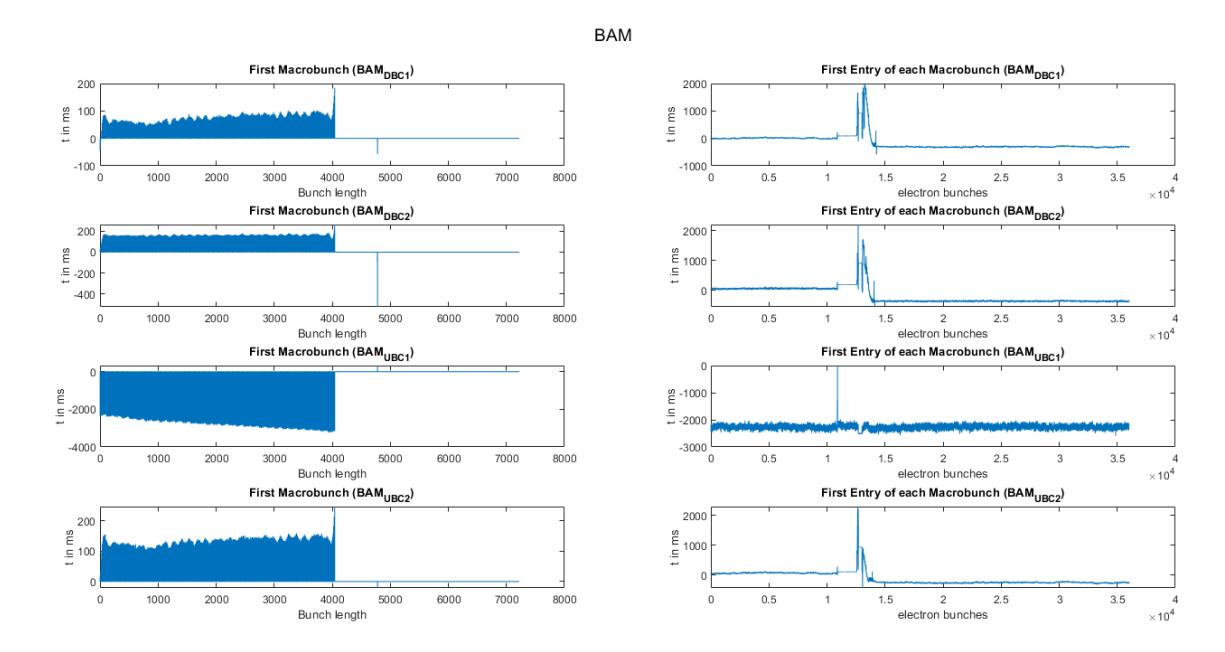


Figure 29: Example of BAM spectra and the first entries of each spectrum

In summary, it can be concluded that using data from a user run would not lead to a sufficiently accurate system identification due to the uncertainty of the information extracted from the DAQ system. Also, the changes applied by the running control system are too small to identify nonlinearities.

#### 5.2. Parameter scans

To identify nonlinearities, larger actuator changes are necessary, furthermore the machine status during the measurements should be known. For that reason, parameter scans during the set up of FLASH were performed. To collect as much data as possible at once, all actuators were scanned randomly and in parallel. Not all actuators could be used to perform the scan. For example, randomly changing the gun amplitude during the parameter scan could harm the performance of the machine for a longer time because the machine reacts very sensitively to it. Once changed, it is very difficult to readjust the gun and a longer set up time is needed. Depending on the schedule, FLASH runs with different energies, in case lower energies were needed the sumvoltage and chirp actuators of the accelerating modules 6 and 7 (ACC67 sumvoltage, ACC67 chirp) were turned off, too.

The following actuators took part in the parameter scan:

- Gun phase
- Accelerating modules 1 and 3.9 GHz sumvoltage (ACC139 SV)

- Accelerating modules 1 and 3.9 GHz chirp (ACC139 C)
- Accelerating modules 2 and 3 sumvoltage (ACC23 SV)
- Accelerating modules 2 and 3 chirp (ACC23 C)
- Accelerating modules 4 and 5 sumvoltage (ACC45 SV)

The following monitors were taken into account:

- Toroid3Gun
- BAM UBC1 (upstream of bunch compressor 1)
- BAM DBC1 (downstream of bunch compressor 1)
- BCM DBC1.1 (downstream of bunch compressor 1, coarse)
- BCM DBC1.2 (downstream of bunch compressor 1, fine)
- BAM UBC2 (upstream of bunch compressor 2)
- BAM DBC2 (downstream of bunch compressor 2)
- BCM DBC2.1 (downstream of bunch compressor 2, coarse)
- BCM DBC2.2 (downstream of bunch compressor 2, fine)
- BAM FL1.SFELC (beamline FLASH1)

To perform the parameter scan, boundaries are needed. Each actuator has a different influence on the whole system. In combination, actuators can add up, for example, by increasing the energy of the beam by increasing sumvoltage values in multiple modules at the same time. So, the maximum boundaries of the actuators in combination with each other have to be defined to avoid beam losses during the scan. Loosing the beam multiple times in a short period of time could trigger the machine protection system (MPS) which would permit operation by stopping the laser at the gun.

Hence, the boundaries were set with the operators by adjusting the actuator values step by step from the gun to ACC45 permanently checking the losses until a configuration was found that enables a wide range of scan parameters and protects the machine from beam losses. The boundaries can be found in table 1.

Actuator	value	unit
Gun phase	0.4	٥
ACC139 sumvoltage	0.2	MeV
ACC139 chirp	0.1	$\frac{1}{m}$
ACC23 sumvoltage	0.2	MeV
ACC23 chirp	0.4	$\frac{1}{m}$
ACC45 sumvoltage	0.5	MeV
ACC45 chirp	_	$\frac{1}{m}$
ACC67 sumvoltage	_	MeV
ACC67 chirp	_	$\frac{1}{m}$

Table 1: Allowed changes during the parameter scan

Again, the first entries of the beam regions are taken for all monitors. To avoid seeing influences in the data from dynamics within the monitors each set point of actuators will last for 25 laser shots at the gun, the values are averaged over each set point for system identification. An example of the absolute actuator values is shown in fig. 30 as well as an example of the absolute monitor values in fig. 31. Since the changes of the actuator values are used and not the absolute values, the changes are calculated as the difference to the first set point.

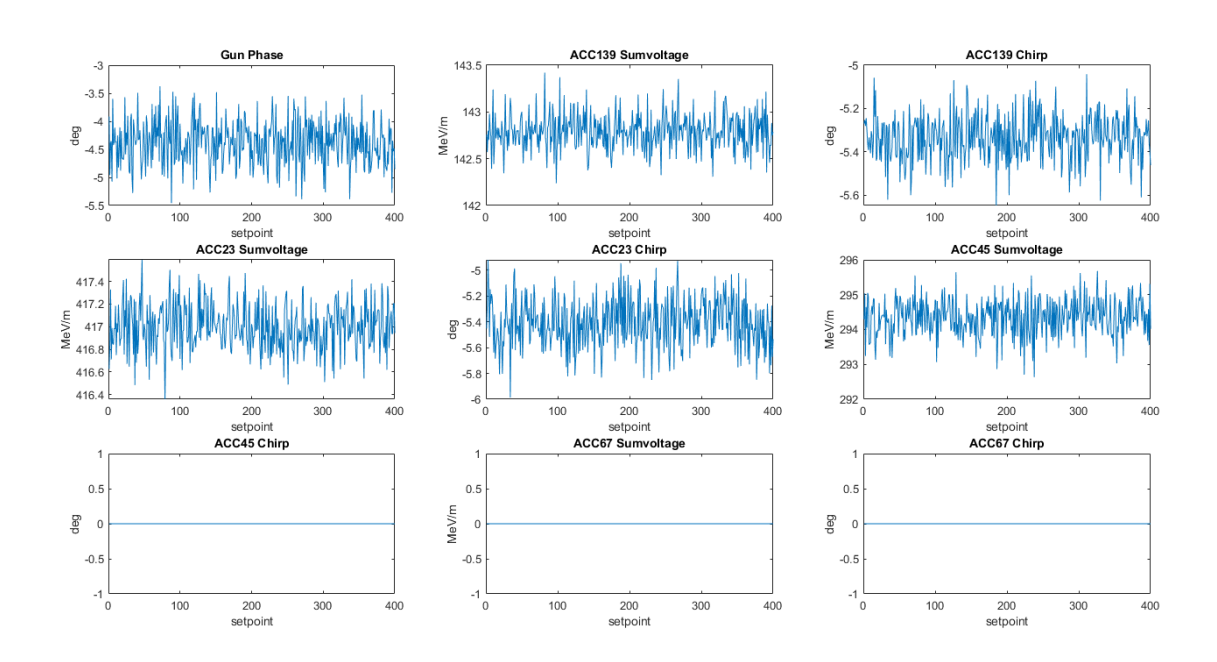


Figure 30: Actuator values of the parameter scan

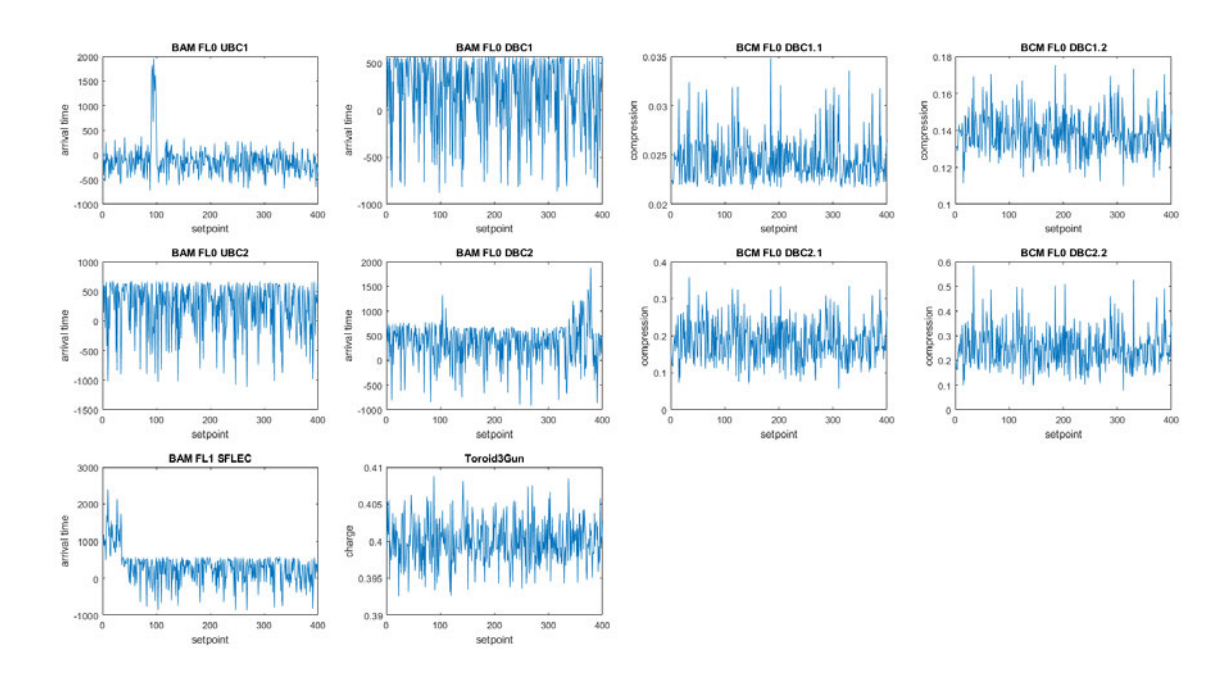


Figure 31: Monitor values of the parameter scan

# 6. Analysis of the data sets

After the data is prepared for the analysis, this chapter shall deal with the different approaches used to estimate the system precisely. Firstly, the linear response matrix will be recalculated from the data using various methods. Secondly, the given approach with a linear response matrix will be refined by using nonlinear response matrices. Furthermore, it will deal with the SINDy algorithm and its application to the data set.

For the analysis of the data set with different approaches, it is divided into a test and a training data set. The training data set contains the first 233 setpoints which refer to  $\approx \frac{2}{3}$  of the data set while the rest of the data is used for testing. The data set does not contain values for ACC67 because these modules were not turned on during the measurements due to a low energy machine configuration.

### 6.1. Recalculation of the linear response matrix

According to [18], which describes, among others, the calculation of the linear response matrix for the SwissFEL, it is possible to calculate the response matrix from data taken in a parameter scan. The response matrix can be calculated by a convex optimization using eq. 6.1 [18].

Furthermore, the size of the matrix R has changed because only the actuators participating in the parameter scan and the monitors for the accelerating section of FLASH1 are considered.

$$R = argmin_{M \in R^{m \times n}} ||\delta m - M\delta a||_F \tag{6.1}$$

Applying the concept to the FLASH training data leads to the following matrix 6.2:

$$R_{FLASH_{measured}} = \begin{bmatrix} -0.0075 & 0.0005 & 0.0014 & -0.0001 & -0.0007 & 0.0003 \\ 537.8070 & -28.5905 & -23.1756 & 2.8716 & -0.1150 & -0.7232 \\ -73.4628 & -551.6643 & -171.9084 & 38.3144 & -36.0219 & -58.3953 \\ -0.0003 & -0.0004 & -0.0147 & -0.0002 & -0.0002 & -0.0001 \\ -0.0004 & -0.0066 & -0.1010 & -0.0008 & -0.0007 & 0.0002 \\ -66.1864 & -1036.3414 & -168.6875 & 81.0404 & 2.4956 & -63.7593 \\ -55.2405 & -1620.2112 & -224.6894 & -1.7692 & 224.1198 & -87.7105 \\ 0.0009 & 0.0206 & -0.5106 & -0.0004 & -0.0671 & -0.0009 \\ 0.0013 & 0.0325 & -0.7106 & -0.0073 & -0.0971 & 0.0013 \\ -59.7441 & -1028.9428 & -252.9879 & 86.0236 & 109.8687 & -90.2930 \end{bmatrix}$$

$$(6.2)$$

The matrix  $R_{FLASH_{2024}}$  used for operation of the slow feedback system for FLASH1 looks like shown in eq. 6.3. It was reduced to the actuators and monitors participating in the parameter scan, too.

$$R_{FLASH_{2024}} = \begin{bmatrix} 0 & 0 & 0 & 0 & 0 & 0 \\ 500 & -180 & -3100 & 0 & 0 & 0 \\ 0 & -3200 & 700 & 0 & 0 & 0 \\ 0 & -0.0080 & -0.0250 & 0 & 0 & 0 \\ 0 & -0.0400 & -0.0200 & 0 & 0 & 0 \\ 0 & -3400 & 740 & 0 & 0 & 0 \\ 0 & -2500 & 600 & -430 & -45 & -100 \\ 0 & -0.0600 & -0.2000 & 0 & -0.0400 & 0 \\ 0 & 0 & -440 & 100 & 0 & 0 \end{bmatrix}$$
(6.3)

It is clearly visible that neither the values nor their sign match in a sufficient way. To show the mismatch of both matrices, the difference  $R_{diff}$  between  $R_{FLASH_{2024}}$  and  $R_{FLASH_{measured}}$  was calculated and is presented in eq. 6.4.

$$R_{diff} = \begin{bmatrix} 0.0075 & -0.0005 & -0.0014 & 0.0001 & 0.0007 & -0.0003 \\ -37.8070 & -151.4095 & -3076.8244 & -2.8716 & 0.1150 & 0.7232 \\ 73.4628 & -2648.3357 & 871.9084 & -38.3144 & 36.0219 & 58.3953 \\ 0.0003 & -0.0076 & -0.0103 & 0.0002 & 0.0002 & 0.0001 \\ 0.0004 & -0.0334 & 0.0810 & 0.0008 & 0.0007 & -0.0002 \\ 66.1864 & -2363.6586 & 908.6875 & -81.0404 & -2.4956 & 63.7593 \\ 55.2405 & -879.7888 & 824.6894 & -428.2308 & -269.1198 & -12.2895 \\ -0.0009 & -0.0806 & 0.3106 & 0.0004 & 0.0271 & 0.0009 \\ -0.0013 & -0.1625 & 0.1106 & 0.0073 & 0.0171 & -0.0013 \\ 59.7441 & 1028.9428 & -187.0121 & 13.9764 & -109.8687 & 90.2930 \end{bmatrix}$$

$$(6.4)$$

With the given matrices a calculation of the necessary actuator changes out of the measured changes of the monitors can be achieved. The values from this simulation are compared to the original changes applied during the parameter scan. For both matrices, the approach shown in eq. 6.5 from chapter 2.4 is used again.

$$\delta a = R^{-1} \cdot \delta m \tag{6.5}$$

Because R is a non-square matrix the calculation of the inverse was realized by creating the Moore-Penrose pseudo-inverse. The results for the test data set are shown in fig. 32. Applying the calculated response matrix to the test data leads to huge errors in the recalculated actuator values which should compensate the monitor changes. For example, the gun phase shows a maximum change of over  $400^{\circ}$  which is not feasible with the gun.

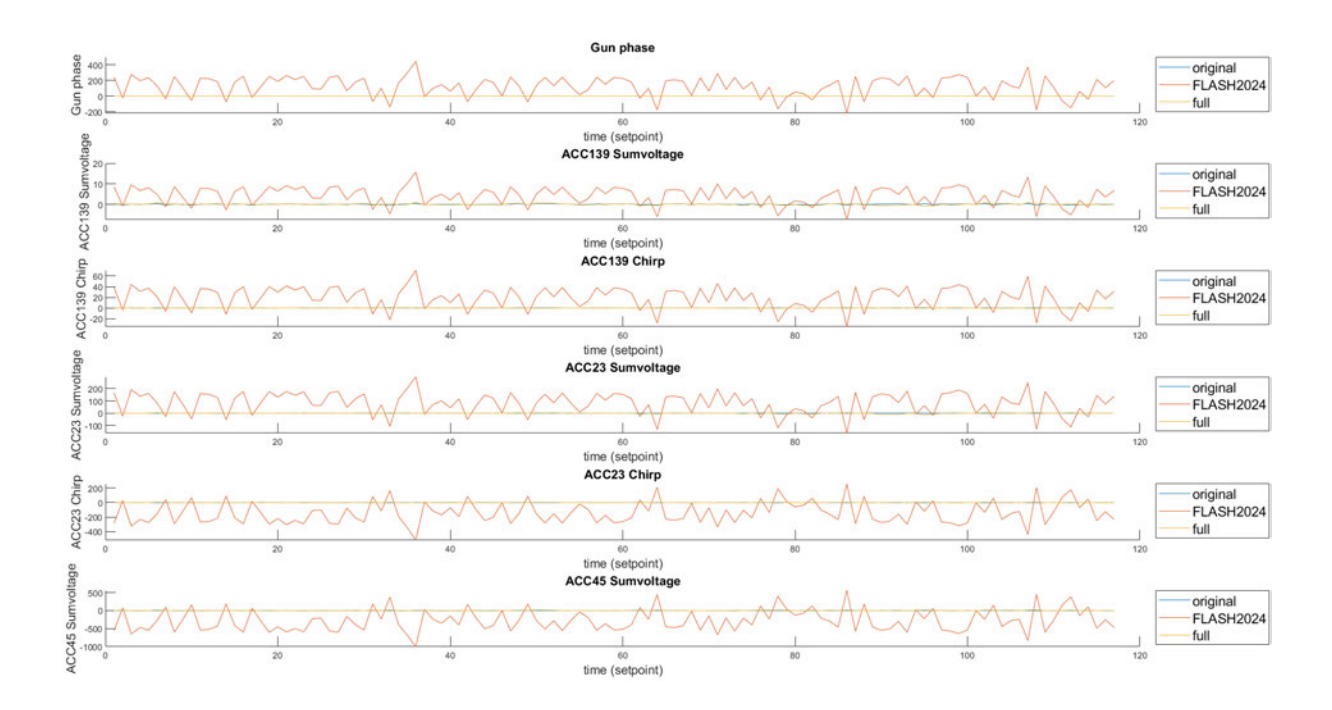


Figure 32: Comparison of original actuator changes and recalculated changes with FLASH 2024 response matrix and measured linear response matrix (test dataset)

The calculated matrix  $R_{FLASH_{measured}}$  allows non-zero entries everywhere. This might be the best linear fit for the given data but in reality there is no possibility to see influences of actuators on monitors upstream of themselves. Hence, constraints were set to the convex optimization that allow non-zero entries in the response matrix only if the monitors can be influenced by the actuators due to their location in the accelerator. Furthermore, only BAMs can measure the impact of sumvoltage actuators and BCMs can only measure the impact of chirp actuators. The resulting constraints are shown in table 2.

	Gun Ph	ACC139 SV	ACC139 C	ACC23 SV	ACC23 C	ACC45 SV
Toroid3Gun	✓					
BAM UBC1	✓	✓				
BAM DBC1	✓	✓				
BCM DBC1.1	✓		✓			
BCM DBC1.2	✓		✓			
BAM UBC2	✓	✓		✓		
BAM DBC2	✓	✓		✓		
BCM DBC2.1	✓		✓		✓	
BCM DBC2.2	✓		✓		✓	
BAM FL1SFELC	✓	✓		✓		✓

Table 2: Constraints for the combination of actuators and monitors for a reduced matrix approach

After implemention of the constraints from table 2, a multivariante regression using convex optimization is applied to the data set again. The resulting response matrix  $R_{reduced}$  (eq. 6.6) is shown below.

$$R_{reduced} = \begin{bmatrix} 0 & 0 & 0 & 0 & 0 & 0 \\ 537.4258 & -38.5409 & 0 & 0 & 0 & 0 \\ 0 & -718.4483 & 0 & 0 & 0 & 0 \\ 0 & 0 & -0.0148 & 0 & 0 & 0 \\ 0 & 0 & -0.1042 & 0 & 0 & 0 \\ 0 & -1132.9877 & 0 & 178.5237 & 0 & 0 \\ 0 & 0 & -1774.9346 & 0 & 185.3860 & 0 & 0 \\ 0 & 0 & -0.4981 & 0 & -0.0691 & 0 \\ 0 & 0 & -0.6802 & 0 & -0.1032 & 0 \\ 0 & -1101.5214 & 0 & 149.2003 & 0 & -107.1350 \end{bmatrix}$$
 (6.6)

In comparison to the original changes of the actuators (see fig. 33), this approach shows a better fit, especially for the gun phase, but still with insufficient accuracy for the other actuators.

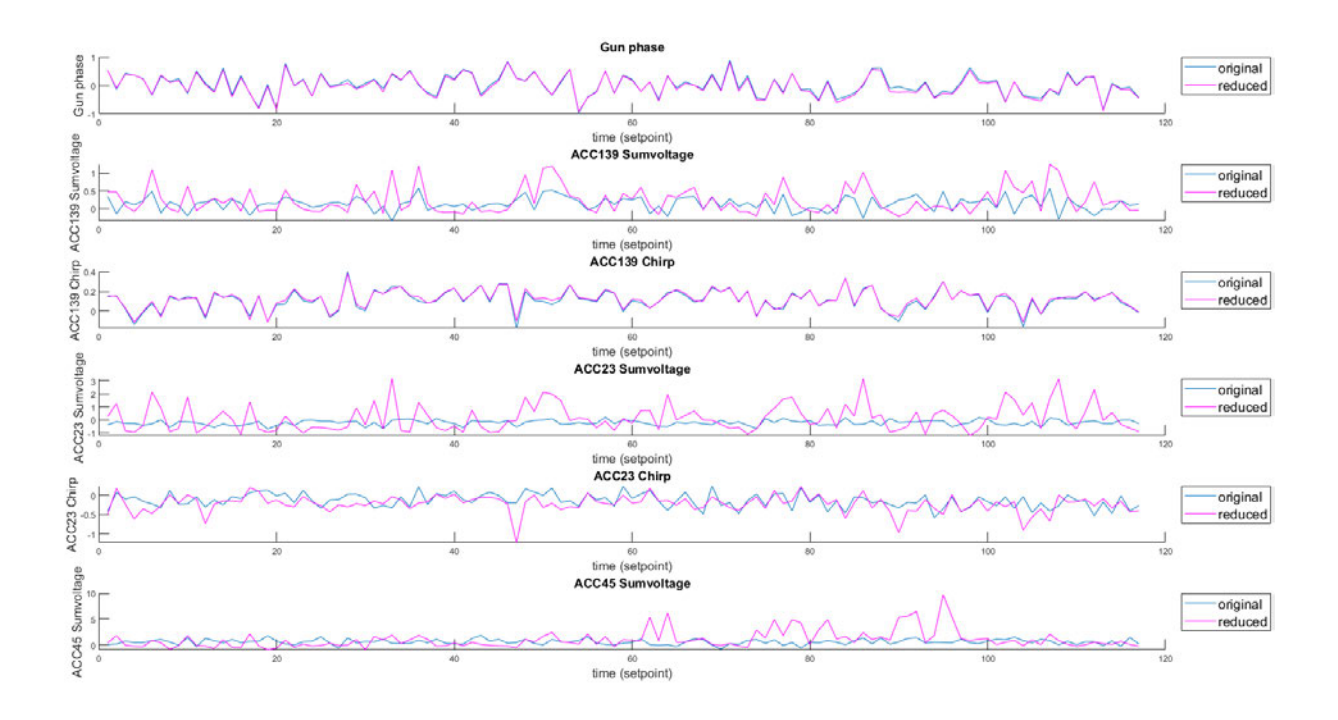


Figure 33: Comparison of original actuator changes with recalculated changes using a reduced response matrix

The current control system operates with single loops (one actuator is only influenced by one monitor). For this reason, a further simplification can be made by enabling these single loops during the calculation of the response matrix. The combination of actuators and monitors for this approach is given by often used combinations by the operators and is described in table 3.

	Gun Ph	ACC139 SV	ACC139 C	ACC23 SV	ACC23 C	ACC45 SV
Toroid3Gun						
BAM UBC1	✓					
BAM DBC1		✓				
BCM DBC1.1			✓			
BCM DBC1.2						
BAM UBC2						
BAM DBC2				✓		
BCM DBC2.1					✓	
BCM DBC2.2						
BAM FL1SFELC						✓

Table 3: Constraints for the combination of actuators and monitors for a single loop approach

This results in the following modified response matrix for single loop operation  $R_{singleloop}$ 

(eq. 6.7). The comparison of the recalculated actuator values to the original values is shown in fig. 34.

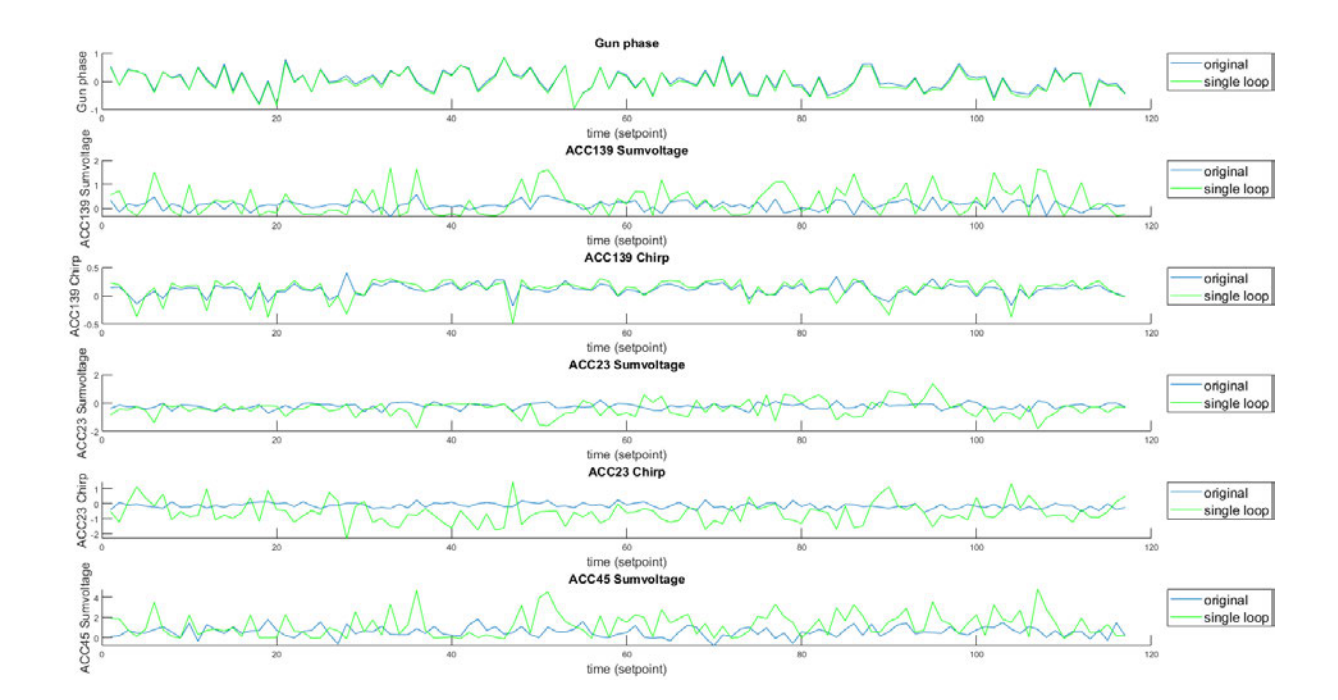


Figure 34: Comparison of original actuator changes with recalculated changes using a single loop response matrix

The error  $e_{RSME}$  is calculated using the root mean square error (RSME) for every set point i (eq. 6.8). The influence of the different matrices on the derivatives sign is shown in table 5 for the test data set. This value is important to evaluate the correct change of the actuator values because a control system operating in the wrong direction leads to increasing errors followed by a performance decrease of the machine. The approach with the

biggest total differences (full response matrix) to the original values predicts the sign the best, but the reduced matrix approach leads to the smallest overall RSME-value (table 4).

$$e_{RSME} = \sqrt{\delta a_{measured}(i)^2 - \delta a_{matrix}(i)^2}$$
 (6.8)

	Gun Ph	ACC139 SV	ACC139 C	ACC23 SV	ACC23 C	ACC45 SV	average
Full	0.2816	0.7796	0.2563	1.0508	0.5429	1.2567	0.6947
Reduced	0.2455	0.9432	0.6534	0.1585	1.0247	0.2361	0.5436
Single loop	0.1626	0.9432	0.7480	0.2153	0.9867	0.2397	0.5493

Table 4: RSME of the calculated actuator values for the test data set

	Gun Ph	ACC139 SV	ACC139 C	ACC23 SV	ACC23 C	ACC45 SV	total
Full	4	47	17	51	50	45	214
Reduced	4	69	106	68	61	66	374
Single loop	4	69	97	65	59	65	359

Table 5: False signs of the calculated actuator changes for the test data set

None of the approaches shown above leads to a sufficient and realiable control system due to significant errors during the recalculation of the actuator values. This can be caused by:

- an insufficient described system
- numerical errors during the calculation of the inverse response matrix
- non optimal data input (normalization)

The influence of nonlinearites will be shown in chapter 6.2. But the consideration of numerical errors due to the invertation of the response matrices might give a hint towards better preparation of the data and calculation techniques. To analyze the impact of numerical errors during inversion the condition numbers of all three approaches are shown in table 6.

method	condition number
$FLASH_{2024}$	$6.7026 \cdot 10^4$
full matrix	$9.1778 \cdot 10^3$
reduced matrix	$1.5562 \cdot 10^5$
single loop matrix	$5.7920 \cdot 10^4$

Table 6: Condition numbers linear

Looking at the condition numbers, it is obvious that a badly conditioned problem cannot lead to an accurate control system because tiny disturbances could have a big influence on the solution (in this case the necessary actuator change to contain a stable beam). Regarding the fact that the values of the actuators and monitors are in very different regimes, a normalization of the data could fix the high condition numbers and enhance the quality of the output of the algorithm. For this reason, a normalization of the data was performed in a way that the data contains only values within the interval [1, 2].

After normalization, the algorithms for the calculation of the full, reduced and single loop response matrices were performed again. The resulting fit can be seen in fig. 35. With the normalized data, the prediction of the necessary actuator changes improves. Especially the gun phase is still predictable with high accuracy. But the further away the actuators are located from the electron gun, the less precise the prediction becomes. Further, variations of the derivatives sign are visible so that a control system built around these linear models might lead to a counterproductive effect that amplifies the misbehavior of the beam. Nonetheless, the condition numbers have improved significantly (table 7), so that the normalized data set will be investigated with additional approaches.

method	condition number
full matrix	35.5079
reduced matrix	2.8321
single loop matrix	1.4947

Table 7: Condition numbers linear after normalization

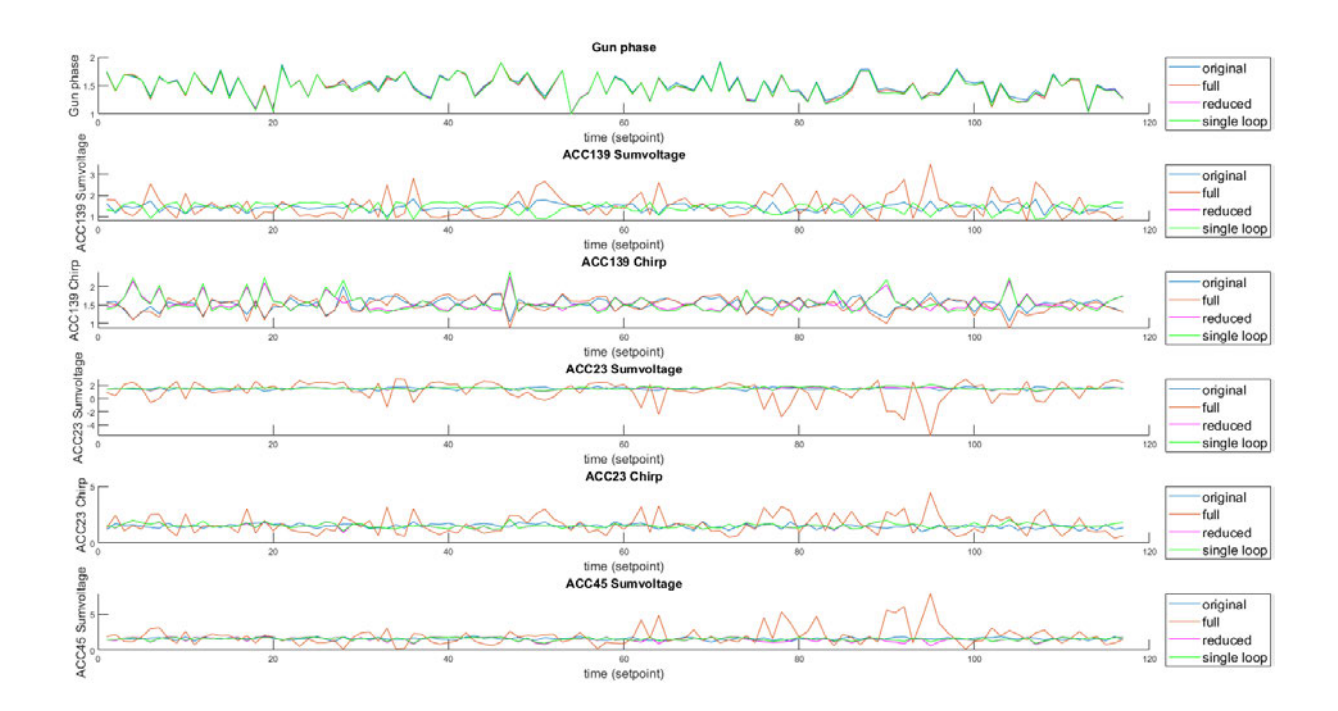


Figure 35: Comparison of original actuator changes with recalculated changes using a full, reduced and single loop response matrix after normalization of the data within the interval [1, 2] and rescaling

The error  $e_{RSME}$  is calculated after rescaling the normalized actuator changes  $\delta a_{norm}$  by applying the standard deviation S as well as the mean values  $\mu$  to  $\delta a_{rescaled}$  (eq. 6.9) and is shown in fig. 36. The influence of the different matrices on the derrivatives sign is shown in table 9. The full matrix approach with the biggest total differences (full response matrix) to the original values still achieves the best results at predicting the sign, whereas the single loop approach delivers the best RSME (table 8). In comparison to the not normalized approach, the RSME is half as big, whereas the number of false calculated signs of the derivative stays the same.

$$\delta a_{rescaled} = \delta a_{norm} \cdot S + \mu \tag{6.9}$$

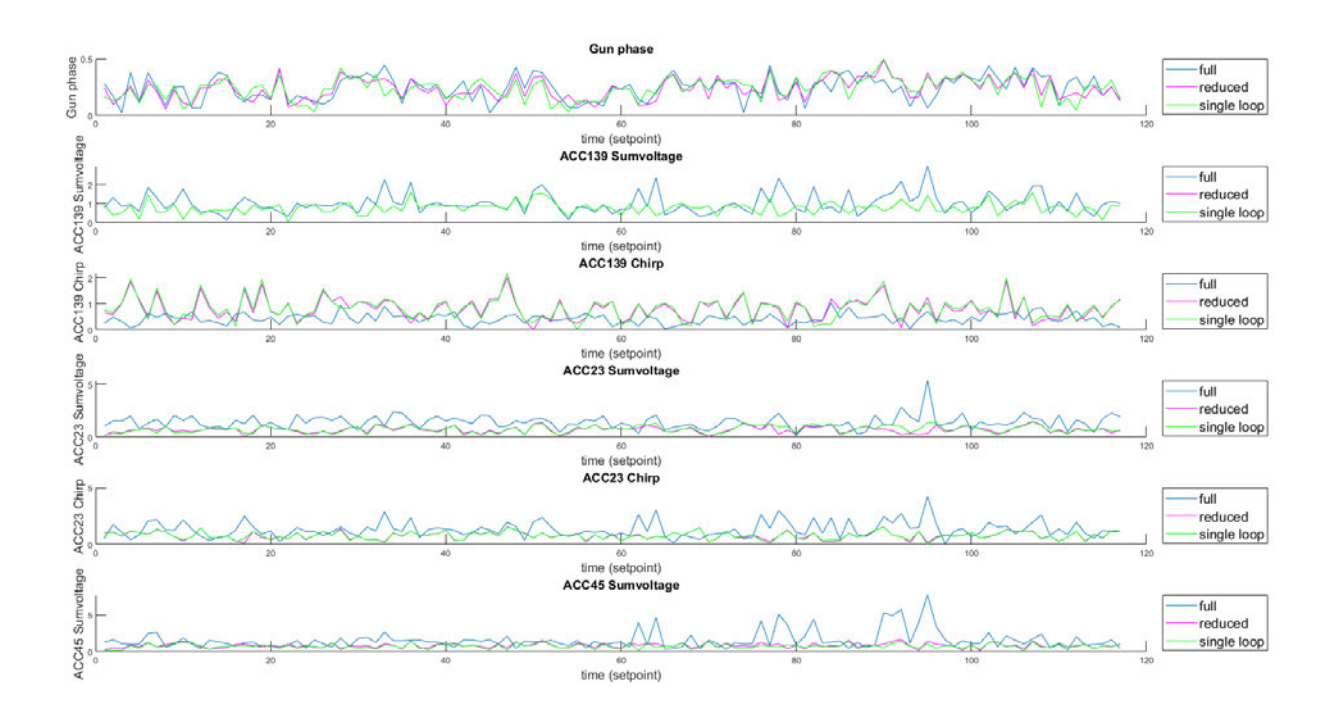


Figure 36: RSME of actuator changes after recalculation with different response matrices and after normalization of the data within the interval [1, 2] and rescaling

	Gun Ph	ACC139 SV	ACC139 C	ACC23 SV	ACC23 C	ACC45 SV	average
Full	0.2181	0.4198	0.0597	0.8892	0.2838	1.5284	0.5665
Reduced	0.1910	0.3474	0.1333	0.0923	0.4168	0.1143	0.2159
Single loop	0.1275	0.3474	0.1428	0.1223	0.4124	0.1165	0.2115

Table 8: RSME of the calculated actuator values for the normalized test data set

	Gun Ph	ACC139 SV	ACC139 C	ACC23 SV	ACC23 C	ACC45 SV	total
Full	4	47	17	51	50	45	214
Reduced	4	69	106	68	61	66	374
Single loop	4	69	97	65	59	65	359

Table 9: False signs of the calculated actuator changes for the normalized test data set

# 6.2. Nonlinear response matrix

The linear approach evaluated in the previous chapter 6.1 shows that a linearized reaction of the monitors to actuator changes does not lead to a sufficiently accurate response matrix. For that reason, the data set will be analysed for nonlinearities which could be

implemented in a nonlinear response matrix  $R(\delta a)$ .

To achieve a better understanding about how nonlinearities could affect the system and the basic equation for the current control system (eq. 6.10) is

$$\delta m = R \cdot \delta a \tag{6.10}$$

the response matrix can be calculated by eq. 6.11

$$R = \delta m \cdot \delta a^{-1} \tag{6.11}$$

Assuming that the monitor values are sufficiently accurate and their measurement principle is not affected by the changes in value of single actuators, R might be dependend on a nonlinear behavior of the actuators. Doubling the  $\delta a$  might not lead to a doubled  $\delta m$ , instead, the changes of the monitors might be slightly larger or smaller. This leads to eq. 6.12 with a dependent response matrix  $R(\delta a)$ .

$$R = R(\delta a) \tag{6.12}$$

To evaluate whether there is a dependency between the height of the changes of the actuators and the corresponding monitor answer, the derivative  $\frac{\delta m}{\delta a}$  was calculated for every taken data point with the normalized data set from chapter 6.1 and visualized in fig. 60. A similar looking plot of the non-normalized data is attached in appendix B. In contrast to the assumption of linear behavior of the accelerator, the scatter plots definitely show nonlinear dependencies. Especially the BAMs downstream of the accelerating modules 1 and 39 shows strong nonlinear behaviors in combination with this actuator. Furthermore, it can be estimated that BAMs and sumvoltage actuators show the greatest codependency; so do BCMs and chirp values. The gun phase, as the first part of the system, is influencing BAMs in the same amount as the BCMs.

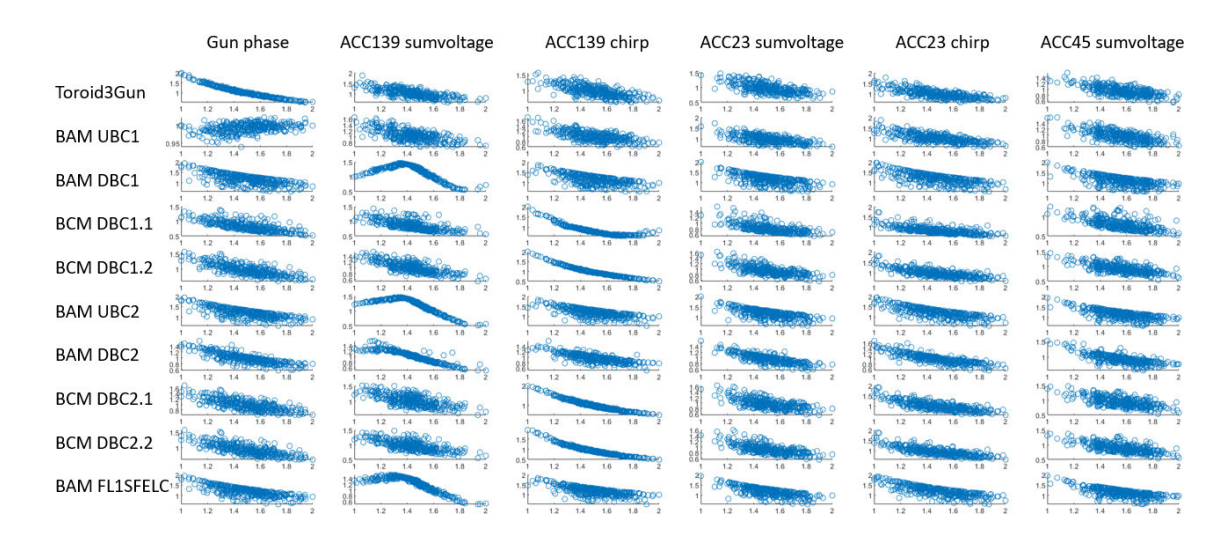


Figure 37: nonlinear dependencies between changes of actuators and monitors

The implementation of the nonlinear behavior into the response matrix approach will be achieved by fitting polynomials of different order to the measured values and the derived entries for every measurement point. Hence, every machine set point has its own specific response matrix according to the actuator settings. Afterwards, the response matrices will be inverted by SVD to realize a recalculation of actuator changes out of the measured monitor changes during the operation of the FLASH accelerator.

For the fit of the different monitor-actuator combinations, polynomials of orders up to four were used. This results in a fit calculated via least squares for all actuators with all monitors e.g., the gun phase (fig. 65). The fit for the other actuators can be found in appendix C. Table 10 shows the order of the chosen polynomials as well as the RSME of the fit.



Figure 38: Fitted data for gun phase with polynomials of order 2

Actuator	polynomial (order)	RSME	RSME linear
Gun phase	2	0.1101	0.1143
ACC139 sumvoltage	4	0.0947	0.1253
ACC139 chirp	2	0.0971	0.1143
ACC23 sumvoltage	2	0.1336	0.1358
ACC23 chirp	2	0.1355	0.1429
ACC45 sumvoltage	2	0.1288	0.1314
ACC45 chirp	_	_	_
ACC67 sumvoltage	_	_	_
ACC67 chirp	_	_	_

Table 10: Parameters contained in the data set, polynomials used and RSME of the fit compared to a linear fit

With a better fit, the recalculation of the monitor values according to the actuator settings is possible. To achieve a matrix that is filled with the corresponding entries of the polynomial fit, it is necessary to refill the matrix every time. The calculation of the first column with the known coefficients of the fit coeff1, the actuator values actuators and the given monitor values monitors is shown within the algorithm 3. With the polynomials of different orders according to table 10, all entries for the nonlinear response matrix for a specific working point can be estimated.

#### **Algorithm 3** calculation of $R_{nonlinear}$ -entries for gun phase

```
1: \operatorname{\mathbf{procedure}}\ (actuators_{live}, monitors, coeff1)
2: \operatorname{\mathbf{for}}\ h = 1 : height(monitors)\ \operatorname{\mathbf{do}}
3: 
4: Fit_{GunPhase}(h) \leftarrow coeff1(h,1) \cdot actuators_{live}(1)^2 + coeff1(h,2) \cdot actuators_{live}(1) + coeff1(h,3)
5: 
6: \operatorname{\mathbf{end}}\ \operatorname{\mathbf{for}}
7: R_{nonlinear}(:,1) = Fit_{GunPhase}
8: \operatorname{\mathbf{end}}\ \operatorname{\mathbf{procedure}}
```

Being able to create nonlinear response matrices allows to test the accuracy of the calculation. Therefore, the actuator values are recalculated with the help of the Moore-Penrose pseudo-inverse as explained in chapter 2.4. The recalculated values now can be compared to the real actuator values for every set point of the machine. A graphical comparison is presented in fig. 39.

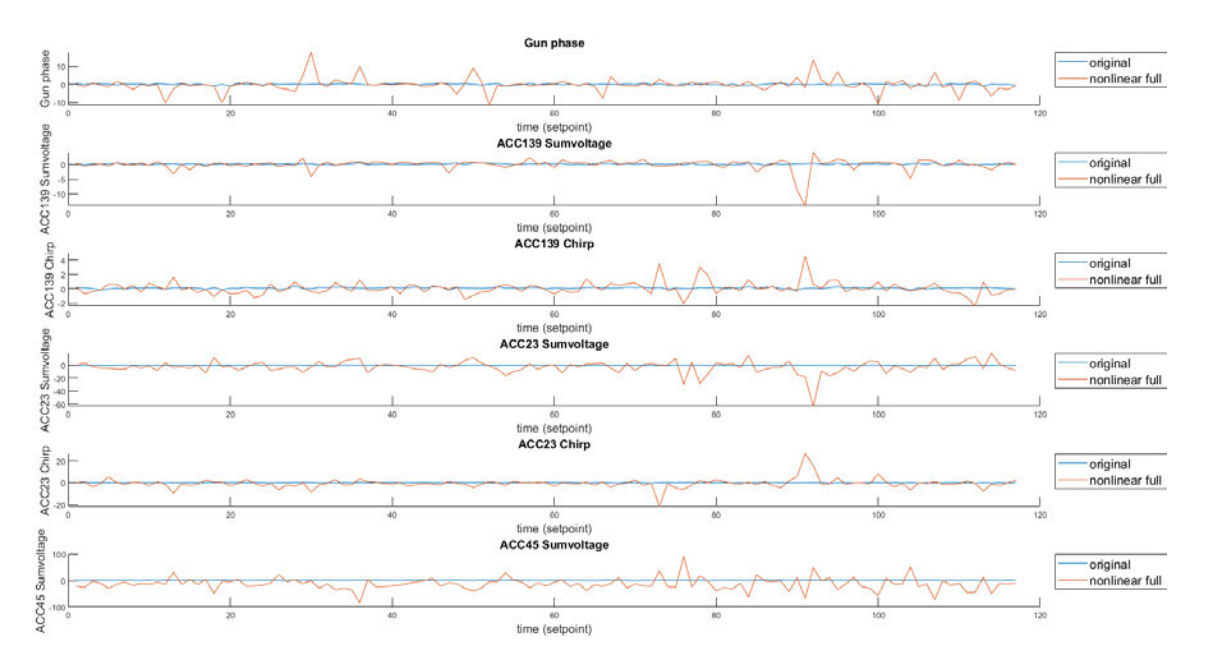


Figure 39: Comparison measured values and estimated values from the nonlinear full matrix approach

Although the polynomial fit seems to be more accurate, the calculation of new actuator values is not possible with the current matrices. To understand why this uncertainty in the result occurs, one has to take a closer look into the matrices themselves, again. As example, a random picked matrix  $R_{nonlinear,full}$  is picked from the calculation (eq. 6.13).

The condition number can be found in table 11 and is even larger than for the linear case. This shows that building the inverse is a serious problem for the nonlinear approach with a fully filled nonlinear matrix.

$$R_{nonlinear,full} = \begin{bmatrix} 1.3385 & 1.0367 & 1.1240 & 0.9929 & 1.0928 & 1.0089 \\ 0.9903 & 1.0415 & 1.1604 & 1.0182 & 1.1286 & 1.0364 \\ 1.3820 & 1.3605 & 1.3348 & 1.1740 & 1.3074 & 1.1904 \\ 0.9908 & 0.8601 & 1.0913 & 0.8286 & 0.9141 & 0.8517 \\ 1.1524 & 1.0056 & 1.2667 & 0.9700 & 1.0656 & 0.9873 \\ 1.4058 & 1.3518 & 1.3547 & 1.1922 & 1.3278 & 1.2065 \\ 1.1581 & 1.0516 & 1.1075 & 0.9800 & 1.0856 & 0.9858 \\ 1.1631 & 1.0200 & 1.3037 & 0.9828 & 1.1021 & 1.0057 \\ 1.0995 & 0.9652 & 1.2249 & 0.9305 & 1.0402 & 0.9501 \\ 1.4102 & 1.3401 & 1.3550 & 1.1963 & 1.3284 & 1.2047 \end{bmatrix}$$
 (6.13)

Following the path from chapter 6.1, the matrices will be optimized in a way like the linear matrix for a reduced (table 2) and a single loop approach (table 3). The condition numbers as well as a comparison to the values from the linear approaches can be found in table 11. In addition to this, the matrices of the reduced ( $R_{nonlinear,reduced}$ ) and single loop ( $R_{nonlinear,singleloop}$ ) approaches belonging to the random chosen set point are shown in eq. 6.14 and eq. 6.15. The recalculation of the actuator changes for all approaches can be found in fig. 40.

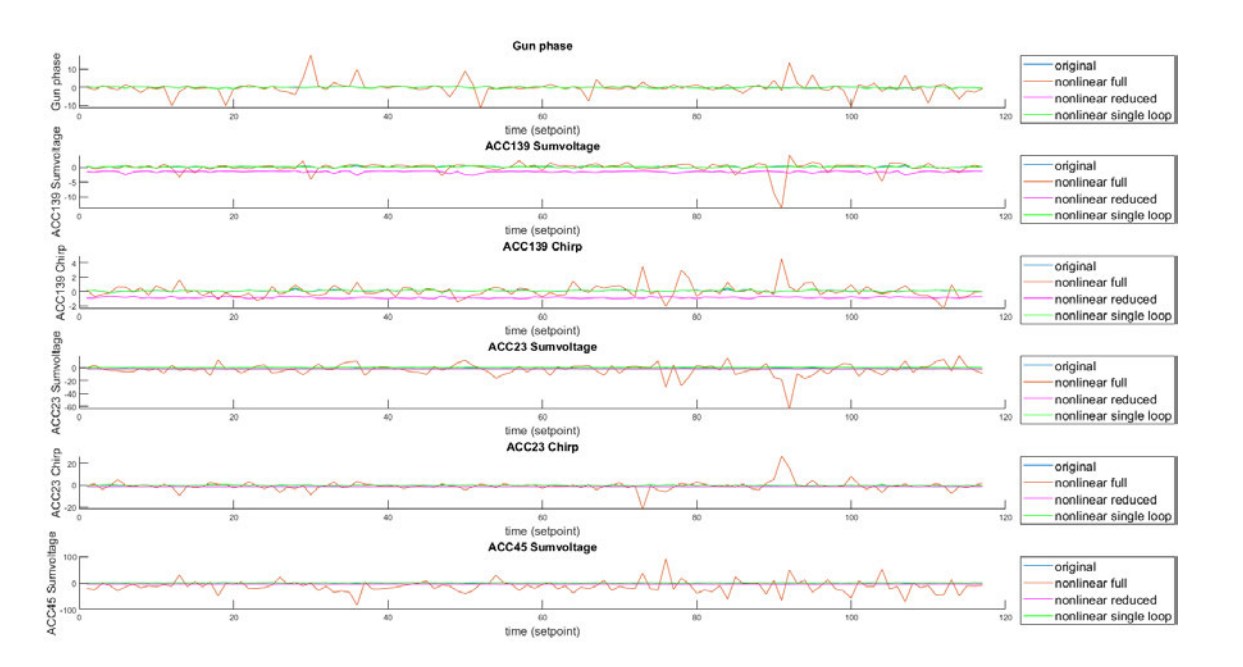


Figure 40: Comparison gun phase, measured values and estimated values from full, reduced and single loop approach

method	condition number linear	condition number nonlinear
full matrix	35.5076	1095.3483
reduced matrix	2.8321	6.4345
single loop matrix	1.4947	1.5655

Table 11: Condition numbers non linear after normalization

The RSME for the nonlinear approaches were calculated and are shown in table 12 as well as the amount of values derivatives with false signs (table 13). The data shows that there

is no significant improvement of the prediction with the new approach, although a slighly better system identification took place. Especially the reduced and single loop matrices allow precise predictions with the given monitor changes. For this reason, a closer look on the combinations of monitors used for the prediction of the actuator values will be taken as per below.

	Gun Ph	ACC139 SV	ACC139 C	ACC23 SV	ACC23 C	ACC45 SV	average
Full	0.5377	0.2602	0.2055	0.4868	0.0706	20.9878	3.7581
Reduced	0.1578	1.5353	0.8725	2.0607	1.3683	4.1859	1.6967
Single loop	0.1530	0.0801	0.0568	0.3793	0.2256	0.2815	0.1960

Table 12: RSME of the calculated actuator values

	Gun Ph	ACC139 SV	ACC139 C	ACC23 SV	ACC23 C	ACC45 SV	total
Full	43	50	41	42	66	50	292
Reduced	4	66	102	61	75	61	369
Single loop	4	10	16	27	20	32	109

Table 13: False signs of the calculated actuator values

The gun phase can already be predicted with high accuracy. Looking at the enabled monitors which take part in the calculation of the needed actuator values the BAM UBC1 is the dominant monitor. The single loop approach is the best fit for the gun phase as presented in table 12. Nevertheless, adding the BCMs and BAMs to the fit is investigated, too. A comparison of the gun phase recalculated with this nonlinear approach to the original values is shown in fig. 41. A comparison of the errors and signs can be found in table 14.



Figure 41: Fitted data for gun phase with polynomials of order 2 compared to the original values

Since the gun phase seems to gather the dominant terms, they were neglected for the fit of the ACC139 parameters the results can be found in fig. 42. The fit improved clearly, the RSME and the false predicted signs of the derivatives can be found in table 14.

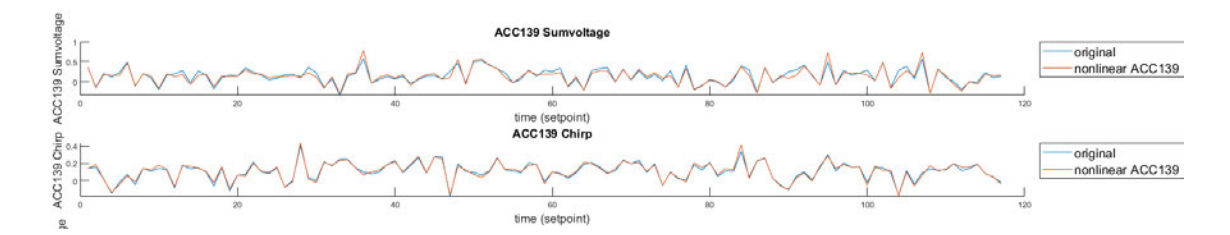


Figure 42: Fitted data for ACC139 sumvoltage and chirp with polynomials of order 4 and 2 compared to the original values

Following the scheme for the accelerating modules 2 and 3 the values of the gun and the modules 1 and 3.9 GHz were neglected and the results presented in fig. 43 and table 14.

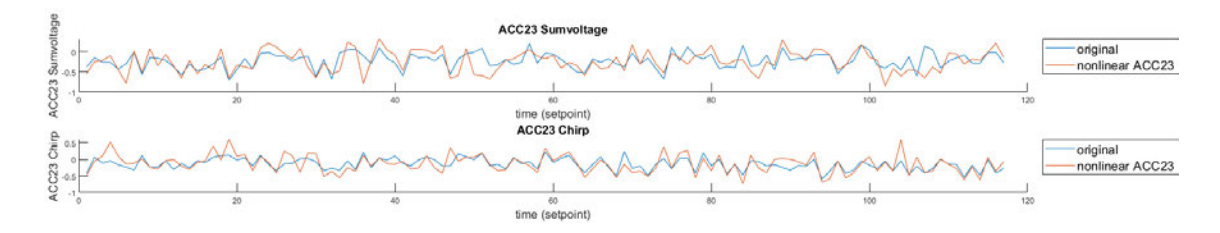


Figure 43: Fitted data for ACC23 sumvoltage and chirp with polynomials of order 2 compared to the original values

Again, all actuators upstream of ACC45 were neglected but for this actuator the fit improved again when the upstream BCMs were considered, too. The results are shown in fig. 44 and table 14.

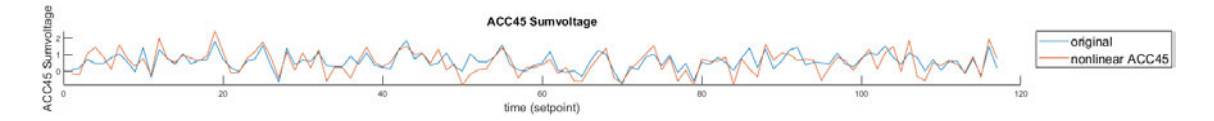


Figure 44: Fitted data for ACC45 sumvoltage and chirp with polynomials of order 2 compared to the original values

	Gun Ph	ACC139 SV	ACC139 C	ACC23 SV	ACC23 C	ACC45 SV	avg./total
RMSE	0.1459	0.0790	0.0467	0.3987	0.2324	0.1238	0.1711
false signs	9	24	19	89	74	89	304

Table 14: RSME and false prediced signs of the actuator changes of the calculated actuator values

# 6.3. Sparse Identification of Nonlinear Dynamics

From chapter 4.2, the introduced SINDy algorithm for the identification of the governing equations of nonlinear dynamic system is applied to the measured data set to evaluate

the influence of dynamics. Furthermore, a version of the SINDy algorithm with control terms will be presented which results in a sequential least squares regression of the data with the included coupling of the actuators.

#### 6.3.1. SINDy

To evaluate whether there is a certain dynamic in the system, it will be applied to the data set taken from FLASH1. As Maximum polynomial order, two was chosen and  $\lambda$  was set to 0.5. The results show that no coincidence between time dependent derivatives of the monitor values and the monitor values can be found since nearly every third sign is constantly predicted incorrectly over all monitors as shown in fig. 45 and table 15. This result was expected because the monitor values were averaged in the data preparation.

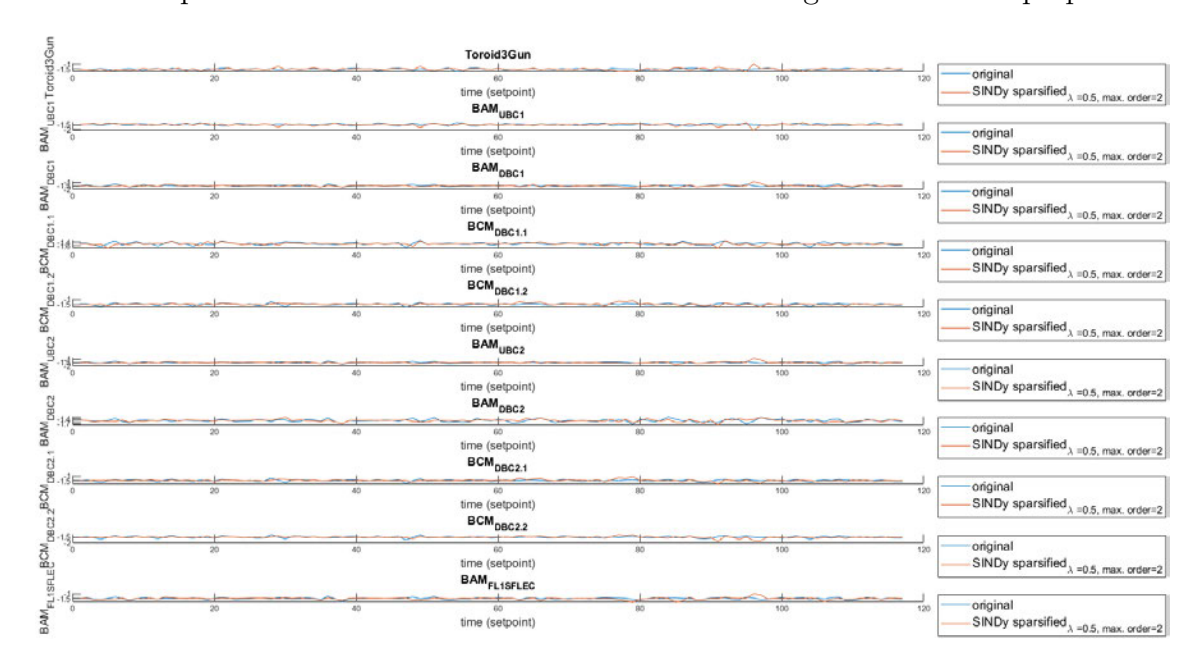


Figure 45: Derivatives of  $\delta m$  calculated with SINDy with  $\lambda=0.5$  and maximum polynomial order of 2

	Toroid3Gun	$BAM_{UBC1}$	$BAM_{DBC1}$	$BCM_{DBC1.1}$	$BCM_{DBC1.2}$	$BAM_{UBC2}$	$BAM_{DBC2}$	$BCM_{DBC2.1}$	$BCM_{DBC2.2}$	$BAM_{FL1SFELC}$
RMSE	0.2608	0.2330	0.2331	0.2961	0.3176	0.3181	0.2819	0.1335	0.1444	0.2012
false signs	40	42	51	52	43	53	45	48	47	47

Table 15: RSME of the calculated monitor values and false signs of the monitor changes during test with 117 setpoints using the SINDy algorithm and the normalized data set

#### 6.3.2. SINDy with control

For a controlled system there is an extension of the library matrix possible by including the actuators [22]. The resulting system of equations is shown in eq. 6.16.

$$\delta \dot{m} = \Theta(\delta m, \delta a) \Xi \tag{6.16}$$

Solving the equations leads to the results shown in fig. 46 and table 16. They do not show improvements of the RMSE compared to the classical SINDy approach but instead the amount of falsely predicted signs increases.

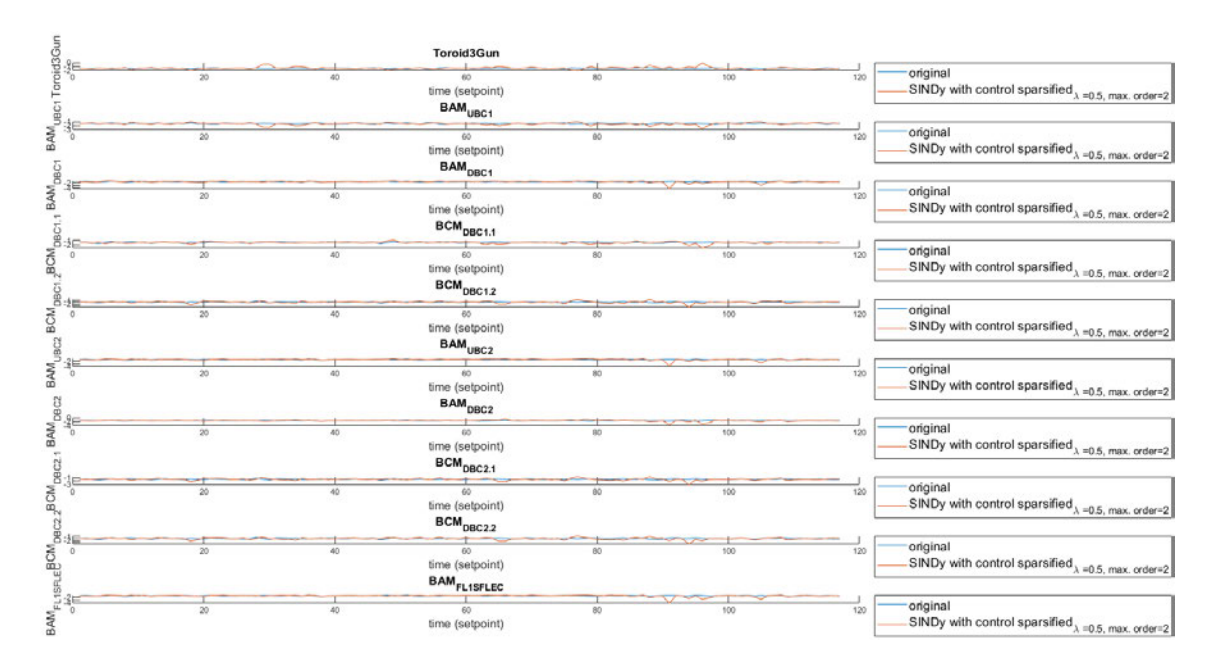


Figure 46: Derivatives of  $\delta m$  calculated with SINDy with control terms with  $\lambda=0.5$  and maximum polynomial order of 2

	Toroid3Gun	$BAM_{UBC1}$	$BAM_{DBC1}$	$BCM_{DBC1.1}$	$BCM_{DBC1.2}$	$BAM_{UBC2}$	$BAM_{DBC2}$	$BCM_{DBC2.1}$	$BCM_{DBC2.2}$	$BAM_{FL1SFELC}$
RMSE	0.1890	0.2341	0.3779	0.1483	0.4443	0.3348	0.1540	0.4794	0.4377	0.3259
false signs	45	42	59	51	49	56	50	58	54	55

Table 16: RSME of the calculated monitor values during test with 117 setpoints (normalized data)

As both approaches are not suitable for a sufficiently accurate system identification, they are not followed further in subsequent investigations.

#### 6.4. SINDy modified

To achieve a better prediction of actuator values, the SINDy algorithm is modified in a way that the time dependent derivatives will be replaced by the values to be predicted. For that reason, a direct and indirect approach for the recalculation of the actuator values will be presented as well as further modifications to the algorithm.

#### 6.4.1. Indirect calculation of the actuator values using a modified SINDy algorithm

In case of adapting the approach with the inversion of a response matrix from chapter 2.4, the monitor values must be calculated as shown in eq. 6.17.

$$\delta m = \Theta(\delta a)\Xi \tag{6.17}$$

An estimation of combinations of polynomials up to order two build the governing equations for the system, a sequential least squares regression is performed with a value of  $\lambda = 0.5$ . The plots for the sparsity matrix  $\Xi$  as well as explanations to the various matrix entries can be found in fig. 47. The plot shows that the modified SINDy algorithm has found similar dependencies like the reduced linear approach but also implements several nonlinear terms.

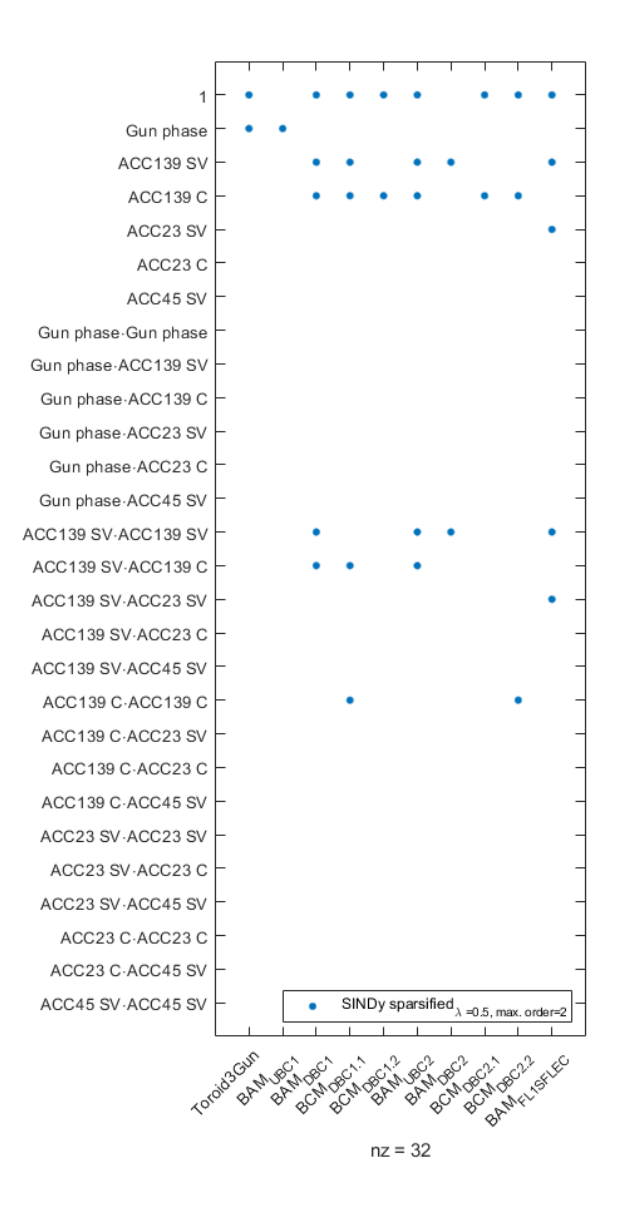


Figure 47: Sparsity matrix visualization with  $\lambda=0.5$  and maximum polynomial order of 2

With the now given sparsity matrix  $\Xi$  a new nonlinear response matrix is set up with the governing equations from the modified SINDy algorithm. Hence,  $\Theta$  contains all variations of the polynomials up to the chosen order as well as the actuator values themselves, it is possible to extract the actuator values from a recalculated  $\Theta$ , as shown in eq. 6.18.

$$\Theta(\delta a) = \delta m \cdot \Xi^{-1} \tag{6.18}$$

The prediction of the monitor values does not work perfectly although the RMSE as well as the deviation in sign seem to be accurate enough to recalculate actuator values, as shown in table 18 and table 19. A visualization of the recalculated monitor values can be found in fig. 48

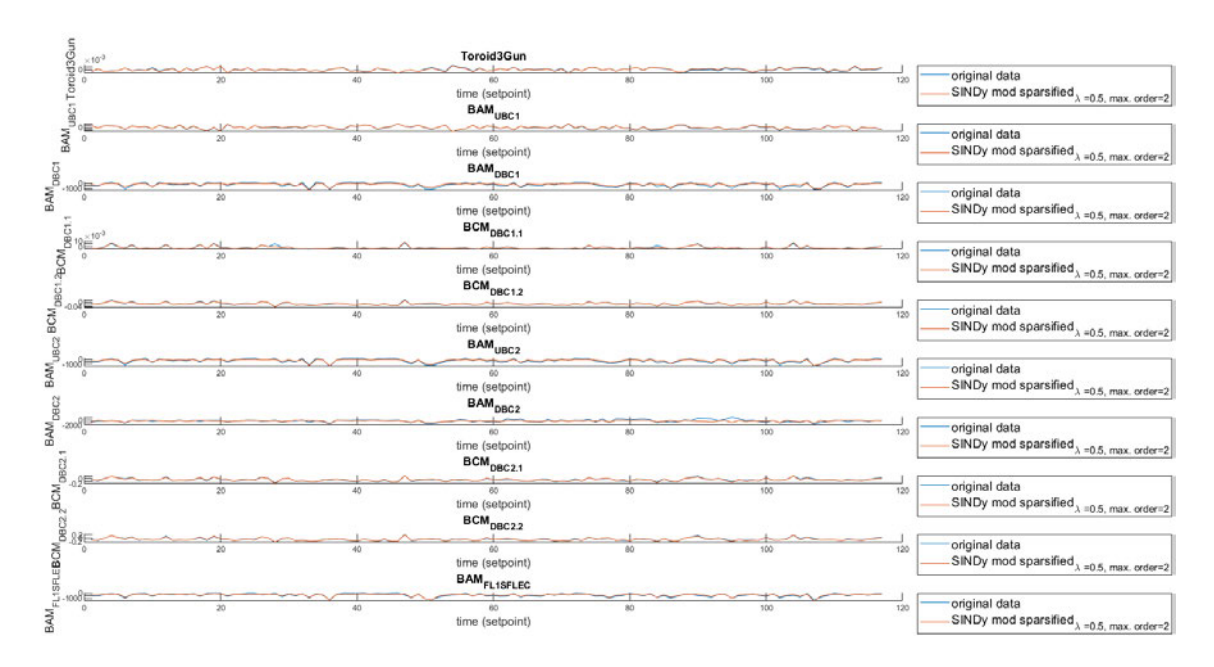


Figure 48: Visualization of the recalculated monitor changes with  $\lambda = 0.5$  and maximum polynomial order of 2 using a modified version of the SINDy algorithm

As already pointed out for the response matrices in the previous chapters, the sparsity of the matrix  $\Xi$  leads to numerical problems during the inversion. The condition number of  $\Xi$  is  $3.4274 \cdot 10^{18}$ , so that the recalculation of the actuator values from  $\Theta$  cannot work with high accuracy. This can be shown by plotting the recalculated values for the actuators for the test data set (fig. 49) and by looking at the RMSE and the derivatives sign (table 17).

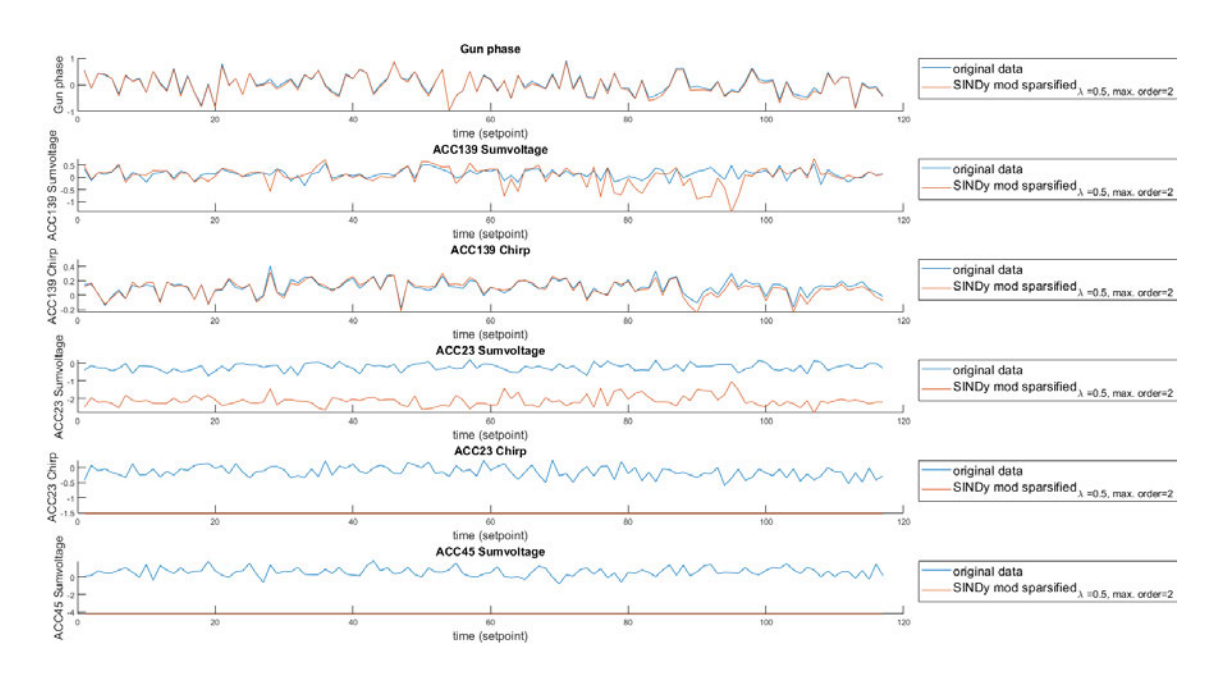


Figure 49: Recalculated actuator changes from the modified SINDy approach (test data set)

	Gun Ph	ACC139 SV	ACC139 C	ACC23 SV	ACC23 C	ACC45 SV	avg./total
RMSE	0.1487	0.3018	0.0937	2.4615	1.4530	4.2352	1.4490
false signs	3	22	6	67	99	86	283

Table 17: RSME and false predicted signs of the derivatives of the recalculated actuator values from the test data set using the indirect approach

	Toroid3Gun	$BAM_{UBC1}$	$BAM_{DBC1}$	$BCM_{DBC1.1}$	$BCM_{DBC1.2}$	$BAM_{UBC2}$	$BAM_{DBC2}$	$BCM_{DBC2.1}$	$BCM_{DBC2.2}$	$BAM_{FL1SFELC}$
RMSE	0.0003	33.3614	213.2382	0.0007	0.0034	136.3491	266.8926	0.0291	0.0392	96.2755
false signs	10	6	17	11	6	11	31	10	10	12

Table 18: RSME and false predicted sign of the derivatives of the calculated monitor values during training using the indirect approach

	Toroid3Gun	$BAM_{UBC1}$	$BAM_{DBC1}$	$BCM_{DBC1.1}$	$BCM_{DBC1.2}$	$BAM_{UBC2}$	$BAM_{DBC2}$	$BCM_{DBC2.1}$	$BCM_{DBC2.2}$	$BAM_{FL1SFELC}$
RMSE	0.0011	65.7849	346.6004	0.0011	0.0075	421.0094	293.082	0.049	0.0717	375.1127
false signs	1	4	10	8	10	4	22	9	8	8

Table 19: RSME and false predicted signs of the derivatives of the calculated monitor values during testing using the indirect approach

## 6.4.2. Direct calculation of the actuator values using the modified SINDy algorithm

Another possibility to receive the actuator values from the measured monitor values is a direct approach using the changes of the monitors with different polynomials, it is shown in eq. 6.19. Due to the changed input parameters, the sparsity matrix changes, too.

$$\delta a = \Theta(\delta m) \Xi \tag{6.19}$$

Because this approach shows the combination of monitors affecting the actuator values, the sparsity matrix looks different as shown in fig. 50. The chosen parameters for the modified SINDy algorithm stay the same at first ( $\lambda=0.5$ , max. polynomial order 2). A closer look at the sparsity matrix  $\Xi$  raises the idea that much more terms have to be taken into account for the calculation than for the approach based on the current control system using the inversion of  $\Xi$ .

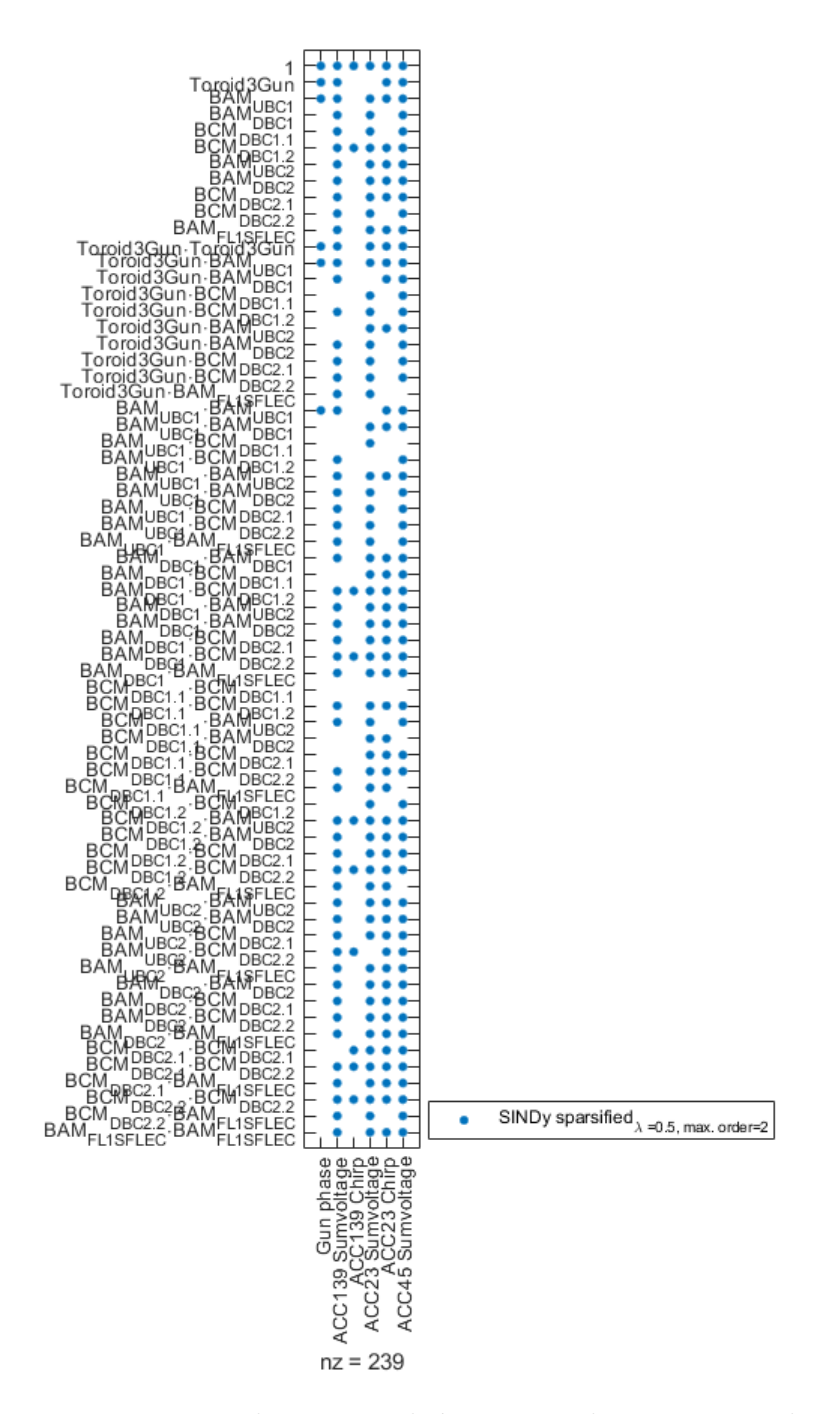


Figure 50: Sparsity matrix visualization with  $\lambda=0.5$  and maximum polynomial order of 2 of the direct approach

Nevertheless, the actuator values are recalculated and a plot for the test data set is shown in fig. 51. At first glance, the behavior seems to fit the actuator values quite well. A closer look at the RMSE and the amount of wrong predicted signs of the derivatives for training (table 20) and test (table 21) shows a better accuracy than the nonlinear approaches.

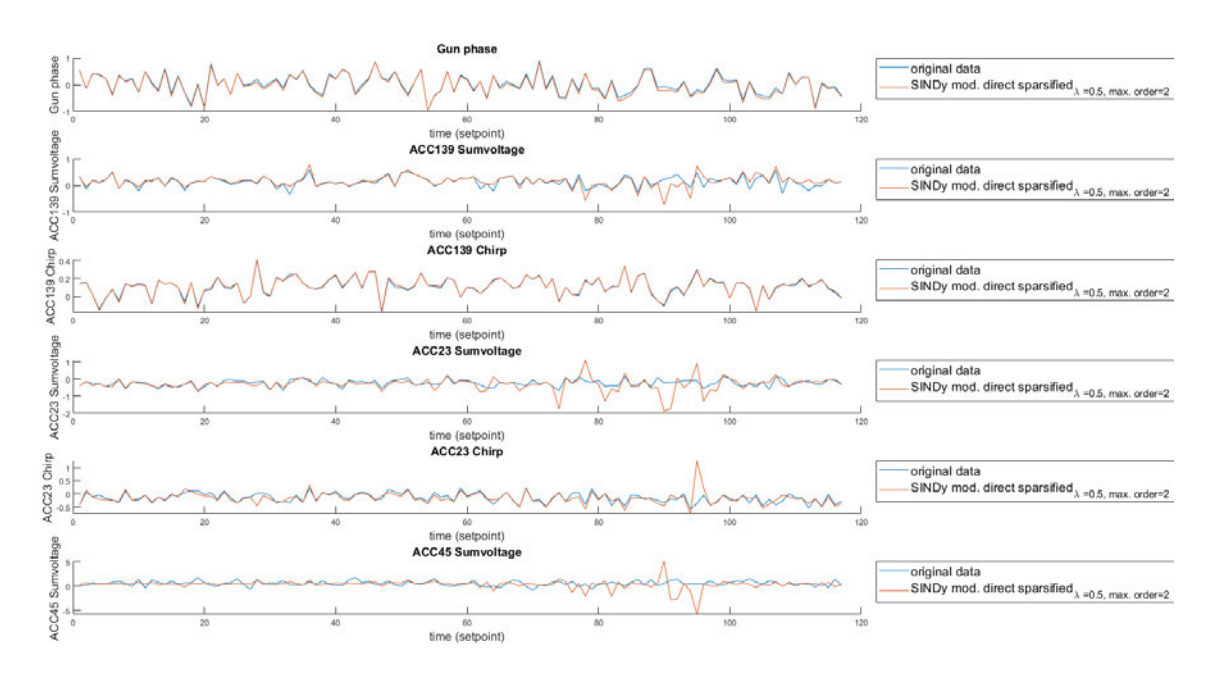


Figure 51: Sparsity matrix visualization with  $\lambda = 0.5$  and maximum polynomial order of 2 using the direct approach

	Gun Ph	ACC139 SV	ACC139 C	ACC23 SV	ACC23 C	ACC45 SV	avg./total
RMSE	0.0785	0.0585	0.0305	0.3295	0.1467	0.2791	0.1538
false signs	5	10	4	26	18	83	146

Table 20: RSME and false predicted signs of the derivatives of the recalculated actuator values from the training data set using the direct approach

	Gun Ph	ACC139 SV	ACC139 C	ACC23 SV	ACC23 C	ACC45 SV	avg./total
RMSE	0.1491	0.1185	0.0373	0.1038	0.0880	0.2261	0.1205
false signs	1	13	5	24	15	62	120

Table 21: RSME and false predicted signs of the derivatives of the recalculated actuator values from the test data set using the direct approach

The advantage of the direct approach is certainly the avoidance of matrix inversions that were already presented in the previous chapters. Hence, the inversions always lead to numerical problems resulting in inaccurately calculated actuator values, a direct calculation of the actuator changes from the monitor changes allows a more accurate prediction of the necessary actuator changes. Nonetheless, there is also a disadvantage of this approach: The direct dependencies between actuators and monitors cannot be shown, because the already inverted nonlinear and with coupled terms filled response matrix is calculated directly.

#### 6.4.3. Optimization of the modified SINDy algorithm

Because the values for  $\lambda$  and for the order of the polynomials were chosen by experience for the first iteration of the modified SINDy algorithm, further investigations are needed to optimize the performance of the system identification. This can be achieved with a brute force approach by scanning with polynomials from order one up to the highest possible order with  $\lambda$ -values in the intervall [0,1] with 100 steps in between.

Especially for the higher order polynomials, one has to consider that the maximum amount of degrees of freedom (=coefficients) is given by the sample size. For this reason, the highest possible polynomial order p is chosen by calculating the amount of coefficients  $c_{needed}$  using the binomial coefficients and comparing them to the sample size (eq. 6.20, table 22). The amount of actuators  $n_{actuators} = 11$  was raised by one to implement the constants of the polynomials.

$$c_{needed} = \begin{pmatrix} n_{actuators} + p - 1 \\ p \end{pmatrix} = \begin{pmatrix} n_{actuators} \\ p \end{pmatrix}$$
 (6.20)

polynomial order $p$	coefficients $c_{needed}$	ok with data set length?
1	11	$\checkmark$
2	66	$\checkmark$
3	286	×
4	1001	×
5	3003	×

Table 22: Possible polynomial orders referring to the given training data set with 233 setpoints

With the given table 22, it is now possible to set up an optimization for the polynomial orders  $p = \{1,2\}$  with the goal to find the combination with the lowest RMSE errors averaged over all actuators. As fig. 66-67 shows, with a polynomial order of two, the best results can be achieved. The optimal value for the spasification hyper-parameter  $\lambda$  is 0.794795. RSME and misinterpreted signs are presented in table 23. It has to be mentioned that this value fits this specific data set best and can vary for other data sets. In addition to this, the optimum found is located next to a large decrease of accuracy by only margins in the value of  $\lambda$ . A lower value in the region  $\lambda \approx 0.1$  would lead to a slightly worse control system accuracy but increases the safety margin towards the big

increase significantly.

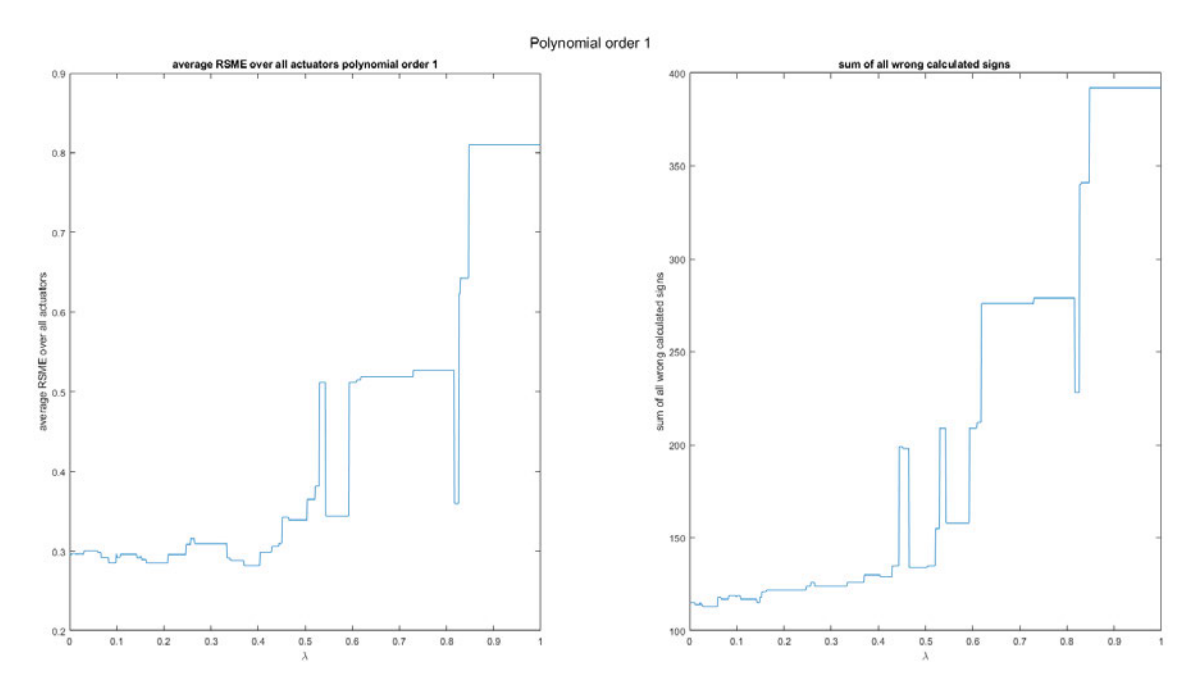


Figure 52: Optimization of the modified SINDy approach: scan  $\lambda$  in the range of [0, 1] using sequential least squares and polynomial order 1 to find lowest RSME

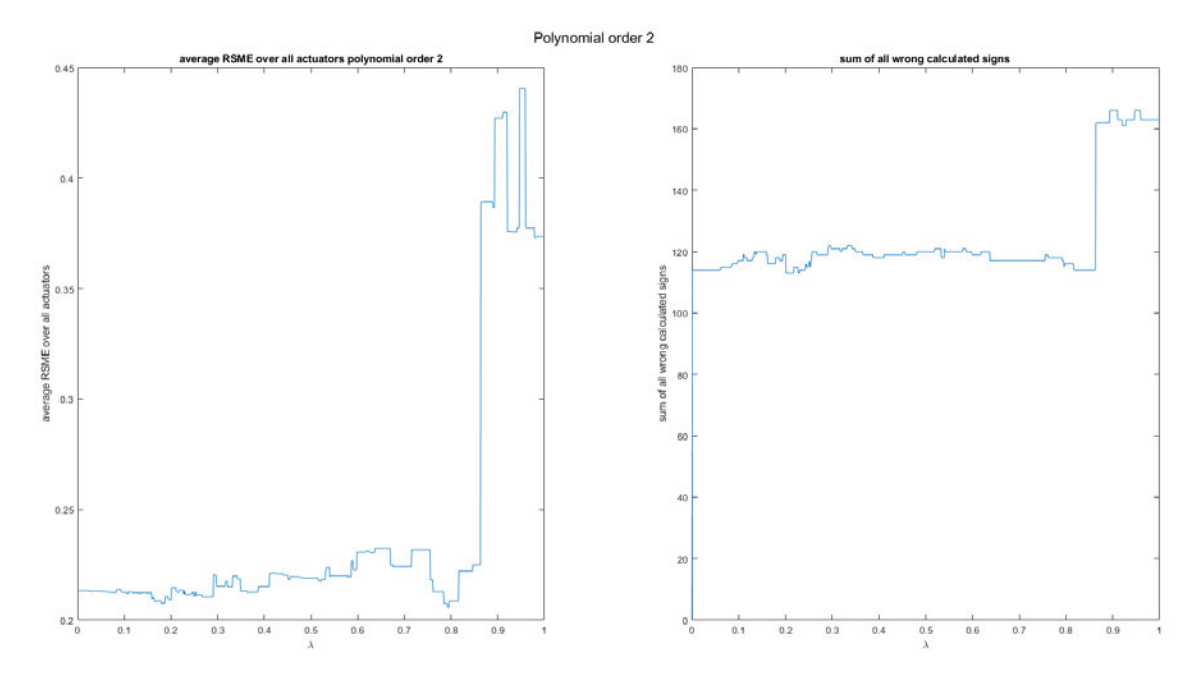


Figure 53: Optimization of the modified SINDy approach: scan  $\lambda$  in the range of [0, 1] using sequential least squares and polynomial order 2 to find lowest RSME

	Gun Ph	ACC139 SV	ACC139 C	ACC23 SV	ACC23 C	ACC45 SV	avg./total
RMSE	0.1290	0.1315	0.0293	0.0924	0.0709	0.2261	0.1132
false signs	4	12	6	21	12	62	117
improvement RMSE $\%$	13.47	-10.95	21.42	11.02	19.44	0.00	6.04
improvement signs $\%$	-300.00	7.69	-20.00	12.50	20.00	0.00	2.50

Table 23: RSME and false predicted signs of the derivatives of the recalculated actuator values from the test data set using the optimized direct approach compared to the not optimized, direct SINDy approach

Furthermore, the method to sparsify the  $\Xi$  was chosen to be a sequential least squares algorithm. As presented in chapter 4.2, a convex optimization is also possible but takes more computational time and will be investigated in this chapter, too. For this reason, the same optimization is performed again, only the sequential least squares approach was exchanged with a convex optimization without additional restrictions.

The optimized sparsity matrices are presented in figure 54 and show that the convex optimization has lead to a less sparse solution than the sequential least squares approach. The results (RMSE, wrong calculated signs of the derivatives and comparison to the not optimized model) can be found in table 24. They show an improvement in the RSME-values as well as in the false predicted signs of the derivatives. Graphs of both criteria over  $\lambda$  are attached in appendix D.

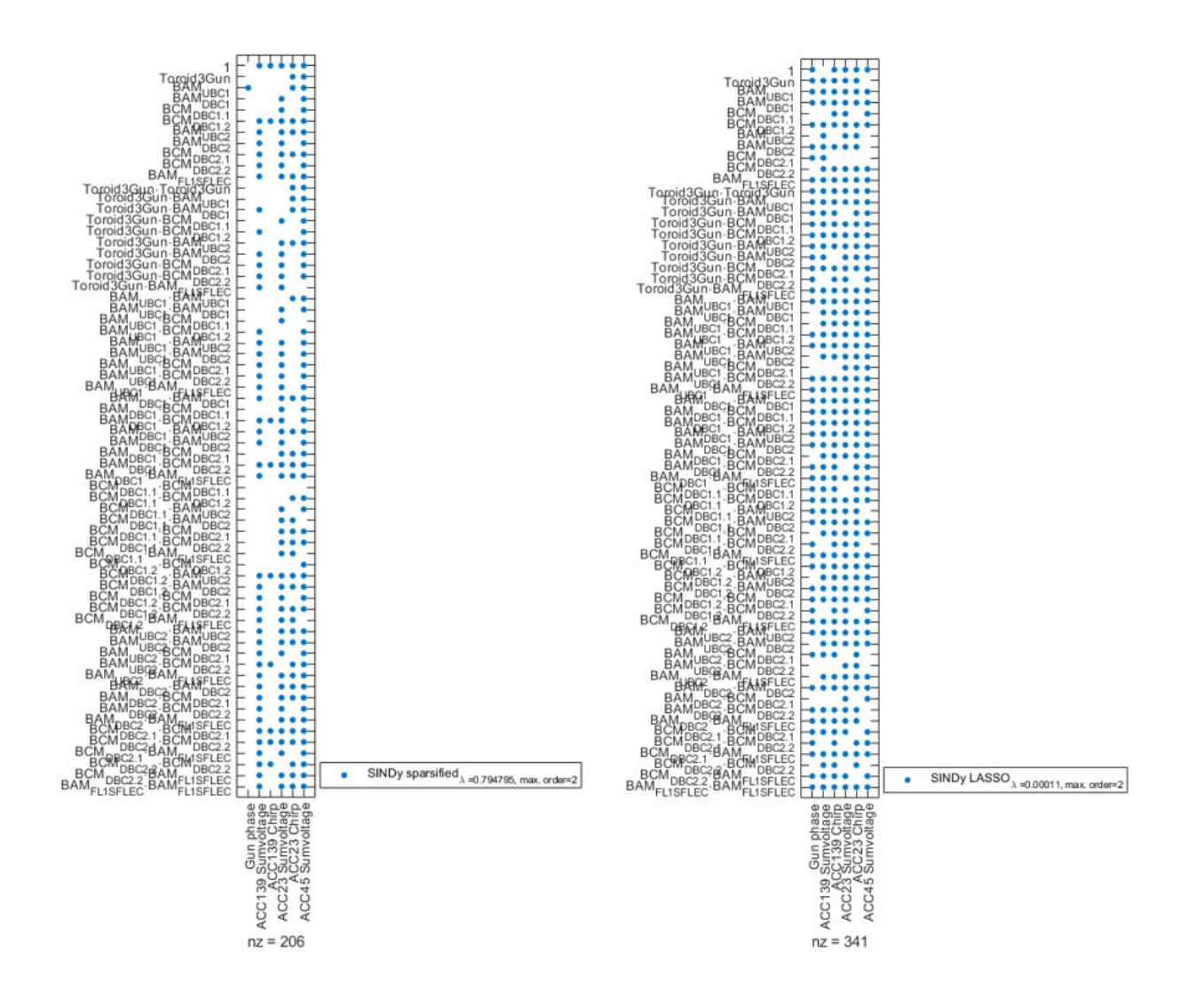


Figure 54: Sparsity matrices from the optimized approaches

	Gun Ph	ACC139 SV	ACC139 C	ACC23 SV	ACC23 C	ACC45 SV	avg./total
RMSE	0.1514	0.1194	0.0300	0.1036	0.0678	0.2052	0.1129
false signs	5	13	4	21	14	57	114
improvement RMSE $\%$	-1.53	-0.69	19.54	0.21	22.99	9.23	6.30
improvement signs $\%$	-400.00	0.00	20.00	12.50	6.67	8.06	5.00

Table 24: RSME and sign evaluation of the direct SINDy approach using LASSO-regression compared to the non-optimized, direct SINDy approach

The results show that the convex optimization leads to better results, hence, this approach will be followed.

#### 6.5. Adding further base functions to SINDy modified

Furthermore, other base functions aside the polynomials like  $e^x$ ,  $\frac{1}{x}$  and  $\sqrt{x}$  can be added to perform a system identification. By adding these terms to the algorithm, the library matrix  $\Theta$  and the sparsified matrix  $\Xi$  increase in size. So, checking whether the amount of coefficients needed exceeds the length of the training data set is necessary and provided in eq. 6.21.

$$c_{needed,extended} = \left( \binom{n_{actuators}}{p} \right) + c_{e^x} + c_{\frac{1}{x}} + c_{\sqrt{x}}$$
 (6.21)

With a maximum polynomial order of p = 2 and the number of actuators  $n_{actuators} = 10$ , the coefficients of the added base functions refer to ten, too, because they do not have any combinations of monitors themselves but only the single values (eq. 6.22).

$$c_i = n_{actuators} (6.22)$$

As result of eq. 6.22 96 coefficients face a data set of 233 setpoints so that all three functions can be implemented at once. Again, the results are evaluated using the RSME and the false calculated derivative signs (table 25).

	Gun Ph	ACC139 SV	ACC139 C	ACC23 SV	ACC23 C	ACC45 SV	avg./total
RMSE	0.1023	0.0405	0.0234	0.1887	0.0742	0.1680	0.0995
false signs	3	6	3	20	10	58	100
improvement RMSE $\%$	31.36	65.79	37.15	-81.81	15.70	25.69	17.37
improvement signs $\%$	-200.00	53.85	40.00	16.67	33.33	6.45	16.67

Table 25: RSME and false predicted signs of the derivatives of the recalculated actuator values from the test data set compared to the not optimized, direct SINDy approach

A visualization of the matrix  $\Xi$  can be found in fig. 55. There are improvents in both criteria, so the additional terms will stay for the subsequent investigations.

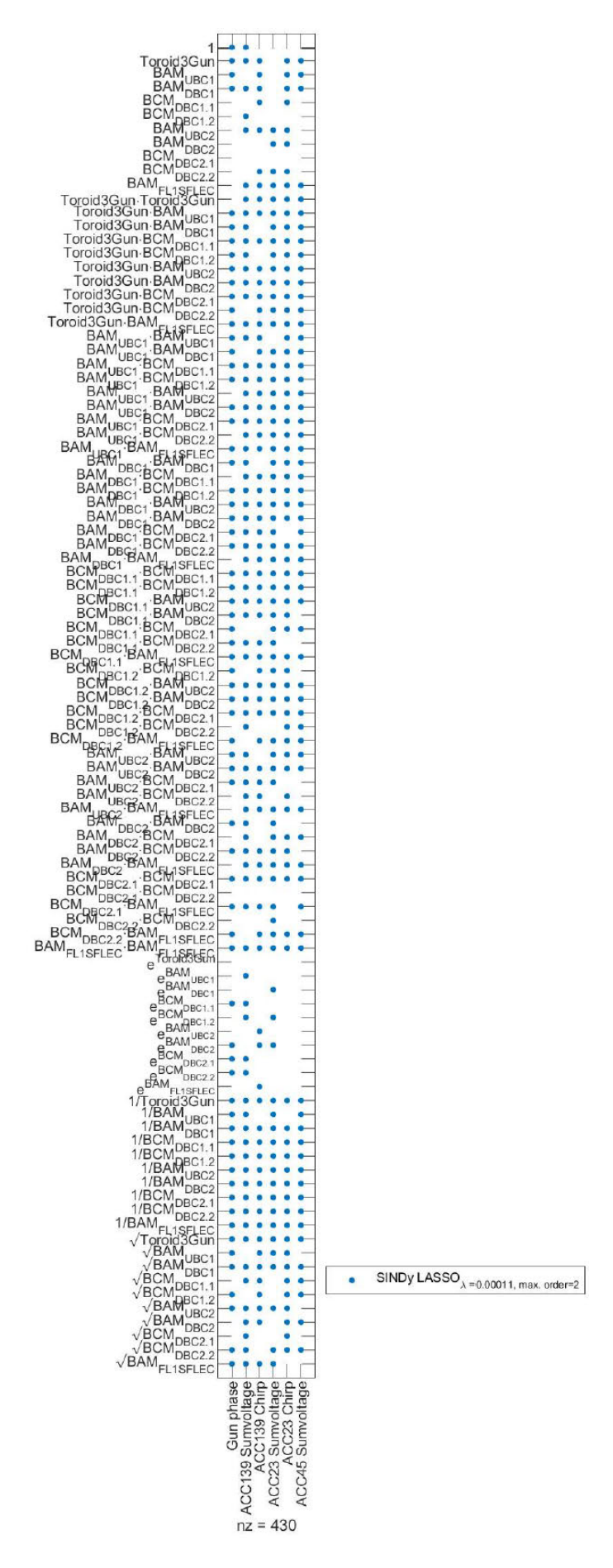


Figure 55: Visualization of the sparsity matrix using convex optimization and additional terms 83

#### 6.6. Influence of the bunch number for control

As described in chapter 2, only the first entry of each macrobunch is currently used for the control system. Since the spectra for the data set analyzed in this chapter have ten entries for beam region 1, this subsection deals with the influence of the bunch number on the control system. For this reason, the following variations will be performed for the entries of the macrobunches of beam region 1 and compared:

- averaged value
- median value

The general setup for the comparison is again the modified SINDy algorithm with additional terms using a convex optimization. The value for  $\lambda$  was not changed after the previous optimization.

For comparison RSME and falsely calculated signs of the derivatives are taken again and shown in table 26 and table 27. Both, averaged value and median value result in similar predictions of the actuator values which just vary slightly from the approach using the first entries of the macrobunch. Therefore, the influence of the bunch number is low and almost negligible.

	Gun Ph	ACC139 SV	ACC139 C	ACC23 SV	ACC23 C	ACC45 SV	avg./total
RMSE	0.1020	0.0092	0.0351	0.1889	0.0823	0.1987	0.1027
false signs	3	6	2	21	10	59	101
improvement RMSE $\%$	31.57	92.21	5.94	-81.92	6.56	12.10	14.76
improvement signs $\%$	-200.00	53.85	60.00	12.50	33.33	4.84	15.83

Table 26: RSME and falsely predicted derivatives signs of the recalculated actuator values from the test data set compared to the not optimized, direct SINDy approach using the mean value of the macrobunch

	Gun Ph	ACC139 SV	ACC139 C	ACC23 SV	ACC23 C	ACC45 SV	avg./total
RMSE	0.0940	0.0142	0.0342	0.1973	0.0874	0.2148	0.1070
false signs	3	5	2	20	10	59	99
improvement RMSE $\%$	36.94	87.99	8.29	-90.09	0.72	5.02	11.19
improvement signs $\%$	-200.00	61.54	60.00	16.67	33.33	4.84	17.50

Table 27: RSME and falsely predicted derivatives signs of the recalculated actuator values from the test data set compared to the non-optimized, direct SINDy approach using the median value of the macrobunch

#### 7. Conclusion and Outlook

It has been shown that the current control system has room for improvement by building a mathematical model based on the information given by the control system and by examining data from the DAQ during user runs. Firstly, several matrix approaches were tested using response matrices. The results of these approaches show a better prediction with the nonlinear matrices than with the linear ones. All these approaches were followed by the same problem: the inversion of the response matrices, which lead to inaccurate predictions of the actuator changes due to high condition numbers of the response matrices even after normalization. Furthermore, it has been shown that dynamics do not take a measurable share in the control system by applying the SINDy algorithm. Nevertheless, a modification of this algorithm by excluding dynamics and using the coupled terms of various order to fit the system firstly indirectly and later on directly, allowed to identify the system with high precision.

Although, the first calculations with the modified SINDy algorithm already lead to good results for an update of the current control system, the algorithm was improved constantly. A deeper look into other parameters like additional equations for the fit, the influence bunch train number, the value of the sparsification parameter  $\lambda$  as well as the implementation of a convex optimization to replace the initial sequential least squares method improved the system identification step by step.

A comparison of all approaches for test data used within this work is provided in table 28 (RSME) and in table 29 (sign of the derivatives). The modified SINDy algorithm delivers the best solution in combination with additional terms in both criteria. With the current control system, an average RSME of 6.8334 was calculated for the test data set. In contrast to this, the best SINDy approach reaches a value of 0.0995. Further, the total amount of misinterpreted signs of the derivatives could be reduced from 336 to 100. Further investigations on the bunch number did not lead to better results although they achieved the same level.

			ACC139		ACC23			
Approach	Description	Gun phase	sumvoltage	ACC139 Chirp	sumvoltage	ACC23 Chirp	sumvoltage	average
	current matrix from							
FLASH 2024	control system; single loop	1.243	1.4290	1.3057	1.4631	25.1265	10.4330	6.8334
FLASH 2024	normalized	2,453						
convex	full matrix	0.281						
convex	reduced matrix	0.245		0.6534				
convex	single loop matrix	0.162	0.9432	0.7480	0.2153	0.9867	0.2397	7 0.5493
convex	full matrix, normalized	0.218	0.4198	0.0597	0.8892	0.2838	1.5284	0.5665
convex	reduced matrix, normalized	0.191	0.3474	0.1333	0.0923	0.4168	0.1143	3 0.2159
convex	single loop matrix, normalized	0.127	0.3474	0.1428	0.1223	0.4124	0.1165	0.2115
nonlinear	full matrix	0.537	7 0.2602	0.2055	0.4868	0.0706	20.9878	3.7581
nonlinear	reduced matrix	0.157	1.5353	0.8725	2.0607	1.3683	4.1859	1.6967
nonlinear	single loop matrix	0.153	0.0801	0.0568	0.3793	0.2256	0.2815	0.1960
	modified for each	0.145	0.0790	0.0467	0.3987	0.2324	0.1238	0.4744
nonlinear	actuator best MSE	0.145	0.0790	0.0467	0.3987	0.2324	0.1238	3 0.1711
nonlinear	(combination)	0.145	0.0790	0.0467	0.3793	0.0706	0.1238	0.1409
SINDy	monitors + inversion	0.148	7 0.3018	0.0937	2.4615	1.4530	4.2352	1.4490
CIMP	actuators order 2,	0.140	0.4405	0.0070	0.4000	0.000	0.005	0.4305
SINDy	lambda=0.5	0.149	0.1185	0.0373	0.1038	0.0880	0.2261	0.1205
SINDy	actuators + convex	0.151	0.1194	0.0300	0.1036	0.0678	0.2052	0.1129
	actuators + convex +							
SINDy	base functions	0.102	0.0405	0.0234	0.1887	0.0742	0.1680	0.0995
	actuators, order2,							
SINDy	lambda=0.794795	0.129	0.1315	0.0293	0.0924	0.0709	0.2261	0.1132
	actuators + convex +	+						
SINDy	base functions +median	0.094	0.0142	0.0342	0.1973	0.0874	0.2148	3 0.1070
J., 10 y	actuators + cconvex		0.0142	0.0342	0.1373	0.0074	0.2140	0.1070
CIMDo	+ base functions	0.103	0.000	0.0354	0.1000	0.0000	0.100	7 0.4037
SINDy	+mean	0.102	0.0092	0.0351	0.1889	0.0823	0.1987	0.1027

Table 28: Comparison of all approaches applied to the test data set (RSME)

Approach	Description	Gun phase	ACC139 sumvoltage	ACC139 Ch	ACC23 irp sumvoltage	ACC23 Chirp	ACC45 sumvoltage	sum	
	current matrix from control								
FLASH 2024	system		52	43	65	64	57	55	336
FLASH 2024	normalized		52	43	65	64	57	55	336
convex	full matrix		4	47	17	51	50	45	214
convex	reduced matrix		4	69	106	68	61	66	374
convex	single loop matrix		4	69	97	65	59	65	359
convex	full matrix, normalized		4	47	17	51	50	45	214
convex	reduced matrix, normalized		4	69	106	68	61	66	374
COTIVEX			-	03	100	00	01	00	0/4
convex	single loop matrix, normalized		4	69	97	65	59	65	359
nonlinear	full matrix		43	50	41	42	66	50	292
nonlinear	reduced matrix		4	66	102	61	75	61	369
nonlinear	single loop matrix		4	10	16	27	20	32	109
nonlinear	modified for each actuator		4	10	8	32	19	29	102
nonlinear	best MSE (combination)		4	10	8	27	66	29	144
SINDy	monitors + inversion order 2, lambda=0.5		3	22	6	67	99	86	283
SINDy	actuators order 2, lambda=0.5		1	13	5	24	15	62	120
SINDy	actuators + conve	(	5	13	4	21	14	57	114
SINDy	actuators + conve + base functions	(	3	6	3	20	10	58	100
	actuators, order2,								
SINDy	lambda=0.794795	<u> </u>	4	12	6	21	12	62	117
SINDy	actuators + conve + base functions +median	(	3	5	2	20	10	59	99
SINDy	actuators + conve + base functions +mean	(	3	6	2	21	10	59	101
Sintely	· Allouii		-	0		-1	10	55	101

Table 29: Comparison of all approaches applied to the test data set (derivative sign)

For further improvement of the control system, taking new data with all accelerating modules in operation would be beneficial and could lead to an even better understanding of the system.

Shortly after taking the data of the parameter scans, the FLASH accelerator has gone into a long shutdown during which all accelerating modules got warmed up and the whole beamline of FLASH 1 gets renewed. For this reason, further testing of the dependencies found or even an update of the control system is impossible until summer of 2025 when operation starts again.

In the meantime, data sets are taken at the EuXFEL that should be used to prove the modified SINDy algorithm on another (fairly similar) machine. If the test is successful, the test-wise implementation into the control system would be the next step before a permanent solution will be implemented.

For the first implementation, it is necessary to run parameter scans for every set point of the machine, this takes about half an hour for roughly 350 setpoints, which was the amount of setpoints used in this thesis.

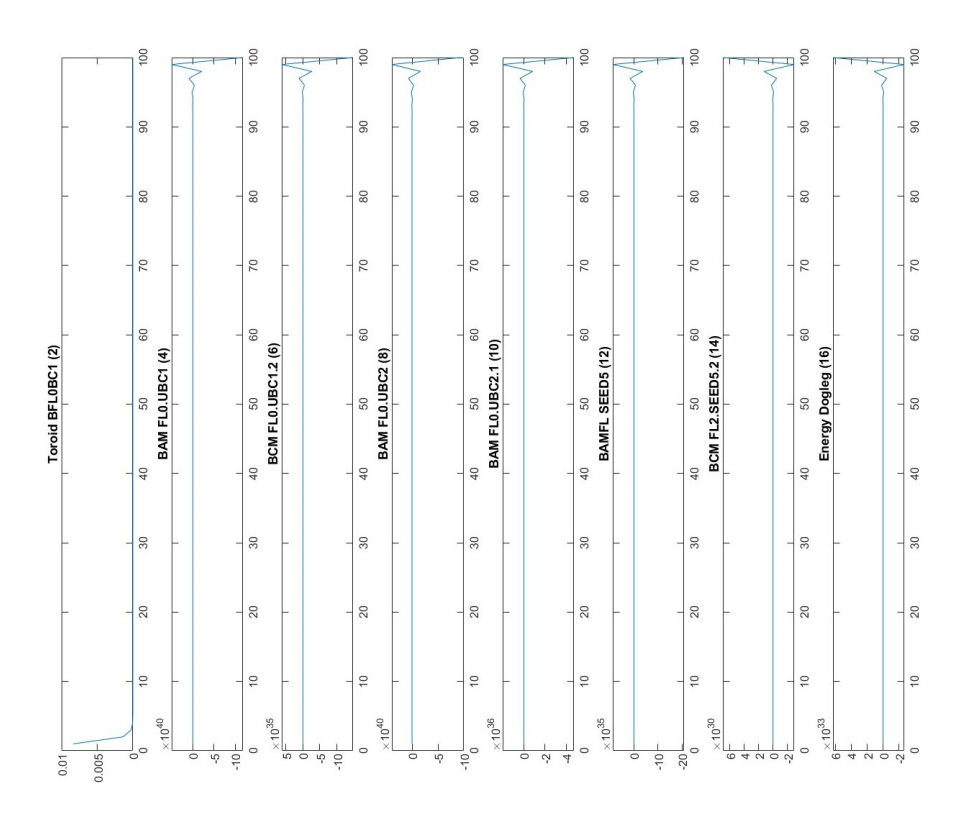
#### References

- [1] NDR. Forschungszentrum DESY und seine Beschleuniger. [online] https://www.ndr.de/geschichte/schauplaetze/DESY-Forschungszentrum-und-seine-Beschleuniger,desy167.html, date: 03.06.2024.
- [2] David Carroll. Overview of High Energy Lasers: Past, Present, and Future? In 42nd AIAA Plasmadynamics and Lasers Conference, Honolulu, Hawaii, June 2011. American Institute of Aeronautics and Astronautics.
- [3] Bart Faatz, Markus Braune, Olaf Hensler, Katja Honkavaara, Raimund Kammering, Marion Kuhlmann, Elke Ploenjes, Juliane Roensch-Schulenburg, Evgeny Schneidmiller, Siegfried Schreiber, Kai Tiedtke, Markus Tischer, Rolf Treusch, Mathias Vogt, Wilfried Wurth, Mikhail Yurkov, and Johann Zemella. The FLASH Facility: Advanced Options for FLASH2 and Future Perspectives. Applied Sciences, 7(11):1114, October 2017.
- [4] Ye Chen, Frank Brinker, Winfried Decking, Matthias Scholz, and Lutz Winkelmann. Perspectives towards Sub-Ångström Working Regime of the European X-ray Free-Electron Laser with Low-Emittance Electron Beams. Applied Sciences, 11(22):10768, November 2021.
- [5] R Kammering and Ch Schmidt. Feedbacks and Automation at the Free Electron Laser in Hamburg (FLASH). Feedback Systems, 2014.
- [6] Hannes Dinter. Longitudinal Diagnostics for Beam-Based Intra Bunch-Train Feedback at FLASH and the European XFEL. 2018.
- [7] M Werner, T Lensch, J Lund-Nielsen, Re Neumann, D Noelle, D Nölle, and N Wentowski. A Toroid Based Bunch Charge Monitor System with Machine Protection Features for FLASH and XFEL. 2014.
- [8] Christopher Gerth and Nils Lockmann. Bunch Compression Monitor Based on Coherent Diffraction Radiation at European XFEL and FLASH. *Proceedings of the 10th International Beam Instrumentation Conference*, 2021.
- [9] DESY. Free-Electron Laser FLASH. [online] https://flash.desy.de/, date: 07.07.2024.
- [10] J. Zhu, N. M. Lockmann, M. K. Czwalinna, and H. Schlarb. Mixed Diagnostics for Longitudinal Properties of Electron Bunches in a Free-Electron Laser. Frontiers in Physics, 10:903559, July 2022.
- [11] Mathias Vogt. FLASH OP-Lecture. June 2017.

- [12] Steven L. Brunton, Joshua L. Proctor, and J. Nathan Kutz. Discovering governing equations from data: Sparse identification of nonlinear dynamical systems. *Proceedings of the National Academy of Sciences*, 113(15):3932–3937, April 2016. arXiv:1509.03580 [math].
- [13] Claudio Pellegrini and Joachim Stöhr. X-ray free-electron lasers—principles, properties and applications. Nuclear Instruments and Methods in Physics Research Section A: Accelerators, Spectrometers, Detectors and Associated Equipment, 500(1-3):33–40, March 2003.
- [14] FLASH. [online] https://www.desy.de/forschung/anlagen\_projekte/flash/index\_ger.html, date: 18.07.2024.
- [15] European XFEL. European XFEL in international comparison. [online] https://www.xfel.eu/facility/comparison/index\_eng.html, date: 14.09.2024.
- [16] H Dewa, H Fujita, M Ikegami, M Inoue, Y Iwashita, S Kakigi, M Kando, A Noda, H Okamoto, T Shirai, and Kyoto University. Pulsed Beam Current Monitor with a Toroidal Coil. 1994.
- [17] Sami Tibshirani, Harry Friedman, and Trevor Hastie. The Elements of Statistical Learning. 2008.
- [18] Zheqiao Geng and Stefan Simrock. *Intelligent Beam Control in Accelerators*. Particle Acceleration and Detection. Springer International Publishing, Cham, 2023.
- [19] Wen-Xu Wang, Rui Yang, Ying-Cheng Lai, Vassilios Kovanis, and Celso Grebogi. Predicting Catastrophes in Nonlinear Dynamical Systems by Compressive Sensing. Physical Review Letters, 106(15):154101, April 2011.
- [20] Sébastien Bubeck. Convex Optimization: Algorithms and Complexity, November 2015. arXiv:1405.4980 [cs, math, stat].
- [21] Stephen P. Boyd and Lieven Vandenberghe. *Convex optimization*. Cambridge University Press, Cambridge, UK; New York, 2004.
- [22] Urban Fasel, Eurika Kaiser, J. Nathan Kutz, Bingni W. Brunton, and Steven L. Brunton. SINDy with Control: A Tutorial, August 2021. arXiv:2108.13404 [math].

## **Appendix**

# Appendix A Additional figures for the analysis of the existing system



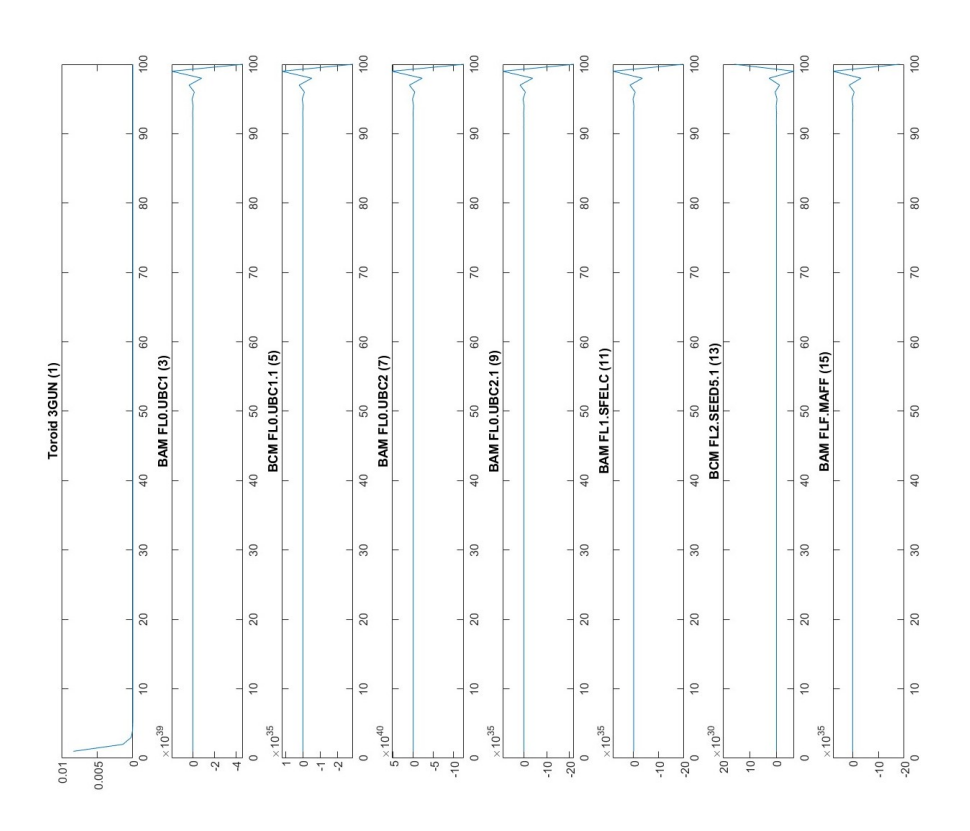
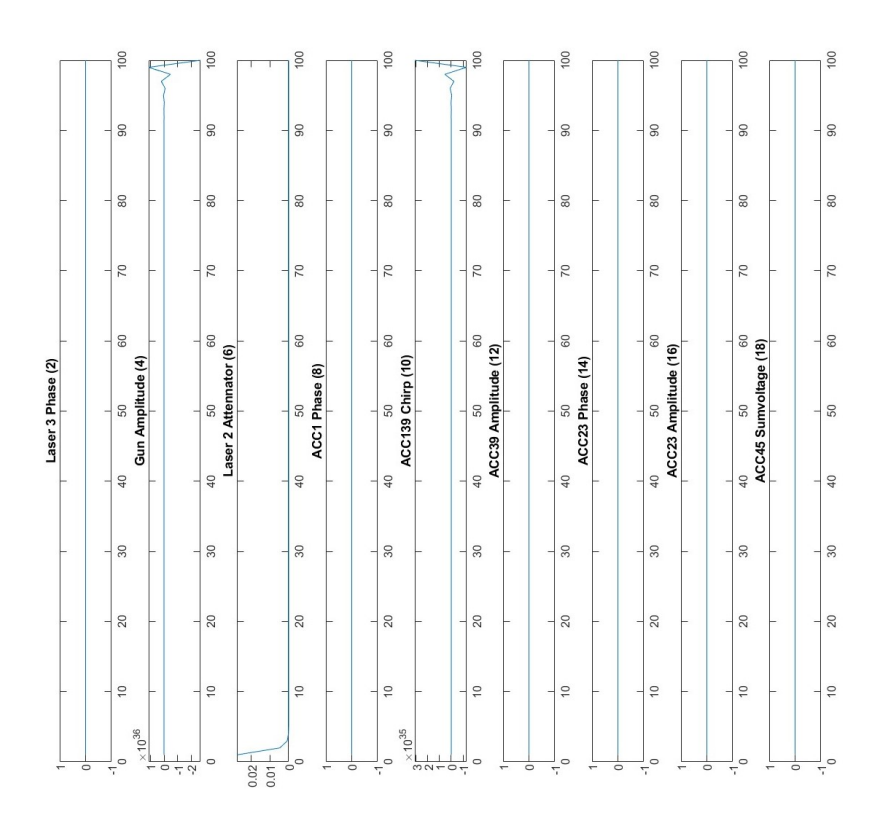


Figure 56: results for all monitors using the simplified response matrix C



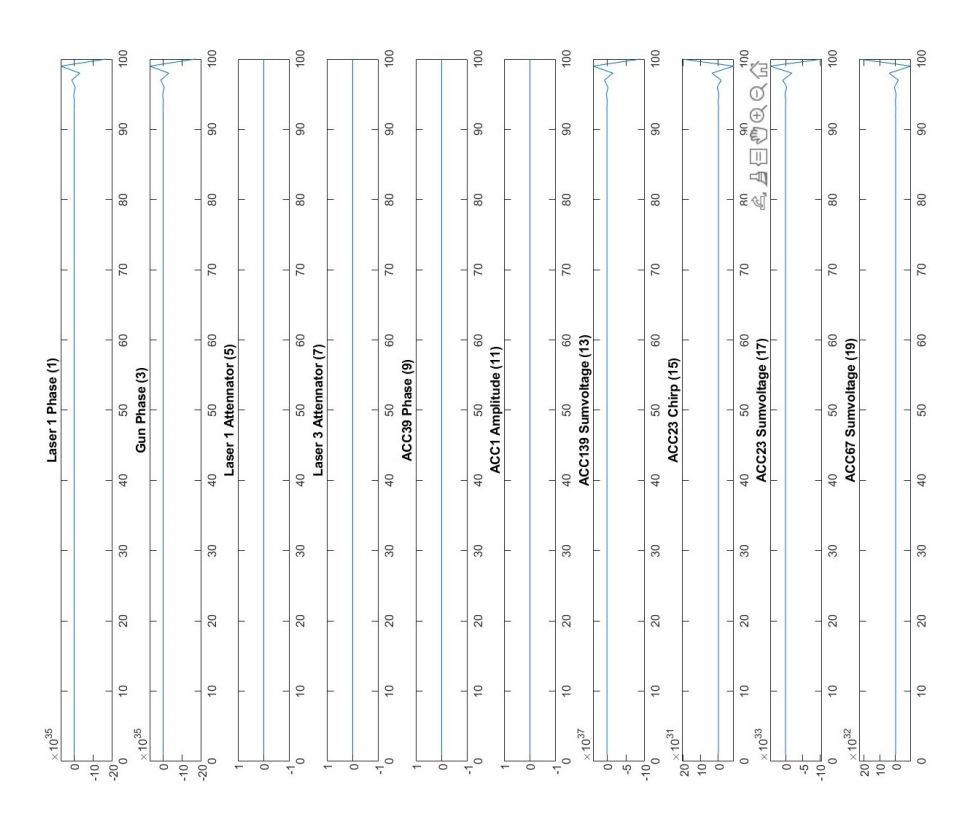
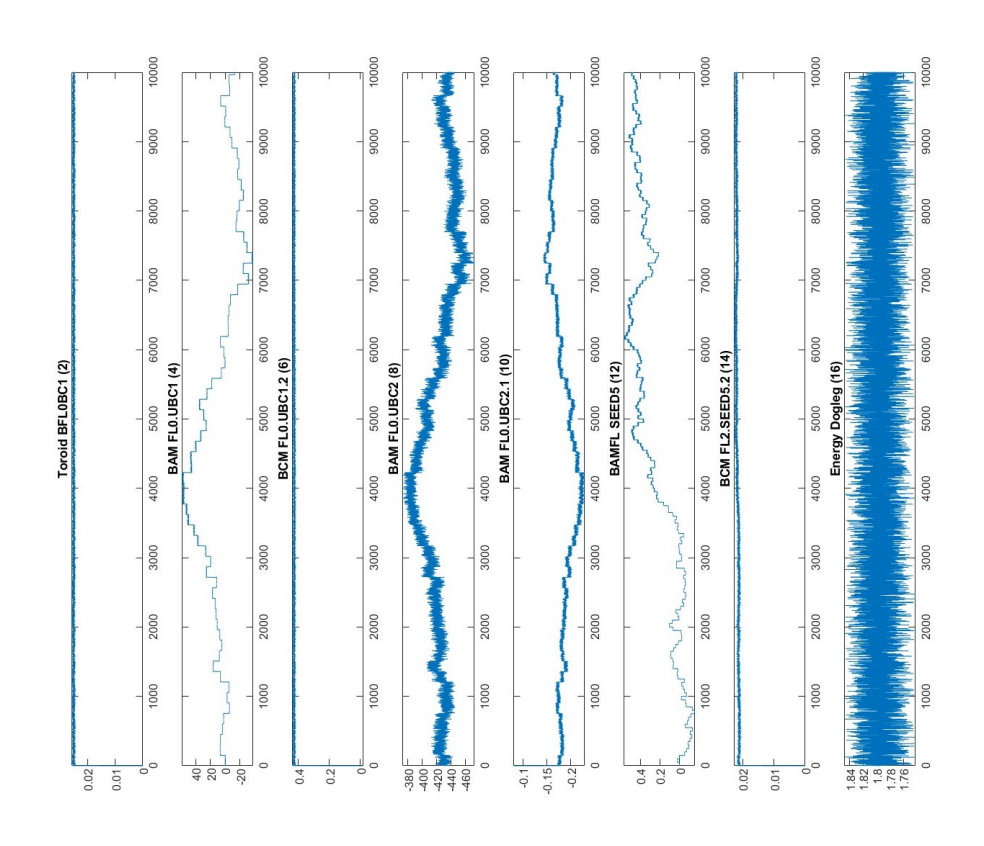


Figure 57: results for all actuators using the simplified response matrix  ${\cal C}$ 



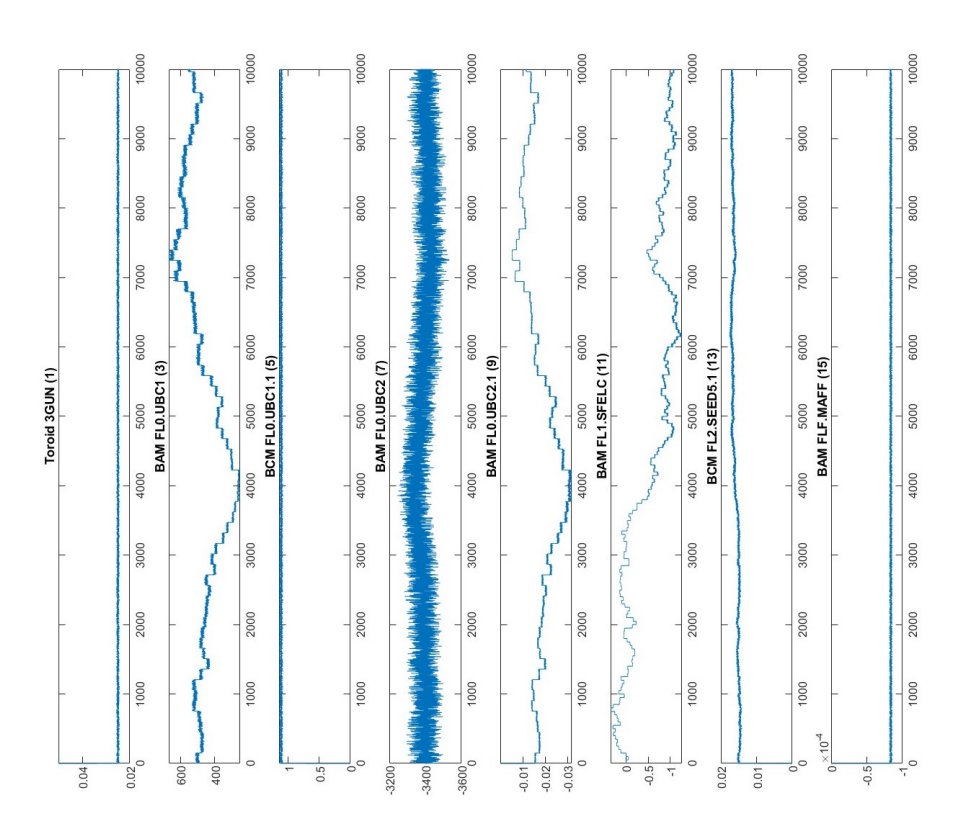
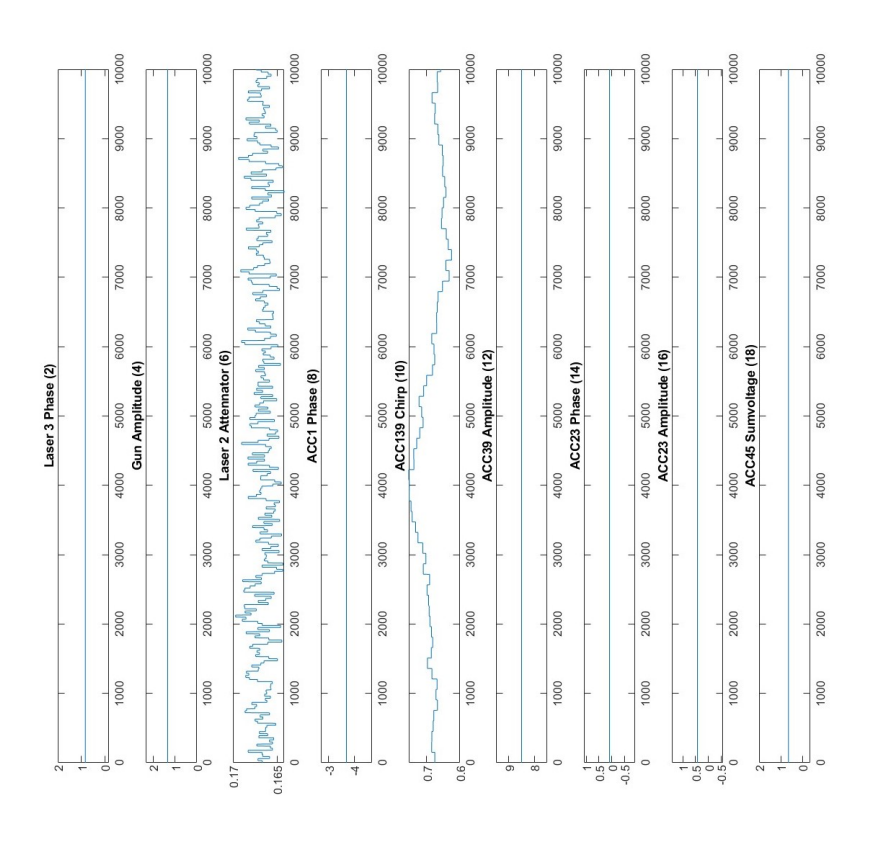


Figure 58: results for all monitors using the response matrix R with the extended model



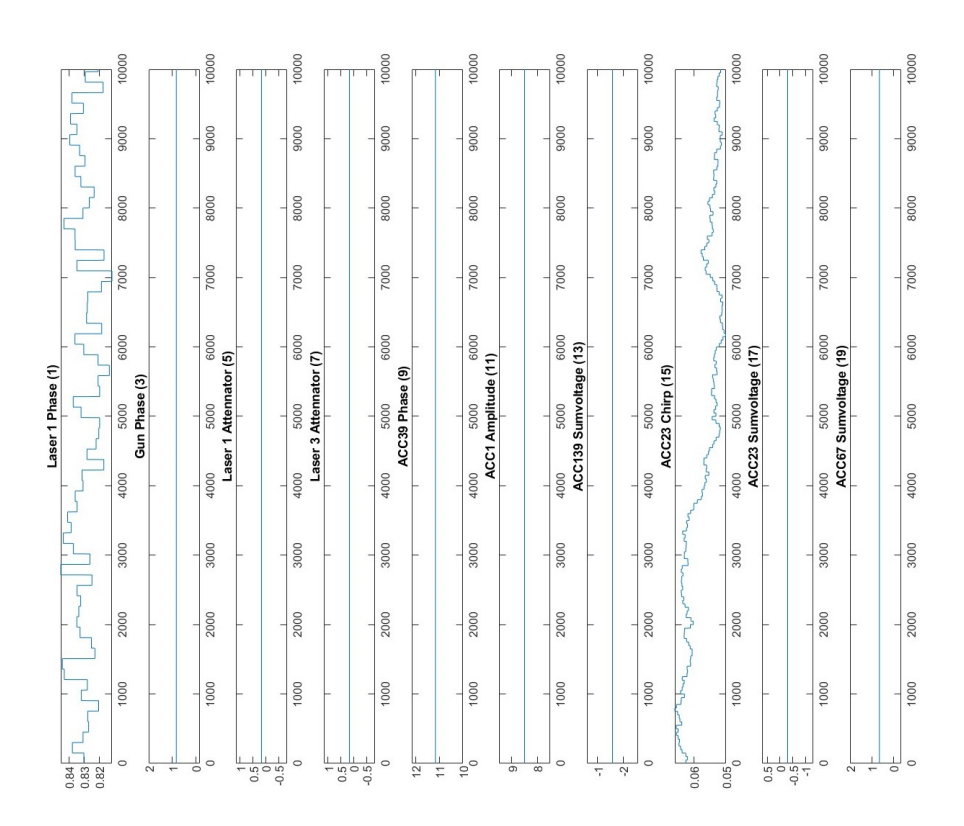


Figure 59: results for all actuators using the response matrix R with the extended model

### Appendix B $\frac{\delta m}{\delta a}$ -plot with raw data

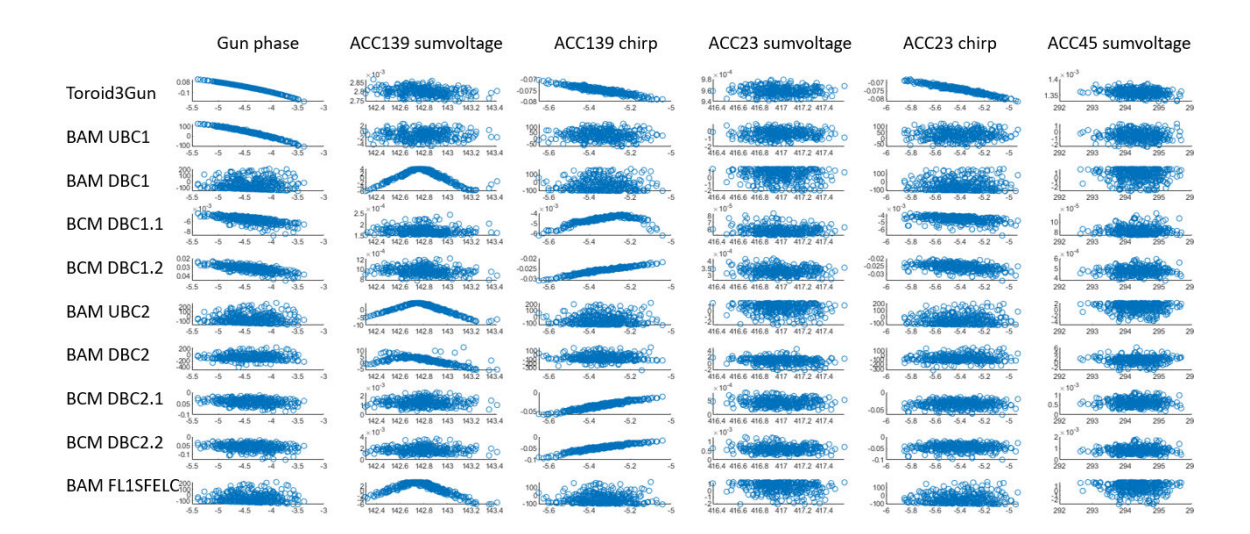


Figure 60: nonlinear dependencies between changes of actuators and monitors

### Appendix C Nonlinear fit for all actuators

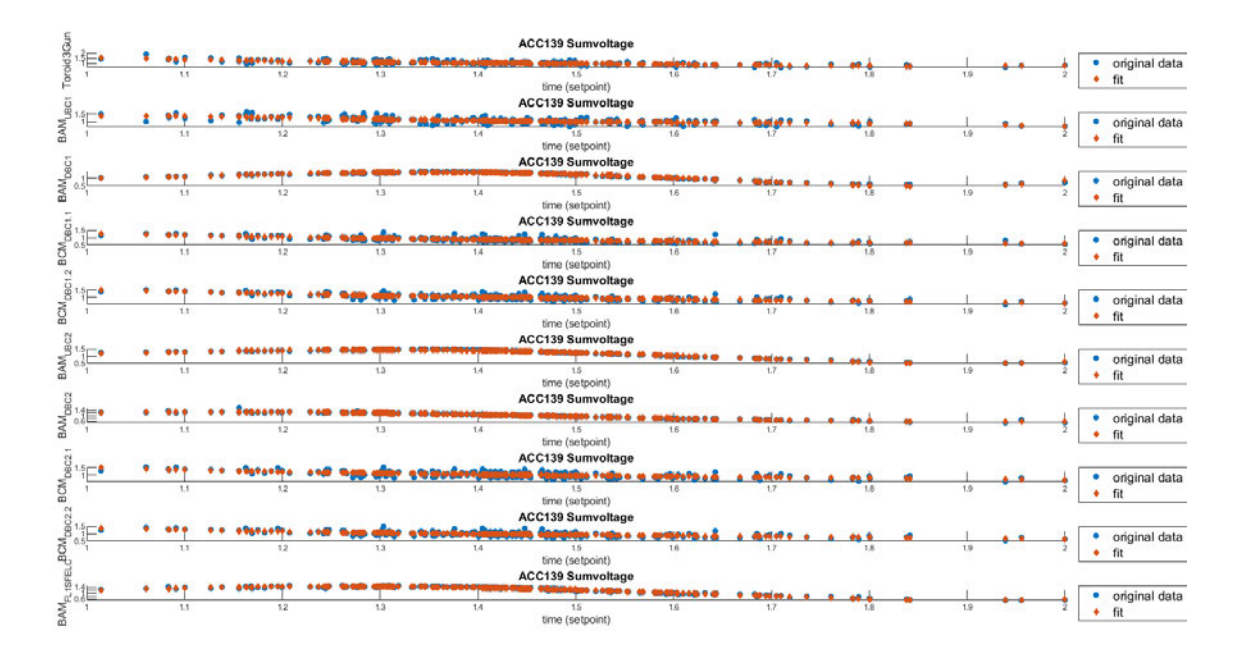


Figure 61: Fitted data for ACC139 sumvoltage with polynomials of order 4



Figure 62: Fitted data for ACC139 chirp with polynomials of order 2



Figure 63: Fitted data for ACC23 sumvoltage with polynomials of order 2



Figure 64: Fitted data for ACC23 chirp with polynomials of order 2



Figure 65: Fitted data for ACC45 sumvoltage with polynomials of order 2

## Appendix D Optimization of the LASSO regressed model

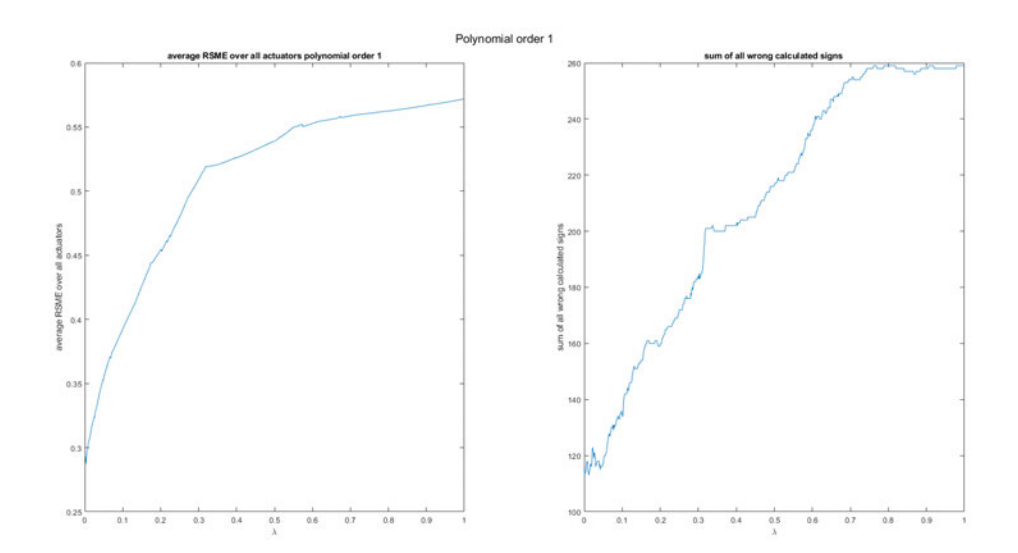


Figure 66: Optimization of the modified SINDy approach: scan  $\lambda$  in the range of [0, 1] using convex optimization and polynomial order 1 to find lowest RSME

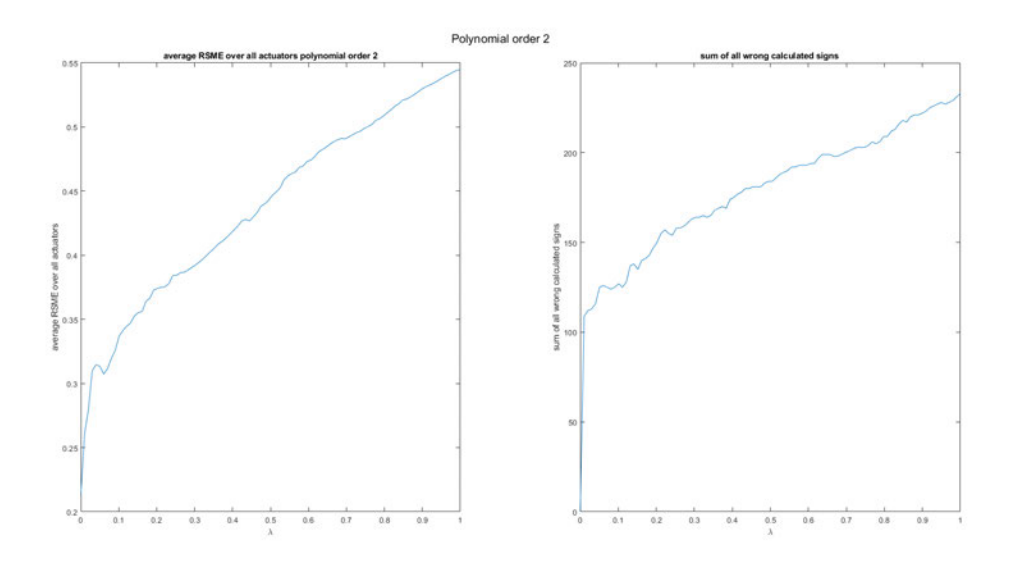


Figure 67: Optimization of the modified SINDy approach: scan  $\lambda$  in the range of [0,1] using convex optimization and polynomial order 2 to find lowest RSME



Hochschule für Angewandte Wissenschaften Hamburg

Hamburg University of Applied Sciences

#### Erklärung zur selbstständigen Bearbeitung einer Abschlussarbeit

Gemäß der Allgemeinen Prüfungs- und Studienordnung ist zusammen mit der Abschlussarbeit eine schriftliche Erklärung abzugeben, in der der Studierende bestätigt, dass die Abschlussarbeit "– bei einer Gruppenarbeit die entsprechend gekennzeichneten Teile der Arbeit [(§ 18 Abs. 1 APSO-TI-BM bzw. § 21 Abs. 1 APSO-INGI)] – ohne fremde Hilfe selbständig verfasst und nur die angegebenen Quellen und Hilfsmittel benutzt wurden. Wörtlich oder dem Sinn nach aus anderen Werken entnommene Stellen sind unter Angabe der Quellen kenntlich zu machen."

Quelle: § 16 Abs. 5 APSO-TI-BM bzw. § 15 Abs. 6 APSO-INGI

Dieses Blatt, mit der folgenden Erklärung, ist nach Fertigstellung der Abschlussarbeit durch den Studierenden auszufüllen und jeweils mit Originalunterschrift als <u>letztes Blatt</u> in das Prüfungsexemplar der Abschlussarbeit einzubinden.

Eine unrichtig abgegebene Erklärung kann -auch nachträglich- zur Ungültigkeit des Studienabschlusses führen.

	Erklärung zur selbstständigen Bearbeitung der Arbeit
Hiermit ver	rsichere ich,
Name:	Müller
/orname:	Lukas
gekennzei	ie vorliegende Masterarbeit bzw. bei einer Gruppenarbeit die entsprechend chneten Teile der Arbeit – mit dem Thema: n optimization of slow longitudinal feedback systems for free electron lasers
enutzt ha	de Hilfe selbständig verfasst und nur die angegebenen Quellen und Hilfsmittel be. Wörtlich oder dem Sinn nach aus anderen Werken entnommene Stellen sind unter er Quellen kenntlich gemacht.
,	- die folgende Aussage ist bei Gruppenarbeiten auszufüllen und entfällt bei Einzelarbeiten -
Die Kennzerfolgt dure	eichnung der von mir erstellten und verantworteten Teile der -bitte auswählen- ist ch:
	Hamburg 23.09.2024
	Ort Datum Unterschrift im Original